# BIOMEDICAL APPLICATIONS OF COBALT-SPINEL FERRITE NANOPARTICLES

# FOR CANCER CELL EXTRACTION AND DRUG DELIVERY

A Thesis
Presented to
The Academic Faculty

by

Kenneth Edward Scarberry

In Partial Fulfillment
of the Requirements for the Degree
Ph.D. in the
School of Chemistry and Biochemistry

Georgia Institute of Technology
May 2009

**BIOMEDICAL APPLICATIONS OF COBALT-SPINEL FERRITE NANOPARTICLES**

**FOR CANCER CELL EXTRACTION AND DRUG DELIVERY**

Approved by:

Dr. John Zhang, Advisor
School of Chemistry and Biochemistry
*Georgia Institute of Technology*

Dr. Donald Doyle
School of Chemistry and Biochemistry
*Georgia Institute of Technology*

Dr. Adegboyega Oyelere
School of Chemistry and Biochemistry
*Georgia Institute of Technology*

Dr. Nael McCarty
Division of Pulmonology, Allergy/Immunology, Cystic Fibrosis, and Sleep
*Emory University School of Medicine*

Dr. John McDonald
School of Biology
*Georgia Institute of Technology*

Date Approved: April 3, 2009

[I dedicate this work to my family.  Their love and support are what kept me going.]

## ACKNOWLEDGEMENTS

I would like to extend my deepest appreciation to Dr. Donald Doyle, Dr. Nael McCarty, Dr. Adegboyega Oyelere, and Dr. John McDonald for the time they have committed to serving on my thesis committee.

I would like to express my sincere gratitude for the opportunities provided to me through the collaborations established with the laboratories of Dr. John McDonald and the CCID Department managed by Dr. Sherry Owen at the Center for Disease Control.

I am very grateful for all the help and support given to me by Dr. Erin Dickerson, Laura Kappa, and Donna Rudolph.

I would also like to express my great appreciation to Dr. John Zhang and Dr. John McDonald for serving as my advisors.

# TABLE OF CONTENTS

# LIST OF TABLES

# LIST OF FIGURES

# LIST OF SYMBOLS AND ABBREVIATIONS

| | |
|---|---|
| MNP | magnetic nanoparticle |
| IP | intraperitoneal |
| GFP | green fluorescent protein |
| VEGF | vascular endothelial growth factor |
| VP | viral particles |
| YSA peptide | GGGGYSAYPDSVPMMSK |

## SUMMARY

In this presentation it is demonstrated that the unique magnetic properties of superparamagnetic cobalt-spinel ferrite nanoparticles can be employed in several novel applications. A method to selectively capture and remove pathogens from infected organisms to improve longevity is presented. Evidence is provided to show that automated methods using modified forms of hemofiltration or peritoneal dialysis could be used to eliminate the particle/pathogen or particle/infected cell conjugates from the organism postoperatively. It is shown that disparately functionalized nanoparticles can be used in concert as drug carrier and release mechanisms. Lastly, we provide preliminary evidence to support the use of magnetic nanoparticles for controlling reaction kinetics.

# CHAPTER 1

# INTRODUCTION

The patent intent of my body of research was to uniquely conceive and analytically substantiate a variety of applications for nanoscale materials having special magnetic properties, henceforth referred to as magnetic nanoparticles (MNPs). Magnetic nanoparticles are an attractive therapeutic tool for a number of reasons. Their size (i.e. measured in nanometers) gives them the ability to distribute ubiquitously throughout an infected organism and seek out pathogens wherever they reside. They have unique magnetic properties[1, 2] that provide a targeting mechanism and a means by which to eliminate them postoperatively. They can be easily coated with biocompatible substances to increase their biopersistence.[3, 4] Their surfaces can be functionalized, and the polymers can be selected based on their ability to improve particle solubility in a particular fluid or to regulate its biodistribution. Many biological applications have been proposed for magnetic nanoparticles over the last few decades and some continue to be active topics of research.[5]

Two of the more common applications being researched for magnetic nanoparticles are diagnostics and drug delivery. Several studies have shown that functionalized nanoparticles are capable of targeting pathogens and binding those pathogens to enhance their detection.[6-9] The magnetic properties of these particles also facilitate their localization to tumor sites or other areas within the body in need of therapy making them attractive drug transports. Novel conjugation strategies have been designed to tether the therapeutic package to the particle using bioconjugation chemistry.[1] After being carried to the target site the therapeutic payload must be

released. Some release strategies rely on the disparate physiological conditions in the intracellular and extracellular spaces. Using pH labile bonds means that the payload can be released when the particle moves between pH conditions.[10] Disulfide bonds have been used because they are readily cleaved by the highly reductive intracellular environment.[11]

Although some groups are finding that the in vivo deployment of magnetic nanoparticles has no toxicological effects[12], this area has not been heavily researched and is much in need of further attention. Various surface coatings have been applied to the particles to enhance their biocompatibility.[4] Coatings like Dextran, and PEG have dramatically increased the particle's half-life in vivo. However, the bondings between the coating and particle surface may rely on non-covalent interactions that lead to shorter shelf lives. In addition, adding functionalities to polysaccharides like Dextran can involve the use of highly toxic reagents like epichlorohydrin. It may be possible to identify similar polymers that do not require the use of toxic reagents during functionalization and that bind to the nanoparticle surface more securely.

Another area that has not received much consideration is the elimination of the nanoparticles from the body after their therapeutic tour is complete. Currently, most of the suggested procedures are surgical in nature and highly invasive. Minimally invasive techniques could increase social acceptance of using nanoparticles in biomedical procedures.

## Fundamentals

In order that the reader may more clearly comprehend the direction of my research I have included several brief topic reviews. These topics include a description of the crystal structure of the nanoparticles that I work with, the magnetic properties of these nanoparticles and how they are measured, the rationale and approach behind

making them biocompatible, and the strategies used to add functionalities to them. In addition this chapter contains reviews on metastatic cancer and the characteristics of the HIV-1 virus and its lifecycle so the reader may understand the applicability of the research. Lastly, there is a section that describes chalcogenides, which is a family of elements used in my research for their exquisite chemical bonding properties and a section on the chemiluminescent properties of Luminol. The chemiluminescent section is being provided to clarify a proof of concept that I designed to show that magnetic nanoparticles could be used to control reaction kinetics ad libitum.

**Spinel Ferrites**

The magnetic nanoparticles we developed are known as spinel ferrites with a general composition formula of $MFe_2O_4$ (M = Mn, Mg, Zn, Co, Fe and other divalent cations or a mixture of these cations).[13] Due to the high compositional flexibility, spinel ferrites offer great opportunities for designing and fine-tuning the magnetic properties of nanoparticles based upon the magnetic interactions at the atomic level and the crystal chemistry. Russell-Saunders couplings between the cations on the lattice sites of the metals making up the spinel structure dictate its magnetic properties. Magnetic coupling is affected by the distance between lattice sites, the magnetic moments, and the symmetry of those moments. The nanoparticles used throughout my studies were cobalt ferrites. They were synthesized using a microemulsion technique that will be explained below and their spinel structures were verified using x-ray diffraction.[14] The purity of the sample and size determinations can be made using this technique. Particle size estimates can be made based on peak broadening and calculating the area under

the curve. Transmission electron microscopy was also used to make size determinations.

**Reverse Micelle Synthesis**

In the microemulsion technique, the spinel ferrite particle precipitates from an organic-based salt solution. The solution contains amphiphilic organic compounds called surfactants that aggregate to form a micellar structure that acts as an incubation chamber for the burgeoning particle.[15]

**Superparamagnetism**

The important point to remember about superparamagnetic behavior is that particles that express it become magnetized in the presence of a magnetic field and remain demagnetized when it is withdrawn. This characteristic is ideal for biomedical applications where the aggregation of particles infused systemically may be undesirable until they are to be eliminated. Magnetism is essentially about magnetic dipoles and how they are arranged in a material. In ferromagnetic materials there is a partial alignment of dipoles in the absence of an external magnetic field. In ferromagnetic materials the dipoles are arranged in two opposite directions but one of these directions has more constituent dipoles than the other giving the material an effective net magnetization when there is no external magnetic field.[16] In antiferromagnetic materials dipoles are all antiparallel to one another making the net magnetization zero. Above a certain temperature, called the Curie temperature, the magnetic properties in ferromagnetic and antiferromagnetic materials change because the force from thermal oscillations is greater than force between the aligned dipoles. The alignment of the dipoles is lost as the thermal oscillations cause them to rotate in different directions. A material having fewer dipole moments has less dipole interaction energy to overcome

and the disruption of the dipole alignments can occur at lower temperatures. This disruption leads to randomly oriented dipoles that can align with the magnetic field, which is a property referred to as paramagnetism. When paramagnetism exists below the Curie temperature at ambient temperatures it is called superparamagnetism. Superparamagnetism can be seen at ambient temperatures in nanoparticles with diameters of 10 nm or less.[16] At this size the magnetic materials have been reduced to a single magnetic domain expressing a single magnetic dipole and highly susceptible to agitation by thermal energies.

Superparamagnetism can be verified using a hysteresis loop like the one featured in Figure 1.1. Hysteresis loops typically compare the induced magnetization (M) to the strength of the applied external magnetic field (H). The magnetic field density B: can supplant the induced magnetization value (M) as seen in the figure. Remanence and coercivity can be determined from the hysteresis loop. Remanence is the magnetization that remains in the material once the magnetic field is removed and coercivity is the magnetic field strength needed to be applied in the opposite direction to return the material's magnetization to zero. Hysteresis is the work done on a magnet and is defined as the width of the hysteresis loop. The hysteresis measurements taken by our group to determine the magnetic properties of our synthesized magnetic materials were taken using a superconducting quantum interference device (SQUID) which is able to detect changes in magnetic field.[17]

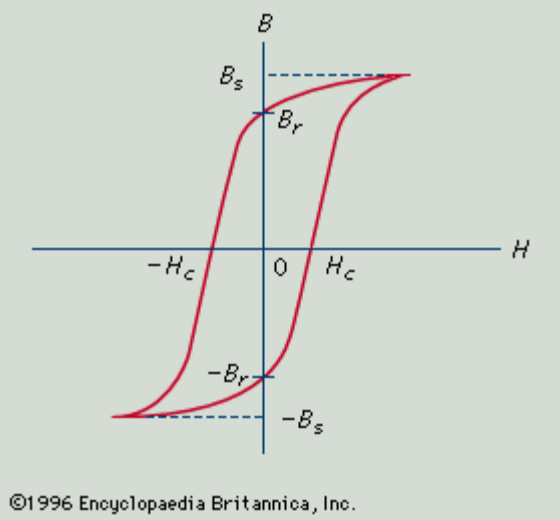


Figure 1.1: Hysteresis loop.

**Biocompatible Coatings**

The nanoparticles are coated with a polysaccharide polymer to increase their biocompatibility. This technique provides the advantage of diminishing an immune response to the particles since glycans do not typically illicit such a response.[18] The polymer coating used also contained numerous free hydroxyls that willingly form hydrogen bonds in aqueous solution. In concert, the many surface hydroxyls hold the particle and surface coat in suspension for an indefinite period of time. This ability is important if the goal is to inject the particles into the general circulation or the ascities fluid of the peritoneal cavity. The surfaces of the polymer can be functionalized with molecules (e.g. antibodies, peptides, or aptamers)[4] that can direct them to specific sites in vivo, and can influence their distribution, reactivity, and retention at the target site[19, 20].

**Nanoparticle Functionalization and Bioconjugate Techniques**

Fundamentally, nanoparticle functionalization entailed understanding the surface chemistry of the MNP and finding practical conjugation techniques that would allow me to modify it. Many of the applications I was developing for the MNPs required that they be deployed in vivo which required the selection of innocuous coatings or functions. Several of the techniques that were adopted and found well suited to my needs were techniques that had been employed in protein chemistry and pharmacology. The chemical procedures are explained in detail in Chapter 2. In theory, anything can be considered toxic in sufficient dosages. Toxicity studies endeavor to discover the acceptable level of tolerance for a specific compound. With regard to our nanomaterials, we wanted to provide functionality while abrogating any adversarial interactions to avoid crossing the toxic threshold. Using coatings previously determined as harmless by the pharmaceutical industry to cover the indiscernibly noxious surface was a good way to head off potential complications until we could test for toxicity. Coating the particle had the added benefit of increasing its solubility and available points of conjugation.

**Metastatic Cancer and the Nature of Ovarian Carcinomas**

In 2005, cancer was responsible for 13% of the deaths worldwide (World Health Organization). The types of cancer contributing the highest mortality rates were lung, stomach, liver, colon, and breast. Often, the lethality of cancers is not due to tumorigenesis at the original locus but to the establishment of distant foci by malignant cells that exfoliate from the primary tumor. This exfoliation and migration is referred to as metastasis and can take place when the tumor is ruptured during surgical intervention or when the malignant cell experiences morphological changes that affect its adherence to other malignant cells at the tumor site. Metastases can lead to a variety of complications. Brain metastases, for instance, usually develop at a late stage

in the progression of certain carcinomas but can have catastrophic effects on cognitive function. Bone metastases typically have a very poor prognosis and are often incurable. Metastases into bone can lead to osteolytic lesions that are typified by nerve-compression syndromes, fractures, severe pain, and terminal hypercalcemia.[21] Lung, breast, kidney, melanoma, and colorectal carcinomas have been shown to metastasize into the central nervous system (CNS) and it is believed that 10-30% of solid tumors follow this same metastatic path.[22] 15-30% of lung, bladder, uteran, rectal, colon, renal, and thyroid cancers metastasize to the bone and the percentage is as high as 70% for breast and prostate cancer.[21] Current modalities for metastatic cancers include surgical excision, and various types of radiation, chemo, and antibody therapies.[23, 24] Radiation therapy can lead to fibrosis.[25] Prophylactic cranial irradiation (PFI), a standard-of-care in CNS metastatic cancer prevention, can lead to adverse neurocognitive disorders.[24] Surgical excisions are often incomplete and leave behind residual cancer mass. Chemo therapies lack efficient targeting strategies and often result in collateral damage to surrounding tissues.

The objective of my research has been to develop a modality aimed at the deterrence of the metastatic development of certain carcinomas. The approach we are using involves functionalizing magnetic nanoparticles with peptides, aptamers, antibodies, or ligands that target receptors that are uniquely expressed by metastasizing cancer cells and extracting those cells magnetically from the organism before they have a chance to establish new foci. Our initial targeting and extraction trials were tested on ovarian cancer cells. Ovarian cancer is one of the most lethal of all gynecological malignancies. While the 5-year survival rate for patients with late stage disease sits around 20%, the survival rate for patients diagnosed with early stage disease climbs

impressively to 94%. Thus, there is an urgent need for improved treatment strategies for late stage disease.

**HIV-1 Life Cycle and Structural Characteristics**

HIV-1 is a member of the Retroviridae family. All retroviruses contain the gag, pol, and env genetic sequences that are necessary for expression of the capsid, accompanying enzymes, and the viral envelope respectively. The HIV-1 genome also contains additional important sequences. The rev sequence produces proteins that trigger the export of unspliced HIV-1 mRNA from the nucleus to be used in viral progeny. The tat sequence codes for a gene specific elongation factor that greatly accelerates the transcription of viral mRNA. The vif sequence is essential for proviral synthesis following viral entry. [26-28] The prerequisites for HIV-1 infection include the uncoating of the virus, reverse transcription of viral RNA, transport of the preintegration complex to the nucleus, and integration of the provirus (viral DNA) into the host genome (Figure 1.2).

The env sequence, responsible for producing the proteins that make up the capsid, expresses the p24 protein. It has been determined that every HIV-1 capsid contains 2000-4000 p24 proteins and this protein is often used to verify HIV-1 infection.[29] This means that once the viral coat and capsid are lysed an immunoassay like an ELISA can be used to detect quantitative levels of p24 protein and these figures can be used to interpolate the number of viral particles.

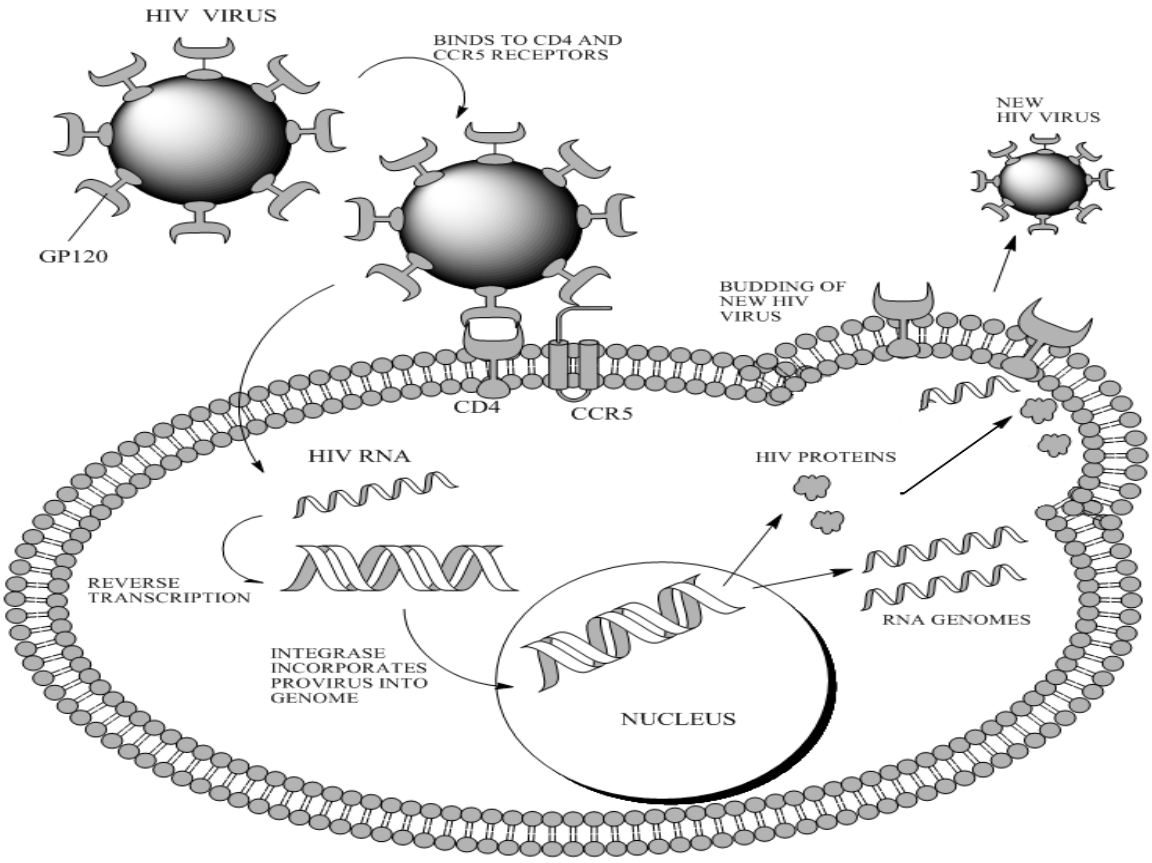


Figure 1.2: Lifecycle of the HIV-1 virus.

**Chalcogenide Bonding**

The chalcogen classification is made up of the Group 16 elements of the periodic table. A subset of this group that is membered by the sulfides, selenides, and tellurides is called the chalcogenides. The valence configuration of these elements ($Xs^2Xp^4$) gives them a high redox potential. Disulfide/thiol redox reactions and the presence of selenides have been found to be essential to many biological processes.[30-32] Dichalcogenide bonds are single covalent bonds that are formed when two of any combination of the protonated chalcogens (thiol (S-H), selenol(Se-H), or tellurol groups (Te-H)) are bound through oxidation. When the electron configuration is such that a shell is more complete it becomes harder for an atom to gain or lose an electron. In the

case of the chalcogens the valence shell for each requires two additional electrons to fill the p orbital. However, it is not the need for additional electrons that is responsible for differences in bonding behavior between the dichalcogens. The atomic size, electronegativity and R groups bound to the chalcogen have a tremendous effect on their bond strengths. Depending on the R group, steric hindrance can lead to rotational barriers that affect the electronic structures of the molecules. Kaur et al. [33] showed that for a dichalcogenide bond X-X and X-R, where X = O, S, Se and R = H, $CH_3$, or $NH_2$, bond lengths were greatest when X = Se and shortest when X = O. However, when X = O and R = $CH_3$ or $NH_2$ the bond lengths almost increased to a non-bonded length. This was not the case when X = S or Se and was explained as being a result of differences in the dihedral angles which were 90 degrees for H-X-X-H when X = S or Se and 120 degress when X = O. When X = O the dihedral angle was larger as a result of hydrogen bonding interactions between the O and H from non-covalently bound O-H groups. When X = S or Se the dihedral angle was determined by lone-pair lone-pair and bond-pair bond-pair repulsions. Kaur et al. [33] also looked at the hemolytic bond dissociation energy (BDE) for the chalcogens mentioned and found that the X-H BDEs were larger than those for H-X-X-H and the values were greatest when X = O and least when X = Se. The BDE levels for H-X-X-H were found to be highest when X=S and lowest when X = O which showed no dependence on the atomic radius of the chalcogen. However, atomic radius was inversely proportional to the BDE values for H-X-$CH_3$. Overall, the data showed that dichalcogen bond strengths were greatest for disulfides and weakest for dioxides. These BDE values explain why the pKa for a selenol is 5.3 and the pKa for a thiol is 8.25. Less energy would be required to deprotonate the hydrogen of a selenol. At a neutral physiological pH a selenol will become a selenate which is the form necessary to reduce a dichalcogenide bond.

**Chemiluminescence and Luminol**

The chemiluminescent reaction featured in Figure 1.3 shows how luminol is able to emit quanta of visible light. In alkaline solution the secondary amine groups are deprotonated by the hydroxides in solution. Electron transfers take place between the dianion that is formed and the carbonyl groups forming an enolate. If oxygen is introduced into the reaction at this point it reacts with the dianion to form an unstable organic peroxide that liberates nitrogen gas. Electron transfer takes place once more and carboxylate anions are formed resulting in 3-aminophthalate. The cleavage of the organic peroxide results in an energy gain and effectively leaves 3-aminophthalate in an excited state which decomposes releasing a quantum of visible light. [34]

It should be noted that throughout the mechanism featured in the diagram the primary amine remains intact. It was for this reason that it was chosen as a conjugation point for the reaction impedance experiment described in the Appendix. The initial supposition was that binding luminol at this point should not adversely affect its capacity to produce light. This was later confirmed to be true.

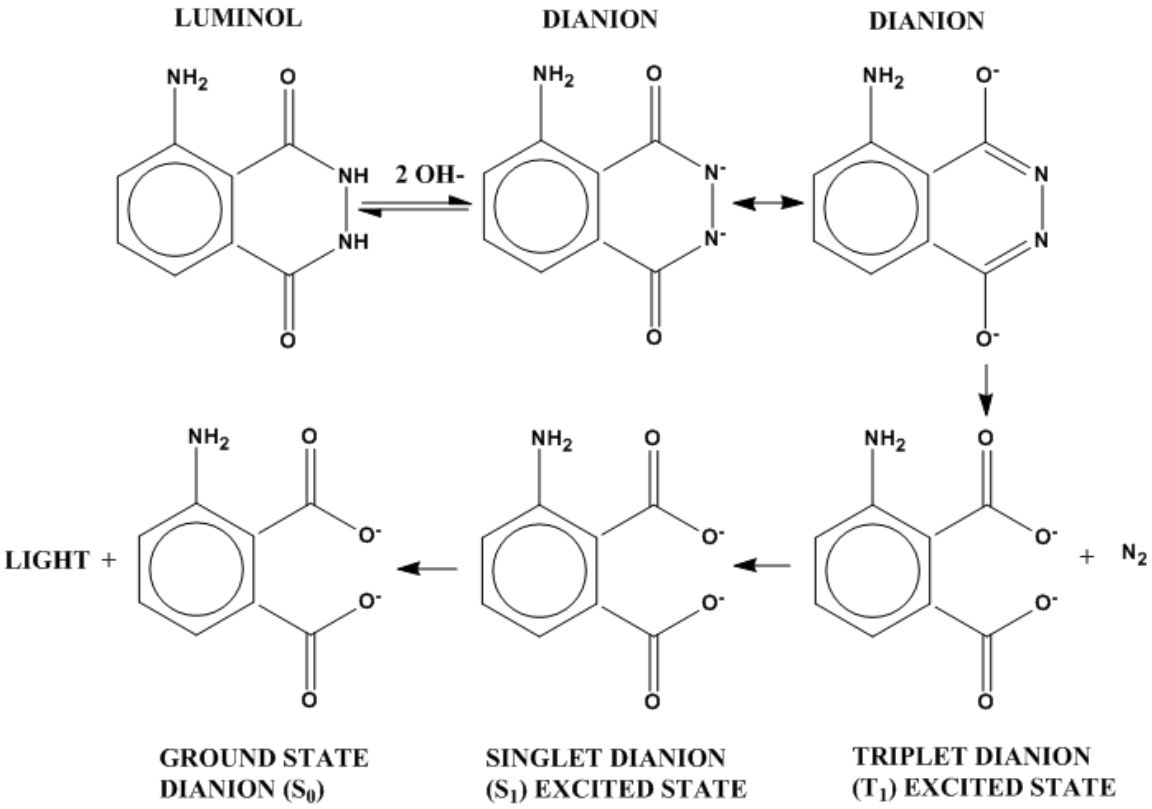


Figure 1.3: Chemiluminescent reaction involving luminol.

# CHAPTER 2

# EXPERIMENTAL APPROACHES AND METHODS

This chapter provides a detailed overview of the experimental designs and methods used throughout the studies described in subsequent chapters. The explanations provided should serve as reference when reading the pertinent study in later chapters.

## Experimental Approaches

### Drug Delivery Application

In vitro experiments were conducted to verify that the particle/package conjugate linked by the dichalcogenide bond could be separated using the described mechanism. In the control group (Figure 2.1) the lability of the dichalcogenide bond was tested using a non-functionalized magnetic nanoparticle. In the experimental group (Figure 2.2), a nanoparticle with a thiol or selenide group was used to cleave a selenyl sulfide or tellurol selenide link respectively. Fluorescein and Luminol were used as packages because their release was visibly detectable using fluorescent microscopy. Acetasalisylic acid was used as a package simply to show that a drug could be conjugated to the particle surface. No studies were conducted to determine whether the conjugation strategy adversely affected the drug's normal function.

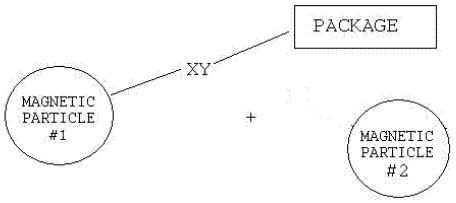


X = S when Y = Se PACKAGE = Fluorescein, Luminol, Acetasalisylic Acid
X = Se when Y = Te

Figure 2.1: Schematic of control group used in drug delivery experiments. The values listed for X and Y illustrate two types of dichalcogenide bonds used to conjugate packages to the nanoparticle surface (#1). The control particles (#2) had no chalcogenide functions.

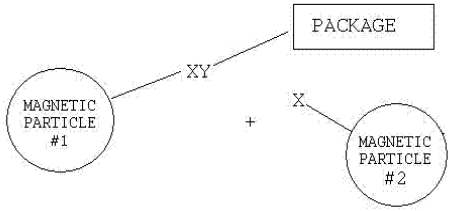


X = S when Y = Se PACKAGE = Fluorescein, Luminol, Acetasalisylic Acid
X = Se when Y = Te

Figure 2.2: Schematic of experimental group used in drug delivery experiments. The values listed for X and Y illustrate two types of dichalcogenide bonds used to conjugate packages to the nanoparticle surface (#1). The control particles (#2) had chalcogenide functions.

The logistics of the experiments were roughly the same for each permutation. A volume of nanoparticles bound to one of the previously mentioned packages was introduced to a reaction vial containing aqueous solution (Figure 2.3.A). Then a second nanoparticle, having or not having been previously conjugated to a chalcogenide function, depending on the group, was also introduced to the reaction vessel (Figure 2.3.A). A magnet was placed beside the vessel to bring the nanoparticle carrier and

nanoparticle release mechanism together (Figure 2.3.B). The magnetic filtrate was examined for traces of the released package (Figure 2.3.C). Three analytical techniques were used to verify the structure of the reaction components and the release mechanism. Fluorescent microscopy was instrumental in visually verifying that fluorophores had been attached to the nanoparticle surfaces and whether or not they were being released. Variations between the UV/Vis spectra obtained from samples at various stages of the conjugation and release process were used to substantiate changes in sample properties. Spectra of the pure compound being conjugated to the nanoparticle, the unconjugated nanoparticle itself, and the conjugated nanoparticle/compound were taken separately and used as baseline comparisons to the magnetic filtrand and filtrate spectra. HPLC/Mass Spectrometry was used to locate the released compound in the magnetic filtrate.

A modification was made to the fluorescent microscopy experiment by incorporating a peristaltic pump driven extracorporeal circuit with an integrated capillary tube that passed over the microscope objective. This design (Figure 2.4) visually illustrated the nanoparticles being captured and the packages being released into the circulating flow. It was also an initial proof of concept showing the plausibility of using the mechanism in systemic circulation in vivo.

The strategy for creating dichalcogenide linkages between the MNP and the packages to be released is thoroughly explained in the next section titled, “Surface Modification Strategies.”

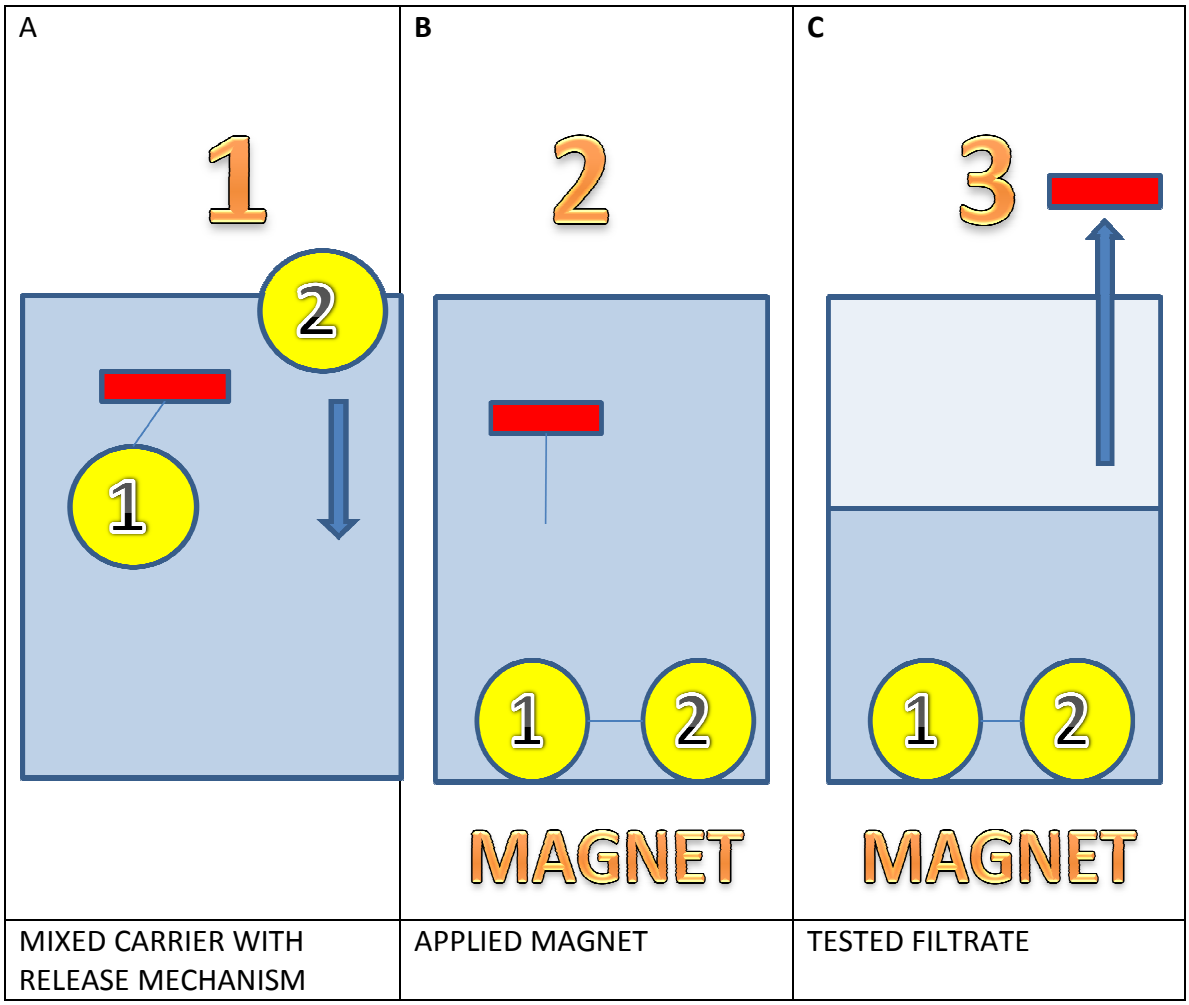


Figure 2.3: A: Nanoparticles (#1) with package conjugates (red box) were added to the reaction vial along with a release mechanism (#2). B: A magnet was placed near the reaction vial to force the nanoparticle/package conjugate to aggregate with the release mechanism. (C) The filtrate was removed from the reaction vial and examined for traces of the released package (red box).

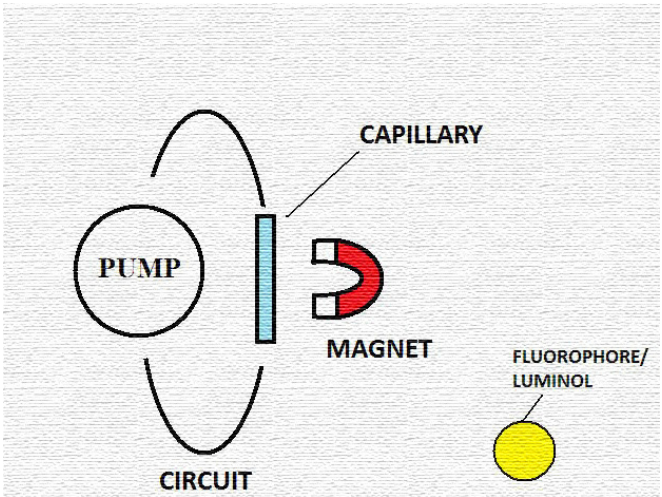


Figure 2.4: Basic schematic diagram showing how the drug release mechanism was tested using a peristaltic pump driven circuit. The capillary was placed over the objective of the microscope and a magnet was placed next to the capillary tube. The nanoparticle (yellow sphere) was pumped through the circuit and could be seen collecting against the side of the capillary tube closest to the magnet.

**Ovarian Cancer Application**

The experimental designs used to show that ovarian cancer cells could be selectively captured using a ligand specific for an ovarian cancer cell membrane receptor are thoroughly explained in Chapter 4 which contains the work as it was published in the Journal of the American Chemical Society.

**Ascites Study**

The ascites study was a natural progression from the ovarian cancer study previously described. Ascites fluid from patients with extraovarian peritoneal serous papillary carcinoma was collected and donated by the Ovarian Cancer Institute in Atlanta, Georgia. The disseminated tumor equivalent for most patients at the time of

sampling corresponded to an ovarian Stage III or IV disease (The International Federation of Gynecology and Obstetrics (FIGO) staging system). An experiment (Figure 2.5) was devised to identify the resident cell populations in the ascites samples and resolve whether the malignant cells could be selectively captured.

A sample of the ascites fluid from a patient was first aliquoted equally into three vials. One vial was left untreated and set aside for analysis. Nanoparticles with peptide conjugates were added to a second vial and nanoparticles with no peptide conjugates were added to a third. The solutions in the two vials containing nanoparticles with and without peptide conjugates were given equal incubation periods and then magnetically separated for equal intervals. The filtrates were drawn from both vials and placed in separate vials for analysis. The filtrand from both vials was washed 3x with PBS and set aside for analysis. All 5 vials were analyzed using a BD LSR flow cytometer (BD Biosciences).

**Ovarian Cancer Survival Study**

The purpose of the ovarian cancer survival study was to discover whether the capture and removal of disseminated tumor cells could be employed as a curative measure to mitigate metastasis and thereby increase longevity.

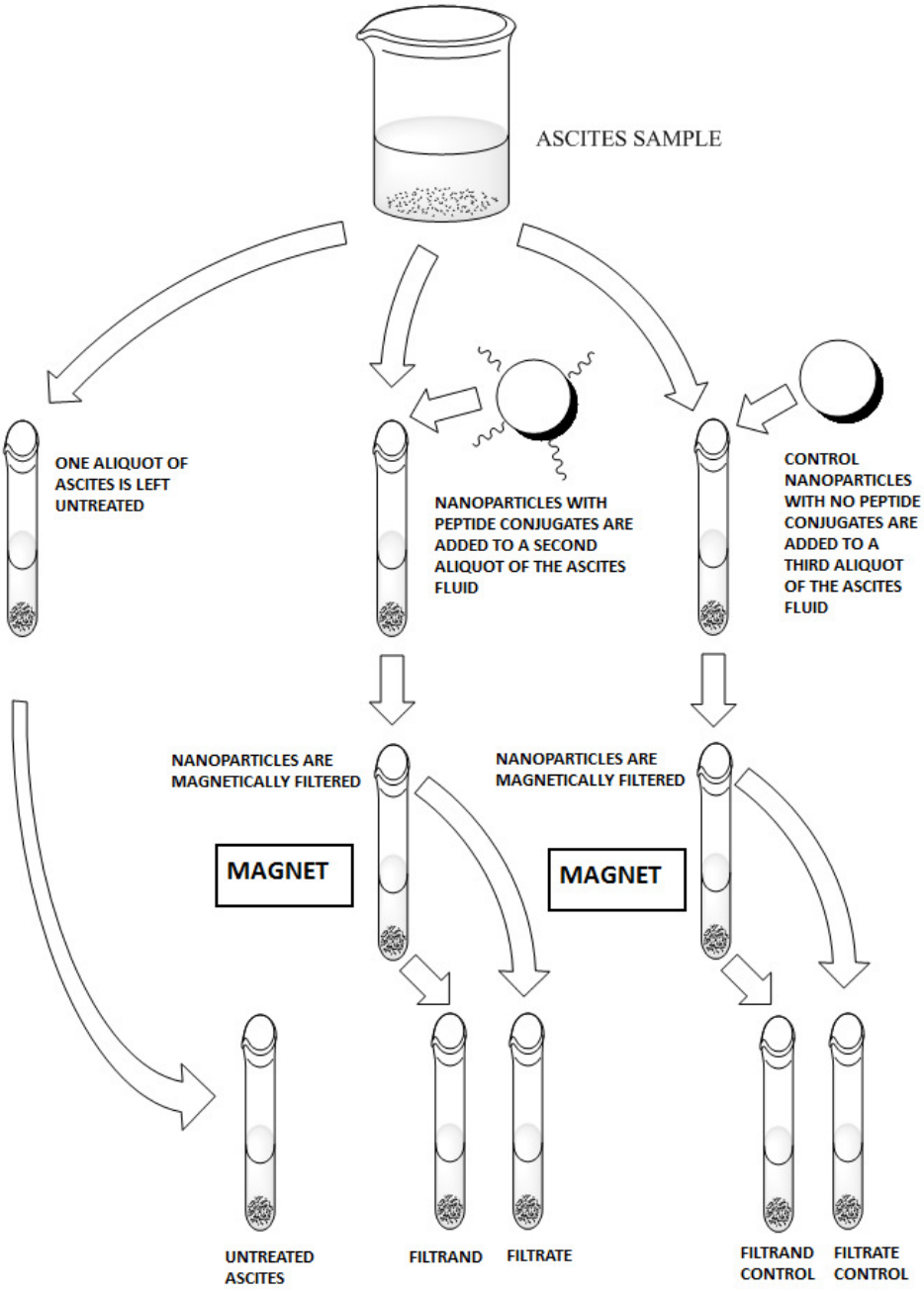


Figure 2.5: Overview of the experimental design used to verify whether magnetic nanoparticles with peptide conjugates were capable of selectively extracting ovarian cancer cells from human ascites samples.

Cell Line

A murine ovarian cancer cell line (ID8) transfected with the gene for green fluorescent protein (GFP) and vascular endothelial growth factor (VEGF) expression was used for the study.[35] VEGF expression would expedite tumor progression by stimulating angiogenesis and abating the immune response. The cell line was obtained through a material transfer agreement with the laboratory of Dr. George Coukos at the University of Pennsylvania.

*Cell Rejuvenation*

Per Zhang et al. [35] Dulbecco's modified Eagle's medium was supplemented with 4% fetal bovine serum, 100 U/mL penicillin, 100 µg/mL streptomycin, 5 µg/mL insulin, 5 µg/mL transferrin, and 5 ng/mL sodium selenite. The cryogenically frozen ID8 cells were slowly thawed at 37$^{o}$ C and transferred to a growth flask containing 10 mL of the prepared medium. Cells were maintained in an incubator at 37$^{o}$ C and a 5% $CO_2$ atmosphere.

*EphA2 Expression*

The ID8 cell lines were tested for EphA2 expression to insure that we could use the YSA peptide to bind it. Ovarian cancer cell lines (ID8 GFP, ID8 GFP VEGF, BG1 and HEY) were plated and grown in 4 well plates. The formulation in Table 2.1 was brought up to 10 mL using distilled water and was added to each well plate after the removal of the growth media. The contents of the plate were centrifuged at 12000 RPM and 4$^{o}$ C

Table 2.1: Cell Lysis Buffer Formulation

| VOLUME | REAGENT | CONCENTRATION |
|---|---|---|
| 200 µL | Tris (pH 7.5) | 20 mM |
| 1.5 mL | NaCl | 150 mM |
| 20 µL | EDTA | 1 mM |
| 40 µL | EGTA | 1 mM |
| 100 µL | Triton X-100 | 1% |
| 250 µL | Sodium Pyrophosphate | 2.5 mM |
| 10 µL | β-Glycerolphosphate | 1 mM |
| 20 µL* | Na3VO4 | 1mM |
| 100 µL* | Protease Inhibitors | 1 µG/mL |
| 10 µL* | PMSF | |
| 500 µL | Glycerol | |

*Stored at 4$^{o}$ or -20$^{o}$

for 5 minutes. The supernatant was transferred to another tube and 10 µL from that tube was used to establish the protein concentration using a Bradford assay (optical density measured at 595 nm). These optical density measurements were used to calculate the equivalent gel loading volumes for each sample. The standard procedures for Western blot analyses were followed[36] and the blots were compared to establish the relative EphA2 expression level for each sample.

Peptide Affinity for EphA2 Receptor

The growth medium in well slides containing ID8 GFP and ID8 GFP VEGF cell lines was removed and supplanted with 2 mL of 0.1 M sodium phosphate buffer, pH 7.4. 100 µL of magnetic $CoFe_2O_4$ nanoparticles (10mg/ml) in aqueous solution and conjugated to the YSA peptide and Rhodamine were incubated with the ID8 GFP and ID8 GFP VEGF cell lines in well slides for 10 min. The slides were washed 3x using the same PBS buffer and then fixed in 100% ethanol. Confocal microscopy (LSM 510 UV, Carl Zeiss Inc.) was used to image the slides and verify the presence of the Rhodamine tagged nanoparticles.

Tumor Model

Understanding the metastatic progression of the tumor model being used was a prerequisite to designing an experiment to analyze whether the proposed therapy could improve longevity. The tumorigenesis of the ID8 cell line expressing GFP and VEGF was compared to that of an ID8 cell line expressing only GFP (Figure 2.6) that served as a control. The results were measured both qualitatively and quantitatively. Mice from each group were euthanized and necropsied at 3-4 time points (2,4,6, and 8 weeks). Sections of the liver, lung, spleen, peritoneal wall (1 cm x 1 cm), and the intestines were viewed and photographed using both bright field and dark field microscopy on an Olympus SZX series stereo scope with green filters (Magnification = 38.5x) and an Olympus DP71 12.5 million pixel digital camera. The GFP being produced by the cells made the metastatic sites easy to locate. The visible fluorescence from the GFP produced by the cancer cells facilitated qualitative comparisons of tumor progression

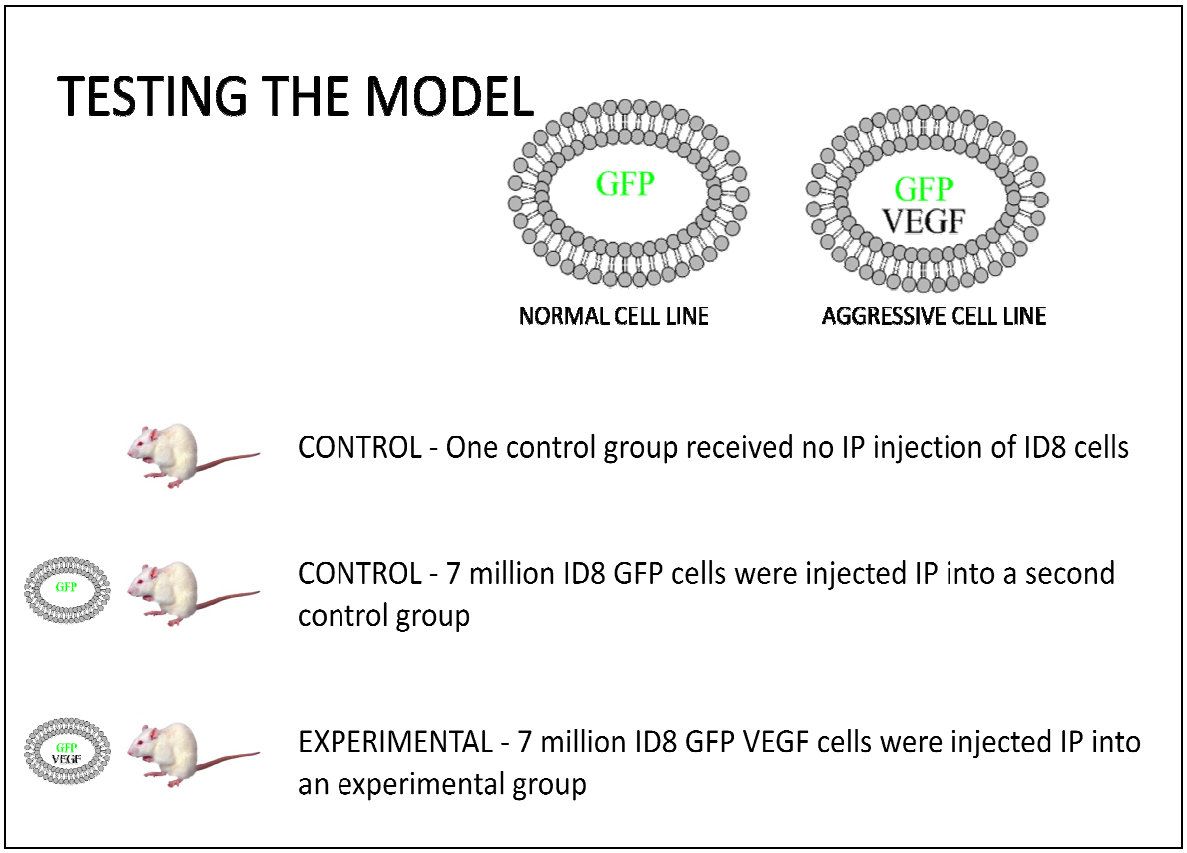


Figure 2.6: Overview of the experimental design used to test the metastatic cancer model.

between the control and experimental groups. The comparative number of metastatic sites was determined quantitatively by homogenizing the tissue sections collected and running 200 microliters of each in duplicate through a fluorescence microplate reader (SPECTRAMAX Gemini, Molecular Devices) to determine their optical densities.[37]

Survival Study

The final part of the study, which is still underway, involved inoculating 6-7 week old female C57BL/6 mice (Black 6) with the ID8 GFP VEGF cell line and treating them at various intervals (Figure 2.7-2.8). Body mass was measured using an analytical balance

three to four days per week . When the body mass was found to exceed 150% of the mass taken at the start of the experiment the mouse was euthanized and the optical density measurements of the homogenized liver and lung sections were taken using a fluorescence microplate reader (SPECTRAMAX Gemini, Molecular Devices).

*Magnetic Filtration Scheme*

Three elimination schemes were devised to remove the MNPs postoperatively. The first (Figure 2.9.A) involved placing a magnetic field at a point exterior to the subject being studied and waiting for a period while the particles began to collect in that region. This idea was quickly abandoned. The approach would require that the nanoparticles be within a close proximity to the magnetic field and assume that no internal encumbrances would block their migration. Removal of the aggregated particles would also be highly invasive requiring the excision of the tissue containing them. The second approach (Figure 2.9.B) consisted of inoculating the subject intraperitoneally with a bolus of MNPs and allowing the MNPs to disseminate ubiquitously throughout the peritoneum. The extracorporeal circuit would cycle the fluids in and out of the peritoneum. A magnetic filtration trap would be a component of the external circuit where the MNPs would be collected as they were cycled out of the organism. For reasons that will be explained in Chapter 6, it was decided that this technique would not be used for the survival study. Instead, the design featured in Figure 2.9.C was used. In this embodiment the MNPs are introduced externally and never enter the organism. An external mixing chamber serves as a first point of contact between the peritoneal fluids

| GROUP | TREATMENT SCHEDULE | # MICE | 2WK | 4WK | 6WK | 8WK |
|---|---|---|---|---|---|---|
| CONTROL GROUP I | NO TREATMENT | 10 | | | | |
| CONTROL GROUP II | INOCULATED WITH CANCER CELLS/ NO TREATMENT | 10 | | | | |
| CONTROL GROUP III | TREATMENT ONLY | | | | | |
| *--SUBGROUP I* | @ 24 HOURS | 10 | | | | |
| *--SUBGROUP II* | @ 24 HOURS<br>@ 2 WEEKS | 10 | | | | |
| *--SUBGROUP III* | @ 24 HOURS<br>@ 2 WEEKS<br>@ 4 WEEKS | 10 | | | | |
| *--SUBGROUP IV* | @ 2 WEEKS | 10 | | | | |
| *--SUBGROUP V* | @ 4 WEEKS | 10 | | | | |
| EXPERIMENTAL GROUP | INOCULATED WITH CANCER CELLS/ TREATMENT | | | | | |
| *--SUBGROUP I* | @ 24 HOURS | 10 | | | | |
| *--SUBGROUP II* | @ 24 HOURS<br>@ 2 WEEKS | 10 | | | | |
| *--SUBGROUP III* | @ 24 HOURS<br>@ 2 WEEKS<br>@ 4 WEEKS | 10 | | | | |
| *--SUBGROUP IV* | @ 2 WEEKS | 10 | | | | |
| *--SUBGROUP V* | @ 4 WEEKS | 10 | | | | |

Figure 2.7: Simplified Gant chart explaining the treatment schedule used for the survival study. Body mass was measured at 2 week intervals. If the mass > 150% of original body mass the animal was euthanized. External images of peritoneal region were taken at 2 week intervals and optical density measurements of GFP content in liver and lungs was assayed at time of necropsy.

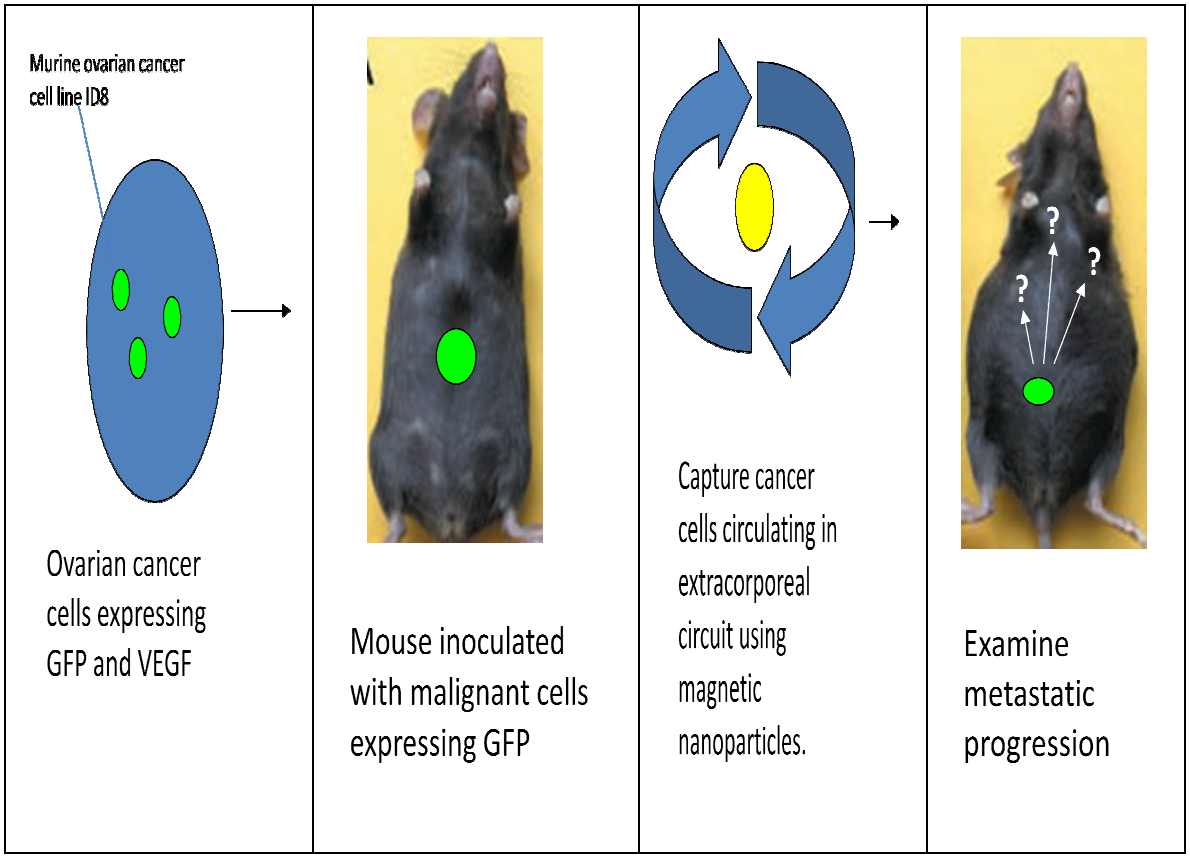


Figure 2.8: Overview of the Ovarian Cancer Survival Study experimental design. Inoculating mice with cancer cells expressing GFP facilitated tracking the metastatic expansion and determining the efficacy of the treatment.

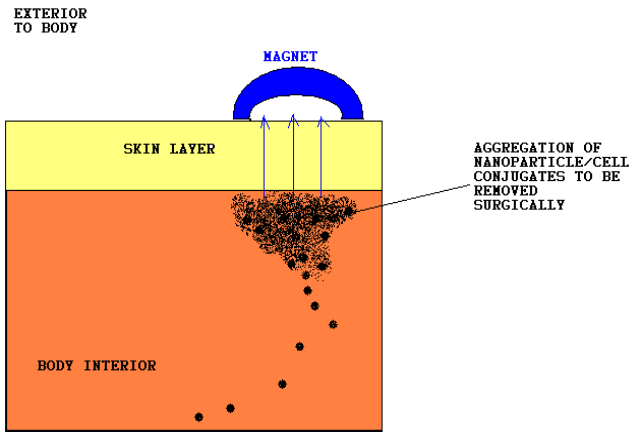


A: Nanoparticle elimination requires invasive surgical procedure after magnetically isolating them at a particular locus.

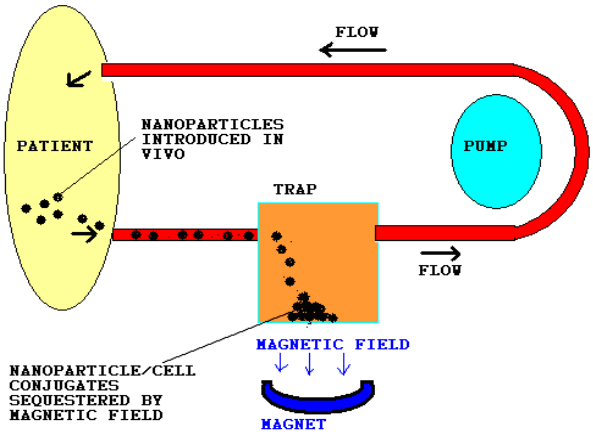


B: Nanoparticles are injected in vivo and then eliminated using an extracorporeal circuit containing a magnetic trap. The technique is minimally invasive.

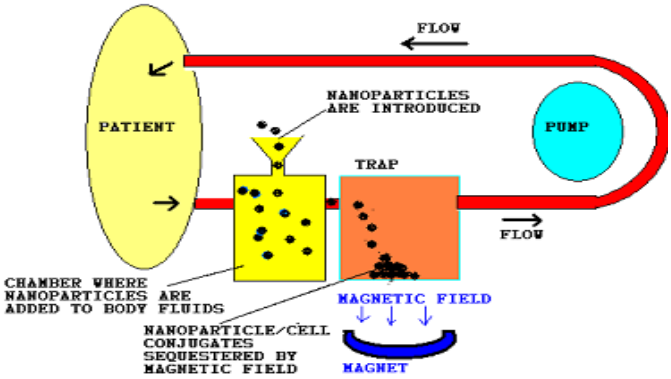


C: Nanoparticles never enter the body and mix with bodily fluids in a mixing chamber prior to being separated by a magnetic trap. Fluids are cycled using an extracorporeal circuit.

Figure 2.9: Different schemes for eliminating nanoparticles post-procedurally.

Table 2.2: Equipment used in survival study.

| COMPONENT | MEASUREMENTS | DESCRIPTION |
|---|---|---|
| Tubing | ID 2.4 mm, OD 4 mm, Wall 0.8 mm | Tygon sterile inert tubing. Formulation S-50-HL. Used for extracorporeal circuit. |
| Needles | 20 Gauge 1” | Used as cannulas to feed and extract fluids |
| Extracorporeal circuit | 49 in, 9.5 mL | Measurements are for the total length and volume of the combined segments (Figure 2.10). |
| Variable Flow Pump | N/A | Fisher (PRDT# 138762). Peristaltic pump used to cycle fluids. |
| Magnetic Filter | 15 mL | Glass vial attached to a magnet. |
| Mixing Cartridge | 15 mL | Glass vial. |

and the magnetic particles. The specifics of the design used are provided in Table 2.2. Figure 2.10 and 2.11 show the actual setup used during the procedure. Arrow #1 points to two stacked neodymium magnets (2 in x 2 in x 4 in) with a magnetic field strength of about 6000 gauss at the surface of each. The magnetic filtration vial (Arrow #2) was strapped to the side of the top magnet. The vial where the magnetic nanoparticles were first introduced (Arrow #3) was placed approximately a foot away from the magnets so that it could remain outside of the magnetic field. Arrow #4 points to the variable flow pump. The pump was set at a flow rate of 10 mL/min. Arrow #5 points to the outlet needle that was used to cannulate the mouse towards the dorsal region of the peritoneal cavity. Arrow #6 points to the inlet needle that was used to cannulate the mouse in the ventral region of the peritoneum. The following procedure was followed using the setup as described:

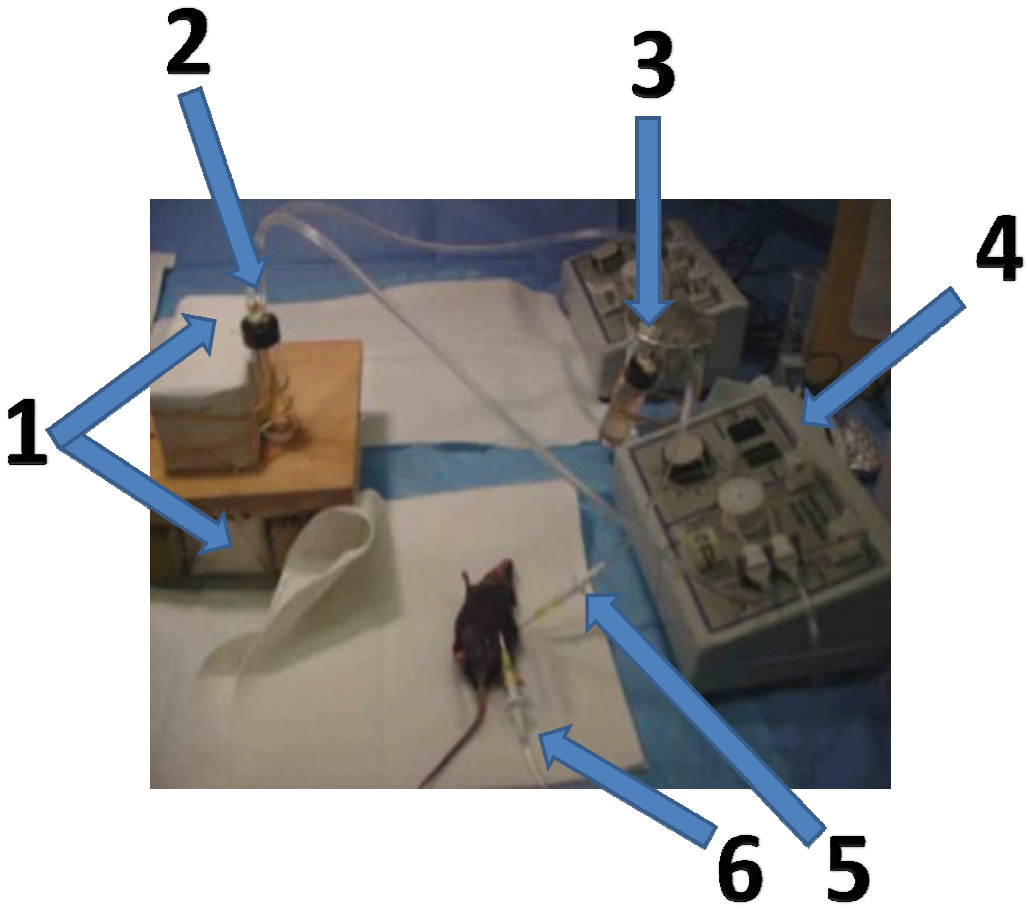


Figure 2.10: Equipment used in the Ovarian Cancer Survival Study. (1) 6000 gauss neodymium magnets (2) Magnetic filtration vial (3) Mixing cartridge where magnetic nanoparticles are first introduced (4) Variable flow pump (5) Outlet cannula (6) Inlet cannula

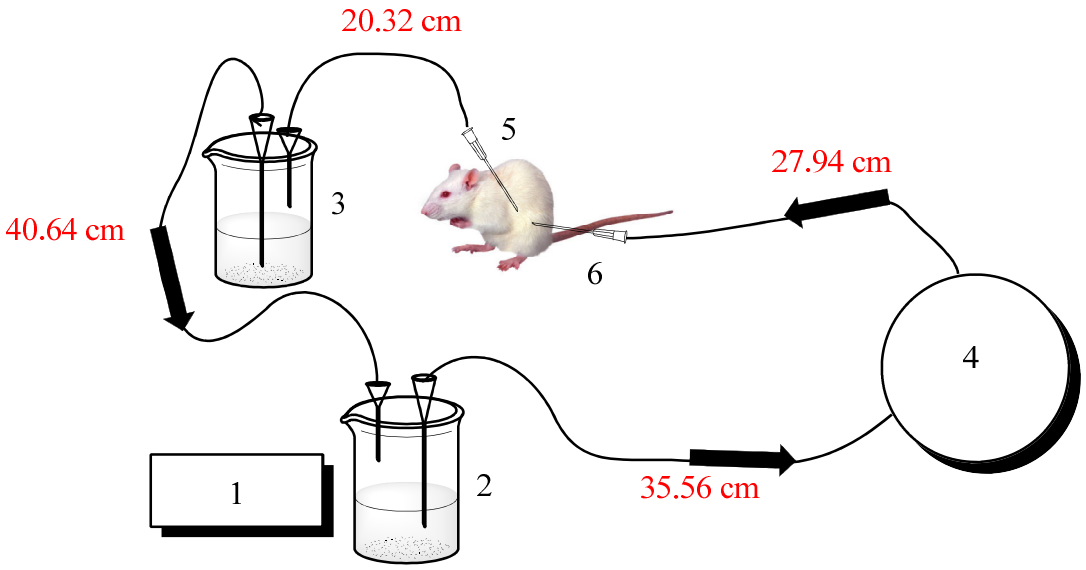

Figure 2.11: Measurements for Tygon tubing used in Ovarian Cancer Survival Study. Numbers correspond to item descriptions in Figure 2.10.

1. The magnetic filtration vial and mixing vial were filled with 15 mL of sterile 0.1 M sodium phosphate buffer, pH 7.5, and attached to the extracorporeal circuit as shown in Figure 2.10.

2. The inlet needle was submerged in a beaker containing a sufficient volume of sterile 0.1 M sodium phosphate buffer to fill the extracorporeal tubing. The variable flow pump was engaged and ran until the fluid had coursed through the entire circuit.

3. Step 2 of this procedure lowered the volume of the two vials. The volume in the magnetic filtration vial was brought back up to 15 mL using the same buffer solution. The volume in the mixing vial was brought up to 14 mL of the same buffer solution and 1 mL of (1g/mL) MNPs (conjugated or not conjugated to the YSA peptide depending on whether

it was the control or experimental group) were also added to the mixing vial to bring its volume to 15 mL.

4. An anesthetized female C57BL/6 was cannulated in the ventral region of the peritoneum using a 20 gauge 1” needle (Arrow #6 Figure 2.10).

5. The outlet needle was placed in a beaker containing greater than 8 mL of sterile 0.1 M sodium phosphate buffer, pH 7.5 and the pump was engaged until 8 mL was drawn from the beaker. It was necessary to fill the mouse’s peritoneal cavity with an additional 8 mL of fluid to prevent occlusion of the needles during the procedure.

6. The outlet needle was removed from the beaker and used to cannulate the mouse on its left flank toward the dorsal region of the peritoneal cavity.

7. The pump was engaged for 20 minutes and stopped and restarted at any sign of occlusion.

8. After the 20 minute session was complete the pump was shut off and the inlet needle was removed and placed into an empty 10 mL graduated cylinder. The pump was re-engaged and the graduated cylinder was brought to a volume of 8 mL. This step was used to insure that the excess fluids were completely removed from the mouse.

9. The mouse was disconnected from the circuit and the pump was again engaged until the tubing and vials were depleted of all fluids. The removed fluids were placed in a falcon tube and centrifuged at 800 RPM, 4$^{o}$ C for 5 min. The supernatant was siphoned out of the falcon tube and any remaining pellet was resuspended in 200 µL of sterile 0.1 M sodium phosphate buffer, pH 7.5. The 200 µL containing the pellet were injected intraperitoneally back into the mouse. This step eliminated the possibility of malignant cell titer reduction from fluids left in the circuit which could otherwise be considered a contributing factor to improving long-term prognoses.

**HIV Capture Study**

Preliminary in vitro studies were run to determine whether MNPs could be used to reduce viral titer (Figure 2.12). MNPs coated with glucuronic acid and conjugated to anti-gp120 and MNPs coated with glucuronic acid and having no antibody conjugates were added to separate aliquots of solutions containing active HIV-1 virus and given a set period (Incubation Time) to bind the gp120 viral epitope. After the set period, the colloids containing the virus and MNPs were placed in a magnetic separation apparatus (Dynal-MPC, Magnetic Particle Concentrator) and given a set amount of time (Capture Time) to collect on the side of the vial closest to the magnetic field. The magnetic filtrate (i.e. remaining solution) was drawn off and tested for p24 concentration using a p24 antigen ELISA (ZeptoMetrix Corp.). Prior to running these studies it was necessary

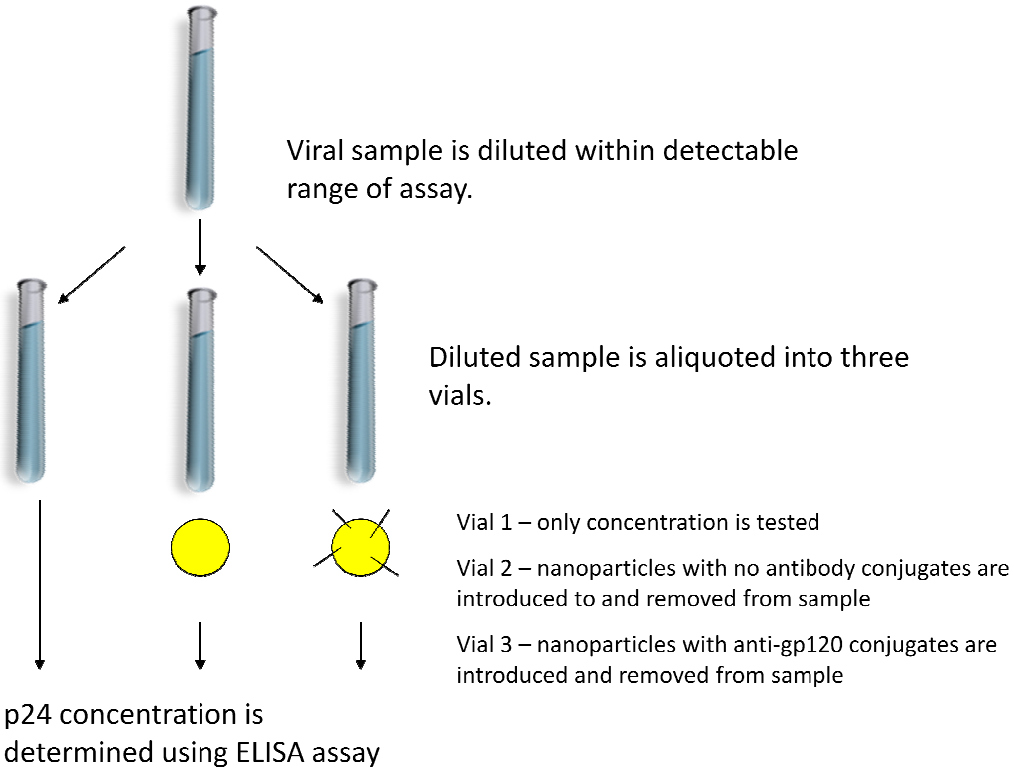


Figure 2.12: Basic concept behind the HIV-1 Capture Study.

to determine whether the residual MNPs in the filtrate might affect viral binding to the antibodies in the ELISA plate. The design for each of these experiments is laid out in the next three sections. The microplate washer used in each of the studies was a Dynex Technologies Ultrawash Plus and the microplate reader was a BioTek Instruments Bio-Kinetics Reader EL312e. The viral sample used was taken from an undisclosed individual and stored by the CDC on 8/26/1998.

<u>Testing MNP Interference with the p24 Assay</u>

The ZeptoMetrix HIV-1 p24 Antigen ELISA (ZMC Catalog# 0801111) was used to determine the p24 concentrations in each of the experiments described in this section. For each run of the ELISA assay it is necessary to include a set of standard concentrations. A calibration curve is created from the optical density values obtained from these standards and the p24 concentrations of the experimental samples are interpolated. To test the effects of the MNPs on the assay, the standards were prepared in duplicate in the microtiter plate as dictated by the assay. The first group was left unaltered and 20 µL of glucuronic acid coated MNPs (10 mg/mL) were added to each of the standards in the second group. The assay was performed as recommended by Zeptometrix and the p24 concentrations of each group were compared. This experiment was repeated using a volume of 10 µL of glucuronic acid coated MNPs (10 mg/mL). The data were normalized to account for the dilution of the sample in the experimental group. The results are discussed in Chapter 7.

HIV-1 Capture Experiment I

A summary of the conditions of the first experiment are provided in Figure 2.13.

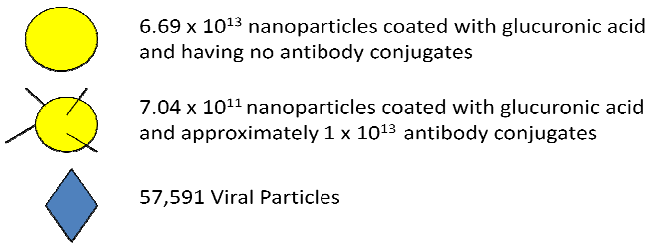


Figure 2.13: Conditions for HIV-1 Capture Study Experiment I.

The summary shows the number of MNPs that were added to the experimental and control vials and the number of viral particles in each vial. The viral particles were suspended in unmodified RPMI cell growth media. The following procedures were performed:

1. Viral stock BaL 8/26/1998 ($1.7 \times 10^{10}$ vp/mL), having been previously stored at -80$^{o}$ C, was thawed at room temperature for 1 hour.

2. The viral concentration was reduced to a level detectable by the ZeptoMetrix HIV-1 p24 Antigen ELISA by performing a 1:9550 dilution with RPMI which provided an approximate concentration of 625,000 vp/mL or 62.5 pg of p24/mL.[29] To perform the dilution 1 µL of the viral stock was added to 954 µL of RPMI. The diluted viral solution was vortexed for 1 min (Vortex Genie 2) and then aliquoted into 14 tubes (50 µL/tube). 450 µL was added to each tube. The 14 tubes were vortexed for about 30 sec each and labeled S1A-S1B for control group I, S2A-S2F for control group II, and S3A-S3F for the experimental group.

3. 10 µL of MNPs (10 mg/mL) without anti-gp120 antibody functions were added to each tube in control group II (S2A-S2F) and the contents were vortexed briefly (≈ 10 sec). Each tube was left at room temperature to incubate for 10 min.

4. 10 µL of MNPs (10 mg/mL) with anti-gp120 antibody functions were added to each tube in the experimental group (S3A-S3F) and the contents were vortexed briefly (≈ 10 sec). Each tube was left at room temperature to incubate for 10 min.

5. The tubes (S2A-F and S3A-F) from control group II and the experimental group were placed in magnetic bead separators (Dynal-MPC) for 10 min.

6. Without removing the tubes from the magnetic bead separators, 450 µL was extracted from each tube and placed in a new tube with the same label.

7. 50 µL of solution was removed from tubes S1A and S1B and discarded.

8. Tubes S1A-S1B, S2A-S2F, and S3A-S3F were ready to be assayed following the procedures outlined in the Zeptometrix HIV-1 p24 Antigen ELISA kit.

HIV-1 Capture Experiment II

The procedures conducted in this experiment were similar to those conducted in HIV-1 Capture Experiment I but it was conducted under different conditions and an additional experimental group was added. A summary of the conditions for this experiment has been provided in Figure 2.14. As before, the summary shows the number of MNPs that were added to the experimental and control vials and the number of viral particles in each vial. The viral particles were suspended in unmodified RPMI cell

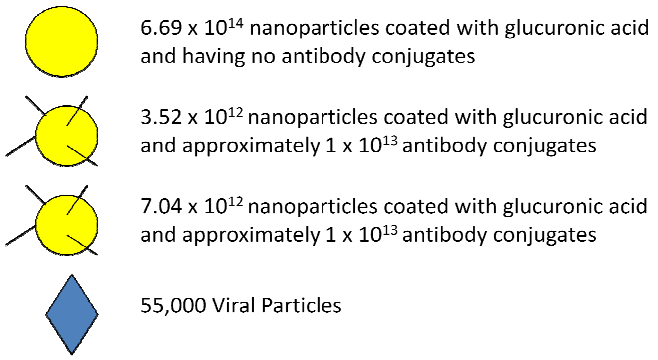


Figure 2.14: Conditions for HIV-1 Capture Study Experiment II.

growth media. The following procedures were performed:

1. Viral stock BaL 8/26/1998 (1.7 x $10^{10}$ vp/mL) was diluted (1:10,000) by first adding 1 µL of viral stock to 999 µL of RPMI, vortexing the solution for 1 min (Vortex-Genie 2), aliquoting the solution into 20 tubes of 50 µL each, and adding 450 µL of RPMI to each tube. Each tube was then vortexed for 30 sec each.

2. The tubes for control group I were labeled S1A-S1B and the tubes for control group II were labeled S2A-S2F. The tubes for experimental group I were labeled S3A-S3F and the tubes for experimental group II were labeled S4A-S4F.

3. Control group I tubes S1A-S1B were only used to measure p24 concentration. Control group II tubes S2A-S2F received 100 µL each of glucuronic acid coated MNPs (10 mg/mL) having no anti-gp120 antibody conjugates. Experimental group I tubes S3A-S3F received 50 µL each of

glucuronic acid coated MNPs (10 mg/mL) with anti-gp120 antibody conjugates. Experimental group II tubes S4A-S4F received 100 µL each of glucuronic acid coated MNPs (10 mg/mL) with anti-gp120 antibody conjugates.

4. Tubes S2A-S2F, S3A-S3F, and S4A-S4F were incubated at 37$^{o}$ C for 30 min after adding the MNPs to the tubes.

5. The capture time was performed for 10 min as described in HIV-1 Capture Experiment I.

**Reaction Impedance Study**

The purpose of this study was to provide a visual proof of concept demonstrating the viability of using MNPs to control reaction kinetics. The reaction being controlled was the chemiluminescent reaction involving luminol. The experimental design was simple. Nanoparticles conjugated to luminol were added to a solution containing the necessary reactants to produce light. A magnet was used to pull the MNP/luminol conjugates from solution to halt light production. The conjugation strategy used to bind luminol to the surface of the MNP is covered in the next section. The following procedures were followed to create the reaction solution:

1. A stock solution of dilute household bleach (Stock A) was created by adding 10 mL of household bleach to 1 L of distilled water.

2. 10 mL from Stock A was added to 5 mL of 0.1 M NaOH in a reaction vial.

3. A 2000 gauss magnet was placed beside the reaction vial and 100 µL of the MNP/luminol conjugate were pipetted into the vial.

## Surface Modification Strategies

There are a plethora of conjugation strategies suitable for binding biocompatible coatings and ligands to the surface of nanoparticles.[38] The methods that will be presented here are the few that I found to be the most useful and convenient for my particular needs. In many of the described procedures it is mentioned that the samples were resuspended in distilled water. For in vitro applications aseptic conditions were unnecessary but when preparing samples for in vivo use the water was always sterilized (Barnstead PVdry2 Sterilizer) and the conjugations took place within an air purifier (Labconco Purifier Delta Series Class II) to mitigate the pyrogenicity or immunogenicity of the sample. In addition, unless otherwise stated, all conjugations took place at ambient temperature. Nanoparticles conjugated to peptides and antibodies were always stored, post-conjugation, at 4º C.

### Surface Binding with Carboxyl Groups and Hydroxyl Groups

#### Hydroxyl Group Conjugations

Some polymers, like Dextran, that were used to coat nanoparticles relied on hydrogen bonding interactions to remain adsorbed to the MNP surface. Hydrogen bonds are much weaker than ionic or covalent bonds and often lead to disaggregation of the coating over short periods. To retard disaggregation some groups employed a highly toxic reagent to crosslink the Dextran molecules. The cross linking created a

mesh of Dextran around the particle that was more stable but the procedure had to be performed in a fume hood and purification of the product was paramount before it could be used in vivo. I initially started working with Dextran in the early stages of my in vitro studies but quickly abandoned it in search of another more stable polysaccharide coat that would have the same non-immunogenic properties and be easier to work with.

*Dextran*

The MNPs were coated with Dextran by adding 200 mg MNPs to 2.5 mL of 0.5 M NaOH (Vial 1). In a separate vial (Vial 2) 200 mg of Dextran was added to 2.5 mL of 0.5 M NaOH. The 0.25 " diameter sonication tip from a Sonics Vibra Cell sonicator was lowered into Vial 1 below the liquid surface level and the solution was sonicated for 15 min with a temperature setting of 25$^{o}$ C and a 38% Amplitude. After 15 minutes, Vial 2 was added to Vial 1 without stopping the sonication process and the combined solutions were sonicated continuously overnight. The sample was magnetically filtered using a 2000 gauss magnetic, washed 3x using distilled water, and resuspended in same.

<u>Carboxyl Group Conjugations</u>

Prior to conjugating the nanoparticles to molecules with carboxyl functions, the hydroxyl groups on the surface of the nanoparticle needed to be deprotonated. This was typically done by adding the nanoparticles to a solution of 5 M NaOH and sonicating

the MNPs for 30 min with a Fisher Sonic Dismembrator 60 at a power setting of 13. Post sonication the compound having carboxyl functions would be added to the alkaline solution. If the molecule contained multiple carboxyl groups it would be added in a molar excess of 10-100 fold to that of the nanoparticles. The molar excess was necessary to limit polymerization of the product and insure adequate surface coverage of the nanoparticle. The alkalinity of the solution acts to dissociate the carboxylic function on the ligand to a carboxylate anion which coordinates with the particle surface.

*Terepthalic Acid Coatings*

Terepthalic acid was a molecule used to conjugate luminol to the surface of the MNPs. This molecule was chosen as a linker molecule because its carboxylate anion could form an amide bond with luminol's primary amine group. The amide would then contain a carbonyl that could act as a hydrogen acceptor and a secondary amine that would act as the hydrogen donor promoting the solubility of the conjugate.

To add terepthalic acid to the surface of the MNPs, 70 mg of $CoFe_2O_4$ and 300 mg of terepthalic acid were added to a 70% ethanol solution and sonicated for 2 hours (Fisher Cell Dismembrator 60, Power Level = 13). The solution was left to incubate at room temperature overnight without stirring or sonication. The reaction vial contained a grey precipitate the next day. The precipitate was magnetically filtered and washed 3x to remove the ethanol and unbound terepthalic acid. The washed MNPs were then re-suspended in distilled water and the procedure described under coupling carboxyls to amines was used to conjugate the luminol to the particle surface.

*Polygalacturonic Acid Coatings*

Polygalacturonic acid is a form of polymerized galacturonic acid. The molecule is more commonly known as pectic acid and is a constituent of all plant cell walls. The molecule is made up of a linear chain of galacturonic acid units bound together by 1α-4 glycosidic links. Galactose is a glucose analog and polygalacturonic acid is similar to Dextran but also contains carboxyl groups attached to the 6th carbon of the galacturonic acid rings. Alone, polygalacturonic acid is virtually insoluble in aqueous solution but capping its carboxyl groups with hydrophilic molecules promotes its solubility in aqueous solution. A typical polygalacturonic acid molecule possesses many carboxyl functions and it is necessary to introduce them in molar excess over the number of nanoparticles they are being conjugated to.

The conjugation of polygalacturonic acid to the cobalt ferrite surface was simple and straightforward. The nanoparticle hydroxyls were deprotonated in 5 M NaOH at a concentration of 1-10mg/mL as previously mentioned and 30 mg/mL of the glycoside was added to the solution. The solution was sonicated for 2-3 hours (Fisher Sonic Dismembrator 50 – Power Level of 13). Post-sonication the sample was magnetically purified and washed with 0.1 M sodium phosphate buffer three times before being resuspended in distilled water.

*Glucuronic Acid Coatings*

The glucuronic acid molecule is also a glucose analog and contains a single carboxyl group at carbon 6. Polymerization was not a concern when conjugating this molecule to the MNP surface and smaller molar ratios could be used.

**Coupling Carboxyls to Amines**

When the hydroxyl of a carboxyl group is supplanted with an amine, an amide is formed (R1(CO)NR2R3). Several characteristics of the amide bond make it an attractive method of conjugating ligands for use in vivo. The bond is stable under physiological conditions. Amide hydrolysis typically requires strongly acidic conditions and is a very slow process at neutral pH. The carbonyl group and secondary amine in the amide structure can participate in hydrogen bonding to promote the solubilitly of the conjugate in protic solvents. Amide bonding was often used when the nanoparticle surface contained carboxyl functions and the ligand contained a conjugable amine group with no competing carboxyl groups that might lead to the polymerization of the product unless this polymerization did not adversely affect the ligands function. It was also possible to avoid polymerization by first capping the competing carboxyls with dihydropyran and later cleaving the cap with a dilute acid.

<u>EDC</u>

1-ethyl-3-(3-dimethylaminopropyl) carbodiimide hydrochloride (EDC) forms an active ester leaving group called o-acylisourea with a carboxylate group. The leaving group will react with an amine group to form an amide bond. This conjugation strategy can be used effectively but is more appropriate when low conjugation yields are desired owing to inherent issues with the stability of the intermediate.

When using EDC as a means of conjugating ligands to surface carboxyl groups on nanoparticles, the nanoparticles were first dissolved at a concentration of 1-10 mg/mL in either distilled water, 0.1 M sodium phosphate, pH 7.4, or 0.1 M MES, pH 4.7. The ligand being conjugated would then be added to the nanoparticle solution in a molar

excess that was varied based on the molecular weight of the ligand, the number of conjugable amines on the ligand, and the desired number of nanoparticle surface functions. Next, an amount of EDC was added that would bring its concentration to 0.5-0.1 M. The resulting solution was vortexed for two hours and then the sample was magnetically purified, washed 3-10x with 0.1 M sodium phosphate, pH 7.4, and resuspended in distilled water. Washes were always performed in PBS buffer solutions because the hydrogen bonding opportunities were not as prevalent as in aqueous solution which generally decreased the time needed to purify the sample magnetically.

Sulfo-NHS and EDC

Sulfo-NHS and the carbodiimide EDC are both soluble in aqueous solution and can be used synergistically to form amide bonds more efficiently. As mentioned, EDC will react with a carboxylate to form o-acylisourea as an active ester living group. However, the longevity of the intermediate state prior to its hydrolysis in aqueous solutions is brief and slow to react with target amines. Conjugation will not take place if the amine cannot react with the intermediate prior to the hydrolysis event. The hydroxyl group on Sulfo-NHS will quickly react with the EDC intermediate forming a hydrophilic reactive ester with the molecule that originally contained the carboxylate. This reactive ester, in turn, can expeditiously bind amine functions.

To conjugate ligands having primary amine functions to a nanoparticle surface coated with a molecule having carboxyl functions, the coated nanoparticles were dissolved (1 mg/mL) in a 0.1 M sodium phosphate buffer solution, pH 7.4. The ligand

was then added directly to this solution. The concentration could be based on the number of desired conjugates. In the experiments that will be described later in which the peptide GGGGYSAYPDSVPMMSK is the ligand conjugated, the concentration used was 1 mg/mL. EDC and Sulfo-NHS were then added to the solution in amounts that would bring their concentrations to 0.1 M and 5 mM respectively. The solution was vigorously vortexed for 2 hours. The sample was purified using a 5000 gauss magnet and washed 10 times with 0.1 M sodium phosphate buffer solution to remove unconjugated ligands and by-products. The washed nanoparticle/ligand conjugates were then resuspended in distilled water.

**Aldehyde to Amine Coupling via Reductive Amination**

An aldehyde and an amine can form a Schiff base and then be reduced to a stable secondary amine link using a reducing agent. This conjugation strategy was effective when nanoparticles were coated with glucuronic acid, Dextran, or polygalacturonic acid because these molecules contained hydroxyls that could easily be oxidized to form reactive aldehydes using sodium periodate. For polygalacturonic acid this was often a desirable alternative to having to first protect the competing carboxyl groups on the ligand to which it was being conjugated.

<u>Glucuronic Acid, Dextran, and Polygalacturonic Acid</u>

Nanoparticles previously coated with glucuronic acid or a glycan could remain in aqueous solution or could be magnetically filtered from aqueous solution and

resuspended in 0.2 M sodium bicarbonate, pH 9.6. In either case, their concentration was adjusted to 10 mg/mL. A stock 0.088 M solution of sodium periodate was created in the dark by adding the sodium iodate to distilled water. 100 microliters/mL of the stock solution was added to the nanoparticle solution and allowed to react in the dark for 15-20 minutes. Next, the magnetic particles were purified using a 5000 gauss magnetic and the filtrate was poured off. The magnetic nanoparticles (filtrand) were resuspended at a concentration of 10 mg/mL in 0.2 M sodium bicarbonate, pH 9.6. The ligand containing the amine was also dissolved in 0.2 M sodium bicarbonate, pH 9.6 at a concentration of 10 mg/mL or higher, depending on the desired number of conjugates, and pooled at a 1:1 ratio with the nanoparticle solution. The combined solutions were given two hours to react and then 10 µL of sodium cyanoborohydride (5 M) was added per mL of the reaction solution. The sodium cyanoborohydride was taken from a 5 M stock solution created by dissolving sodium cyanoborohydride in 5 M NaOH. The reaction ran for 30 minutes while vigorously shaking. It was essential that the work with sodium cyanoborohydride be performed under a fume hood owing to its high toxicity. Unreacted aldehydes were capped by adding 2-aminoethanol, pH 9.6 (50 µL per mL reaction solution) and also reacted for 30 minutes. The final preparation was magnetically purified and washed 10x with 0.1 M sodium phosphate buffer to remove any unreacted agents and byproducts. The sample was finally resuspended in aqueous solution at a concentration of 1-10 mg/mL.

**Chalcogen Bond Formation**

To synthesize the nano-triggers for the drug delivery project that will be described in Chapter 3 we began by activating cobalt iron ferrite nanoparticles with sodium hydroxide and then coating them with Dextran using the previously mentioned procedure. L-selenocystine's primary amine group was conjugated to the surface of the Dextran coated particle by following the reductive amination procedure previously described. L-selenocystine was used because the pKa of the selenide function is 5.2 and would mean that the diselenide would be unstable enough at neutral pH to dissociate into selenate groups.

To synthesize the nano-carriers the selenide side of the carrier was created in the same manner as the nano-trigger, however once the dimer of two particles linked by a diselenide was isolated it was placed into a nitrogen environment where 5 mg of DTT was added as a reductant and allowed to incubate until needed (approximately 3 hours later). The DTT was used to reduce the diselenides to selenols and the nitrogen environment was necessary to prevent premature oxidation.

Although no prior studies could be found where alkyl halides were changed to tellurols it was assumed that the chemistry was similar to that demonstrated by Klayman et al.[39] who successfully added thiol and selenide groups to alkyl halides using elemental sulfur and selenium combined with super hydride.

$NaBH_4 + Se + 3C_2H_5OH \rightarrow NaHSe + B(OC_2H_5)_3 + 3H_2$ *Klayman et al. reaction*

$NaBH_4 + Te + 3C_2H_5OH \rightarrow NaHTe + B(OC_2H_5)_3 + 3H_2$ *modified reaction*

This was an accurate assumption and was achieved in the following manner: 2-aminoethylbromine in HBr was produced by combining 0.9 mL of 2-aminoethanol with 2.0 mL of HBr (a stoichiometric excess) and allowed to react for 2-3 minutes (until cessation of smoking and bubbling) before adding 30 mL of THF. The solution (Solution A) was magnetically stirred until needed for use (approximately 2 hours later). Solution A was to be mixed in a nitrogen environment with another solution and was placed there along with the coated MNPs before beginning the next step. The next step involved the synthesis of NaHTe which was used to convert our alkyl halide to a tellurol. In a nitrogen environment, 2.78 mmol of grey Te was added to 5.8 mL of $Li(C_2H_5)_3BH$ (5.8 mmol). Safety precautions were necessary owing to the combustability of the compound in the presence of oxygen. A pinkish white solution formed after about 20 minutes of magnetic stirring. At this point 3.0 mL of THF was added and the solution (Solution B) was stirred for an additional 20 minutes. Solution A and B were then combined and allowed to incubate with magnetic stirring for 1-2 hours. Most of the solvent evaporated during mixing and we were left with roughly 8.0-9.0 mL of solution. 1 mL of this was added to the MNPs that had been sitting in DTT and this combination was immediately removed from the nitrogen environment. The objective was to oxidize the tellurol and selenol groups to form tellurol selenide bonds. The oxidation process was facilitated by adding peroxide to the solution. The peroxide had to be added drop-wise with a pipette in microliter increments. In our case, 200 microliters was sufficient. The solution was allowed to mix on a stir plate for one hour in open air before magnetically separating and washing the particles in distilled water three times. After the third wash the separated particles were re-suspended in 0.1 M NaOH. 1.0 mL of FITC in DMSO (20 mg/mL respectively was added to the suspended particles and the solution was allowed to incubate overnight at 4 degrees Celsius. In the trial involving

acetylsalicylic acid, FITC was supplanted by aspirin in aqueous solution. The following day the particles were again magnetically separated and washed with distilled water several times to remove excess FITC and NaOH and were then ready to use.

# CHAPTER 3

# DRUG DELIVERY

Magnetic nanoparticles have been proposed as possible vectors for targeted drug delivery systems. The magnetic properities of these particles allow for a more controlled biodistribution. Although the attachment of small molecules, peptides and other therapeutic compounds to the particle surface has been facile, the engineering of their controlled release has been more challenging. In this chapter I describe the phased delivery of a therapeutic package using magnetic nanoparticles that are classified as either nano-carriers or nano-triggers. The major difference between the particles is their surface modification. For magnetic nano-carriers, the surface of the nanoparticle is chemically modified with certain types of linker molecules. These linker molecules utilize chalcogen-chalcogen bonds to tether the particle's cargo which may include various drugs, peptides or nucleic acid chains. The nanoparticle-drug conjugate can be sent to a targeted region using an external magnetic field. The surface of the other particle, the nano-trigger, is modified with chalcogenides. These nano-triggers can exist as individual particles or as dimers bound by a chalcogen-chalcogen bond.

## Introduction

After translation and before its final deployment a protein must assume its tertiary and quaternary conformations. Mistakes can be made during this process and there are biological checks and balances to insure that they are remedied. Protein disulfide isomerase (PDI) is one such means of insurance. PDI contains thiol functionalities that serve to break disulfide bonds that hold nascent protein structures together and give them another opportunity to fold correctly. The latter example is an

oxidation by which two thiol hydrides pass to the sulfurs engaged in the disulfide bond. But once reduced, PDI can just as easily accept these hydrides back, again resulting in reformation of the original disulfide bond. It was conceivable that a functional carrier and release mechanism could be designed using the same principal if an element of selectivity could be added during the cleavage process and if the exchange could take place at a neutral physiological pH. Selenyl sulfide bonds seemed a logical means of achieving this. Further research showed that this concept has been extensively employed in phase tag chemistry and studies have shown that selenyl sulfide bonds can be reduced more easily by thiol groups than disulfide bonds.[40]

Chalcogens are also known as Oxygen Family elements and include oxygen, O; sulfur, S; selenium, Se; tellurium, Te; polonium, Po and ununhexium, Uuh. The chemical properties of the chalcogenides were covered in Chapter 1. It was shown that in the chalcogen family reductive strength is inversely proportional to atomic size and dichalcogenide bond strength is independent of atomic size. This dichotomy affords some interesting functionality that lends well to both speed of function and selectivity when employed in a carry and release mechanism. For example; a particle containing a thiol substituent encountering a selenyl sulfide bond will selectively exchange with the sulfide and free the selenol. A free selenol will not have the reductive strength to replace another sulfide in a disulfide linkage and is unlikely to reattach. The same scenario applies to a selenol substituent encountering a tellurol selenide bond. The selenol binds to the selenide side forming a diselenide link and the tellurol side is freed. Kinetics studies have shown that the speed of a selenide exchange with a selenyl sulfide linkage is about $1.67 \times 10^7$ times faster than the exchange of a thiol with a disulfide linkage (kinetics reference). It was the characteristic speed and selectivity that made

this chemistry a viable mechanism for drug delivery and the mechanisms legitimacy was tested by carrying and releasing fluorescent tags and drugs donated by the NIH.

There was still one problem that begged revision. Cysteine is an important constituent of many proteins. The disulfide linkages formed between cysteine residues can be important to the maintenance of a protein's structure.[41] It was conceivable that if cell membrane surface receptors or other proteins contained reduced thiol groups and a magnetic particle containing a selenyl sulfide linkage was introduced systemically, thiol/dichalcogenide exchange could take place between the selenyl sulfide bond of the particle and the cell membrane receptors. If this exchange took place only at the tumor site when employed as a cancer drug delivery mechanism it would be of little consequence, save possible complications with the particle elimination post treatment. However, it was entirely likely that these particles would contact many non-cancer cells on their way to the site and any exchange there would be very undesirable. In vitro tests (Figure 3.1-3.3) verified both cell surface binding and toxicity toward the cell lines tested. So as stated, this issue had to be remedied. The formation of diselenides is much less common than that of disulfides in vivo. This may have to do with the decreased stability of the bond owing to its lower bond dissociation energy. Although there was little to no information on the use of tellurol selenide linkers it seemed logical that incorporating them into the delivery mechanism might not only increase the speed of release but also preserve the selectivity. But, more importantly, it was theorized that the presence of a mechanism containing a selenol or diselenide trigger and telluride

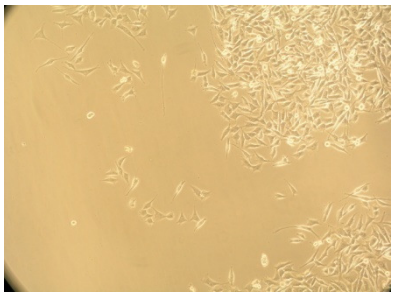

Figure 3.1: HEY cell line prior to introducing nanoparticles with S-Se dichalcogenide bonds to peptides (bright field, 10x objective).

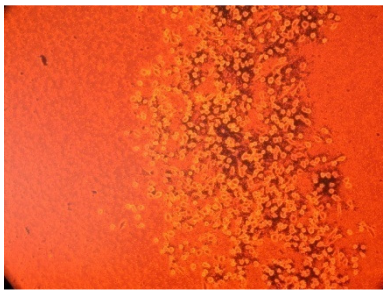

Figure 3.2: Agglutination of nanoparticles with S-Se dichalcogenide bonds to peptides around cell membranes (bright field, 10x objective).

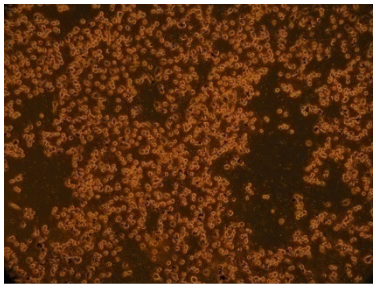

Figure 3.3: Shows rounding up of HEY cells after exposure to nanoparticles with S-Se dichalcogenide bonds to peptides (bright field, 10x objective).

selenide linked carrier would not interfere with the omnipresent thiol groups in vivo. To date, our research has shown that this is precisely the case.

In general, the mechanism works as follows: The first particle (Particle I) contains a tellurol selenide cross linkage to a package (i.e. fluorescent tag, drug, etc). It is conceivable that the package or drug could be conjugated directly to the particle or encapsulated in a structure like a liposome and then conjugated to the particle. The tellurol group is conjugated to the package side and the selenol is conjugated to the particle side. The second particle (Particle II) contains selenol substituents or a diselenide bond between two particles. The diselenide selenocystine was used for this procedure because the selenol group of selenocystine has a pKa of about 5.2 which would mean the diselenide would dissociate to selenates at neutral pH. Theoretically, Particle I could be introduced into an organism and sequestered at a target site magnetically. Particle II could be introduced to the organism sometime later where it would eventually arrive at the target site and also become sequestered magnetically. A selenol functionality on Particle II would participate in an exchange with the tellurol selenide bond on Particle I forming a preferential diselenide bond with the selenium and liberating the tellurol group and attached package (See Figure 3.4-3.5). The use of a telluride selenide bond is key to the selectivity of the mechanism. Otherwise, as mentioned in the PDI scenario it is possible that the package, having a selenide group too, would simply reattach to another magnetic particle.

As a proof of concept, one group of Dextran coated nanoparticles was tagged with Fluorescein Isothiocyanate (FITC) using the tellurol selenide crosslinker and another was conjugated to the well known acetylsalicylic acid using the same linkage. Figure 3.6 shows the molecular structure of acetylsalicylic acid and how it was expected to be

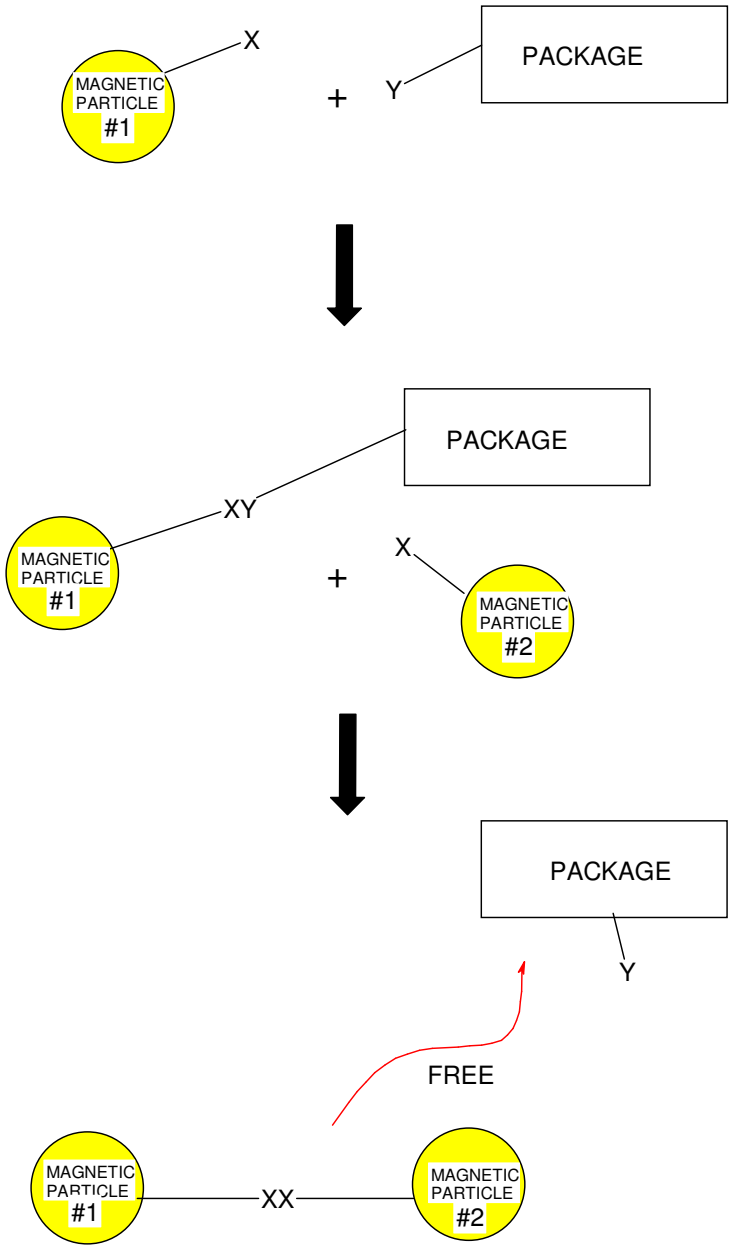


X = S when Y = Se

X = Se when Y = Te

Figure 3.4: Basic concept behind the dichalcogenide bonding and release mechanism showing how a Se-Te or S-Se bond could be used to carry and release a package attached to a magnetic nanoparticle.

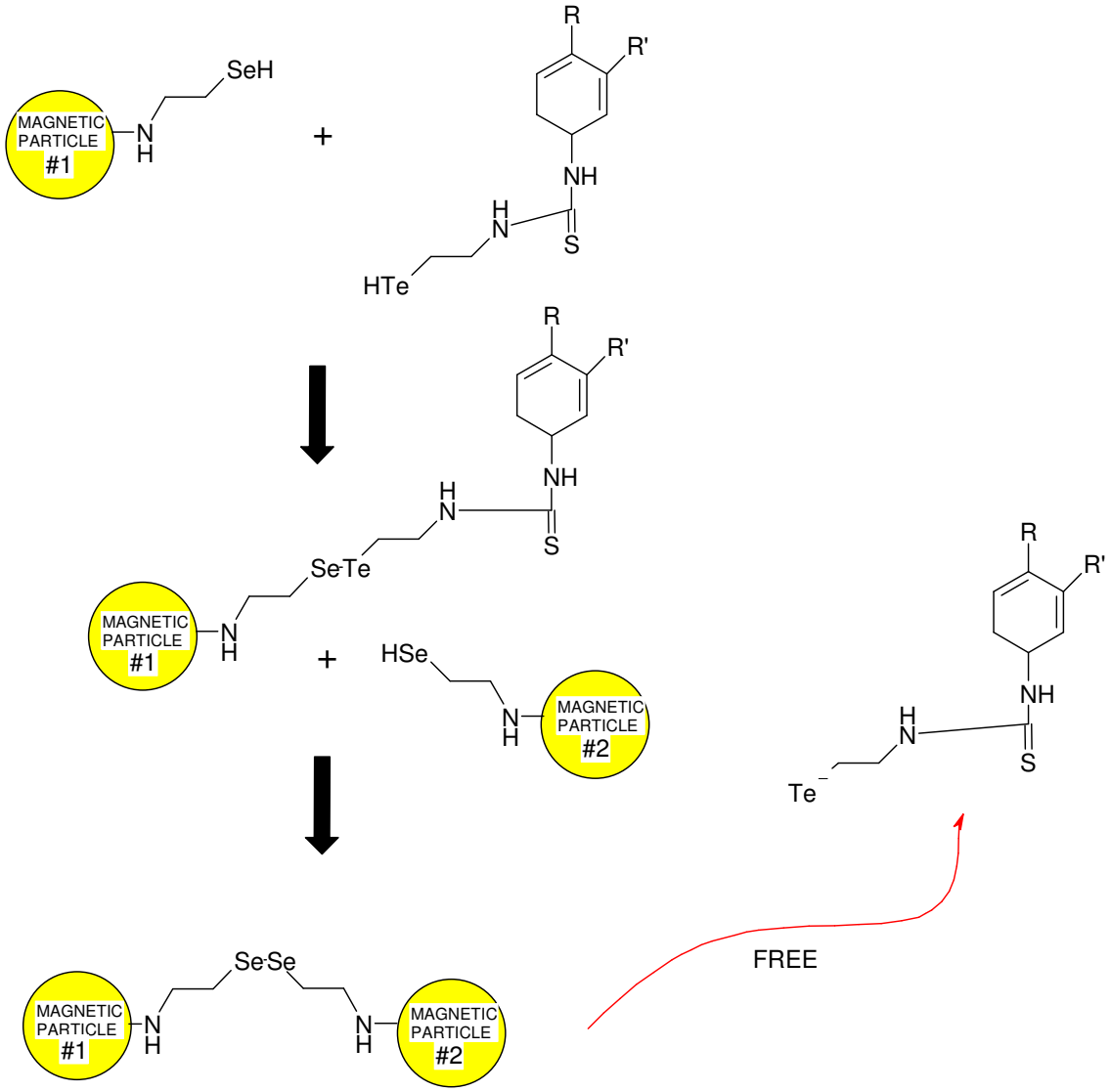


Figure 3.5: Illustration of how dichalcogenide bonds and chalcogen functions can be used to release packages bound to magnetic nanoparticles.

altered after its release from the magnetic nanoparticle. The conjugation strategy used to form the dichalcogenide link has been described in detail in Chapter 2. By using the FITC conjugate it was possible to visualize the successful formation of the bond using confocal microscopy (LSM 510 UV, Carl Zeiss Inc.). Figures 3.7.A -3.7.D are confocal images (excitation wavelength = 488 nm). The green fluorescence is confirmation that

FITC is bound to the magnetic nanoparticle surface. In Figure 3.7.A the bright field levels were raised in the photo so that it was evident that the FITC was bound to the aggregations of MNPs.

| | |
|---|---|
| 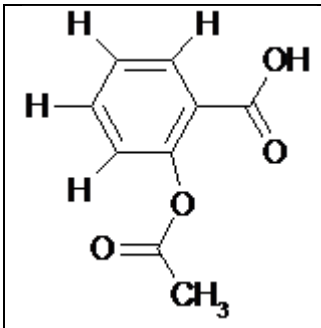 | 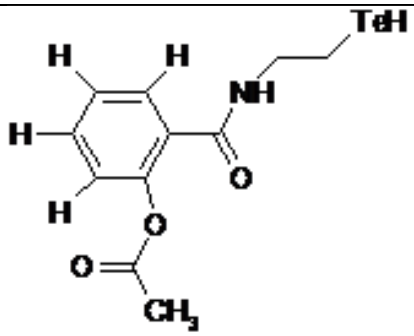 |
| Acetylsalicylic Acid | Aspirin modified after release. |

Figure 3.6: The molecular structure for acetylsalicylic acid and it's expected altered structure after being released from the magnetic nanoparticle.

| | |
|---|---|
| A: 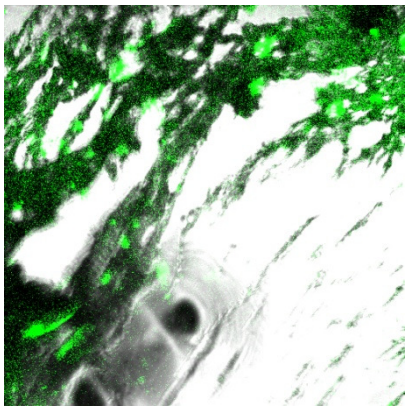 | B: 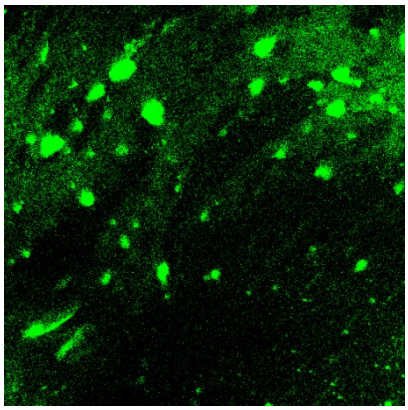 |
| Combination of bright field and dark field exposure at 60x. FITC is bound to aggregated particle bands. | Dark field exposure at 60x. Fluorescence confirms FITC is conjugated to MNP. |

Figure 3.7A-D: Confocal images of FITC bound to magnetic nanoparticles using a tellurol selenide link.

| C: | D: |
| --- | --- |
| 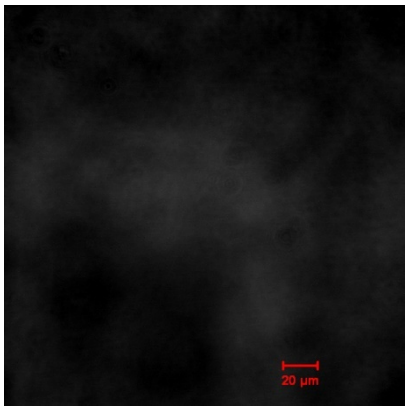  | 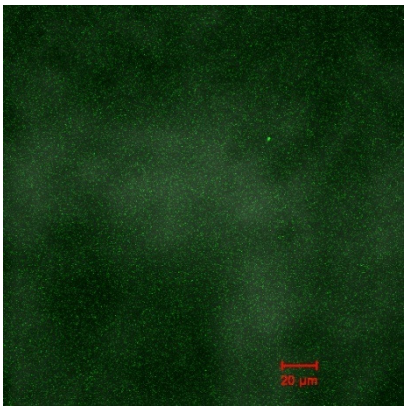  |
| Bright field image at 40x. | Dark field image at 40x. Fluorescence is visible throughout image indicating wide spread conjugation of FITC. |

Figure 3.7A-D continued

**Results and Discussion**

In both experiments involving the conjugation of aspirin or FITC, the introduction of the nano-trigger, containing a diselenide, was shown to initiate release. The release was conducted within a chamber slide filled with distilled water. Under natural light the nano-carriers were introduced to the chamber. For the trial involving the FITC tagged nano-carriers, the chamber slide was placed over the objective of an Olympus IX70 inverted microscope. The natural light was turned off and the epi-flourescent (mercury arc) lamp was turned on. The FITC tags could be seen as widely dispersed throughout the solution. A magnet was placed on the side of the chamber and the flourescent tags were quickly pulled to that side. Immediately, upon contact with other particles release began to take place. This initial release eventually subsided and additional release of the FITC tags was triggered by addition of the nano-triggers

into the solution. The release of the aspirin was conducted in the same manner. However, fluorescent microscopy was unnecessary. The release was verified by analyzing the particles before and after they were agglutinated magnetically and by analyzing the composition of the solution once the particles were extracted. Figure 3.8 shows the electrospray ionization mass spectrometry (ESI-MS) data obtained from the sample after the aspirin release trial. The molecular mass of aspirin is 180.175 atomic

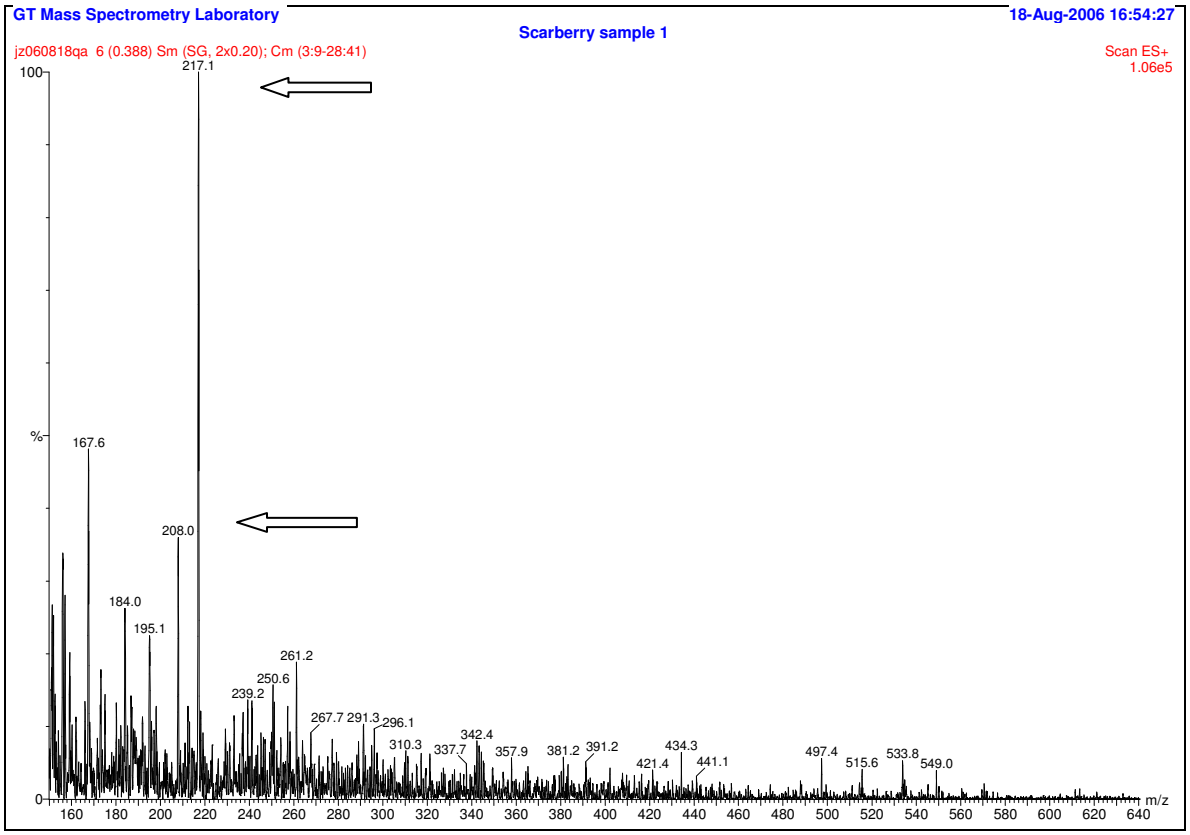

Figure 3.8: EIS-MS data for release of acetylsalicylic acid using a labile Te-Se bond.

mass units (u). The molecular mass of the structure containing the tellurol is 334.83 u. None of the peaks in the spectra appear to correspond to the expected value. However, there are two prominent peaks for masses of 208.0 u and 217.1 u. ESI-MS typically

makes use of acidic solvents that would be likely to dissolve the tellurol. If this were the case then the expected mass of the complex released would be around 207.23 u which is very close to the mass of the peaks in the spectra.

As mentioned one of the initial reasons for employing the Te-Se bond was to avoid toxic interactions with cells in vivo. The experiment illustrated by the results in Figure 3.1-3.3 was repeated with MNPs conjugated to FITC using the TeSe linkage. The MNPs were incubated at 37$^{o}$ C and an atmosphere of 5% $CO_2$ for a period of 15 minutes with ovarian cancer cells (HEY, ≈2 million) that had been growing in single chamber slides. After the 15 minute incubation period the cells were washed with PBS 3x and viewed using bright field and dark field microscopy (488 nm excitation). Figure 3.9.A shows a bright field image of the HEY cells prior to incubation with the MNPs. Figure 3.9.B shows the HEY cells post-incubation with the MNPs and after the third PBS washing. The fluorescence is positive confirmation that the MNPs were either bound to the cell surface or were endocytosed. Figure 3.9.C shows the HEY cells under bright field, post-incubation and after the third PBS washing. There is no visible rolling up of the cells in this image.

No extensive cytotoxicity testing was performed in the drug delivery study and the mechanism has yet to be tested in an animal model. The data obtained from the tests that were performed support a potential novel release mechanism that is both selective and functional at a physiological pH. All the preliminary tests that were conducted involved conjugating packages directly to the MNP using a dichalcogenide link. This approach is only feasible when the package being attached contains a conjugation point that will not affect its function. It was envisioned that the utility of the technique could be greatly expanded if the package to be conjugated was a

| | | |
|---|---|---|
| 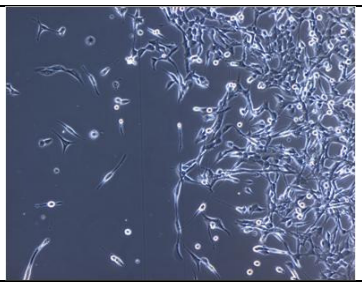 | 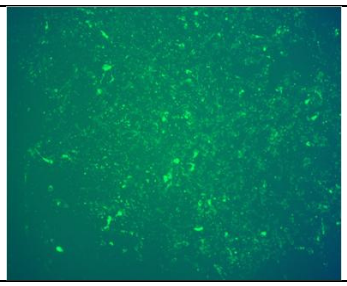 | 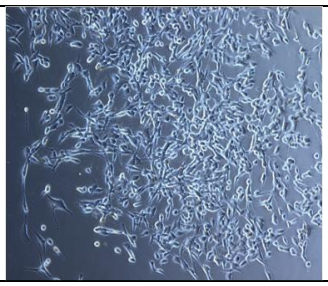 |
| A: HEY cells prior to incubation with magnetic nanoparticles with Se-Te dichalcogenide bonds to peptides (bright field, 10x objective). . | B: Dark field image (460-488 nm band-pass excitation filter, 10x objective) of HEY cells after incubation with nanoparticles with Se-Te dichalcogenide bonds to peptides. Fluorescence is positive indication that particles have adsorbed to the cell membrane or have been endocytosed. | C: HEY cells after incubation with nanoparticles with Se-Te dichalcogenide bond to peptides (bright field, 10x objective). No “rounding up” was observed. |

Figure 3.9A-C: Nanoparticles conjugated to FTIC were incubated with a cancer cell line and analyzed for signs of toxicity.

liposome that could be loaded with a therapeutic molecule. In this case the molecule would not need to be structurally altered. However, this approach has yet to be tested.

# CHAPTER 4

# TARGETING AND CAPTURING OVARIAN CANCER CELLS

(THIS CHAPTER WAS ADAPTED FROM THE ORIGINAL JOURNAL OF THE AMERICAN CHEMICAL SOCIETY PUBLICATION.)[42]

Magnetic cobalt spinel ferrite nanoparticles coated with biocompatible polygalacturonic acid were functionalized with ligands specific for targeting expressed EphA2 receptors on ovarian cancer cells. By using such magnetic nanoparticle-peptide conjugates, targeting and extraction of malignant cells was achieved with a magnetic field. Targeting ovarian cancer cells with receptor specific peptide-modified magnetic nanoparticles resulted in cell capture from a flow stream in vitro and from the peritoneal cavity of mice in vivo. Successful removal of metastatic cancer cells from the abdominal cavity and circulation using magnetic nanoparticle conjugates indicates the feasibility of a dialysis-like treatment and may improve long-term survival rates of ovarian cancer patients. This approach can be applied for fighting other cancers, such as leukemia, once the receptors on malignant cells are identified, and the efficacy of targeting ligands is established.

## Introduction

Magnetic nanoparticles have promising potentials in biomedical applications because of the unique abilities of magnetic interactions over space and physical barriers.[1, 2] Over the past several years, they have shown very promising applications as in vitro medical diagnostic tools. In these studies, magnetic magnetite, $Fe_3O_4$ nanoparticles were used for ultrasensitive detection of prostate-specific antigen (PSA) and for detecting amyloid-β-derived diffusible ligands (ADDLs), which is a potential

Alzheimer's disease (AD) marker.[6, 8] $Fe_3O_4$ nanoparticles also have been employed in the in vitro detection of certain leukemia and lymphoma cells.[7, 9]

We have been exploring possible in vivo approaches aimed at deterrence of the metastatic spread of cancer cells from primary carcinomas. The lethality of cancer is often not due to tumorigenesis at the primary locus but due to metastasis of the disease. To this end, we developed biologically modified magnetic nanoparticles as part of a therapeutic approach to capture and extract cancer cells from the body. For cell capture, using nanoparticles with stronger magnetic properties than $Fe_3O_4$ would be required. Cobalt spinel ferrite, $CoFe_2O_4$ nanoparticles belong to the same spinel ferrite materials family as magnetite. However, they have displayed much stronger magnetic responses at ambient temperatures.[13, 43] We chose ovarian cancer as a model to develop our extraction technique. Ovarian cancer is one of the most lethal gynecological malignancies. The survival rate for patients with late stage disease is about 20%. Because of the difficulty in early diagnosis of ovarian cancer, 81% of all cases are detected in late stages with metastatic spread of malignant cells.[44] The most significant pathway of ovarian tumor spread occurs via exfoliation of malignant cells from primary tumor sites, leading to dissemination of cancer cells throughout the peritoneal cavity[45] and worsening the prognoses for cancer patients.[46, 47] In addition, some cancer cells may escape during primary tumor excision, and the development of resistance in these cells to current chemotherapies can lead to regrowth of a tumor cell population. Intraoperative rupture of malignant epithelial ovarian neoplasms also has been shown to worsen the prognosis of patients with early stage ovarian cancer.[48] Thus, combining the extraction of residual tumor cells to limit the metastatic spread as part of routine treatment procedures could be a strategy to improve long-term survival for cancer patients.

We report here our study on capture of cancer cells from a flow stream in vitro and from the peritoneal cavity of mice in vivo using magnetic $CoFe_2O_4$ nanoparticles functionalized with a receptor-specific ligand. A polypeptide with a sequence of GGGGYSAYPDSVPMMSK was used as a targeting ligand for ovarian cancer cells. The core of the peptide, YSAYPDSVPMMS (YSA), was reported as an ephrin mimetic peptide that binds specifically to EphA2, a receptor tyrosine kinase (RTK), using the YPDSVP residues of the peptide sequence.[49] Because EphA2 is more highly expressed by ovarian carcinoma cells when compared with normal ovarian surface epithelium,[50, 51] magnetic nanoparticle−YSA peptide conjugates should be able to selectively bind to the ovarian cancer cells and enable them for magnetic attraction.

**Experimental Section**

Preparation of CoFe2O4 Nanoparticles with a Biocompatible Polymer Coating and with YSA Peptide Conjugation.

The superparamagnetic CoFe2O4 nanoparticles were synthesized with a micelle method, and the mean diameter was 8 nm with a size distribution of less than 15%. The detailed experimental procedures have been reported elsewhere.[13] The nanoparticles (200 mg) and polygalacturonic acid (600 mg, Alfa Aesar) were added into 80 mL of 5 M NaOH solution at ambient temperature. After sonication for 5 h with a Model 60 Sonic Dismembrator (Fisher Scientific), the coated nanoparticles were separated from the solution using a magnet. After being washed a few times with water, the coated nanoparticles were resuspended in distilled water. Glucuronic acid was also tested as the biocompatible coating with similar procedures. 1.9 mg of peptide having a sequence of GGGGYSAYPDSVPMMSK were added to 10 mL of an aqueous suspension of the

nanoparticles with polygalacturonic acid coating (~1.7 × 1015 particles/mL). The mixture was sonicated for a few minutes. The solution was protected from light and stored at 4 °C overnight to complete the formation of amide bonds between carboxyl groups on the polymer coating and the primary amine on the C-terminal lysine residue.

The YSA peptide was synthesized using standard Fmoc chemistry as reported in the literature.[52] A Rhodamine tag was conjugated on the N-terminus, and the four N-terminal glycine residues were used to distance the Rhodamine from the binding region and prevent steric hindrance to receptor binding.

Cell Growth.

The BG-1 cell line was provided by Julie M. Hall and Kenneth S. Korach of the Environmental Disease and Medicine Program, Research Triangle Park, NC. The BG-1 cells were cultured in DMEM:F12/50:50 (Invitrogen) supplemented with 10% heat-inactivated fetal bovine serum (FBS) (Invitrogen), 100 U/mL penicillin, and 100 µg/mL streptomycin (Mediatech, Inc., Herndon, VA) at 37 °C, in a 5% $CO_2$ atmosphere. The Hey cell line was provided by Gordon Mills, Department of Molecular Therapeutics, The University of Texas, MD Anderson Cancer Center. The Hey cells were propagated in RPMI 1640 (Mediatech) supplemented with 2 mM of L-glutamine (Sigma), penicillin, streptomycin, and 10% heat-inactivated FBS at 37 °C, in a 5% $CO_2$ atmosphere.

Cell Staining.

Cells were incubated overnight with 20 mg/mL of fluorescein diacetate (FDA) (Research Organics) or 20 mg/mL 5(6)-carboxyeosin diacetate (Research Organics) at 37

°C, 5% $CO_2$. Cells were removed from the cell culture flask with trypsin+EDTA, washed once with PBS, and resuspended to $2.8 \times 10^6$ cells/mL. For confocal imaging, cells were incubated overnight on chamber slides (Laboratory Tek) and washed the next day with PBS. Rhodamine labeled nanoparticles with or without conjugated YSA peptide were added to the cells and incubated for 1 h at 37 °C, in a 5% $CO_2$ atmosphere. Cells were washed followed by fixation in 4% paraformaldehyde and coverslipped for imaging analysis.

Mouse Studies.

Female nu/nu mice were obtained from Taconic (Hudson, NY) and Balb/c mice were from Harlan (Indianapolis, IN). All experiments were conducted with the approval of the Institutional Animal Care and Use Committee at the Georgia Institute of Technology (Atlanta, GA).

Microscopy.

In vitro studies were conducted using a 40× objective on an Olympus IX71 inverted microscope with green and red filters and a mercury short arc HBO lamp. Images and video were taken using an Olympus DP71 12.5 million pixel digital camera. Confocal images were obtained with a 40× objective using a Zeiss LSM 510 laser scanning confocal microscope.

**Results and Discussion**

The magnetic $CoFe_2O_4$ nanoparticles were coated with biocompatible polygalacturonic acid to diminish the adverse immune response[18] and also to facilitate the surface modification. After coating of the polymer, the particles became irregular in shape and with a dimension in the range 100−200 nm. Glucuronic acid also worked very well as a biocompatible coating, which formed a shell around each nanoparticle with a thickness of 5−10 nm.

Hey and BG-1 ovarian carcinoma cell lines were used in our studies. While both Hey and BG-1 lines showed expression of EphA2, the expression was several fold higher in the Hey cell line (Figure 4.1.A). For testing the cell targeting and magnetic attraction

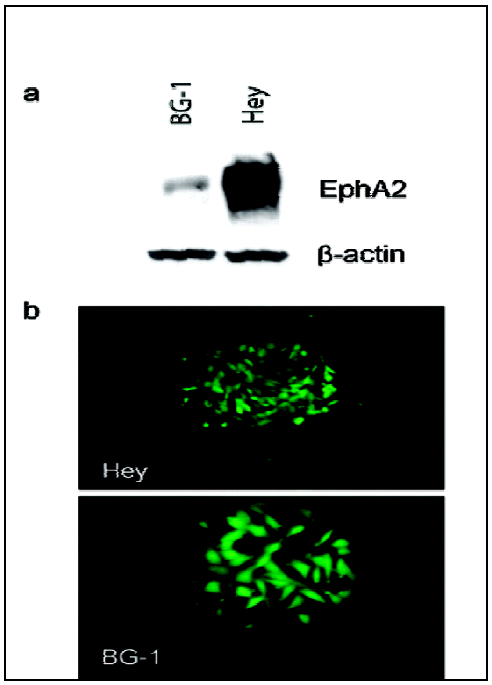


Figure 4.1: Expression of EphA2 receptor in the Hey and BG-1 cell lines. (a) Immunoblot demonstrating the low expression of EphA2 by the BG-1 cell line and the high expression of the receptor in the Hey cell line. β-Actin was used to show equal loading of the samples. (b) Equivalent uptake of the fluorescein fluorophore by the Hey cells and the BG-1 cells.

in vitro, these cancer cell lines were incubated with fluorescein diacetate (FDA) (Figure 4.1.B) with the green emission at 515 nm, which can be distinguished from the nanoparticulate conjugates with the Rhodamine tag emitting red at 610 nm. The labeled Hey cells were introduced into a circulating system driven by a peristaltic pump to determine if EphA2 expressing cells could be extracted from a flow stream. A capillary tube, with a flow rate of ~1.22 mL/min inside, was centered in the circuit and placed above a microscope objective. The continual flow of the green fluorescent Hey cells was observed through the tube. Approximately 2 min after the introduction of Rhodamine-tagged magnetic nanoparticle−YSA peptide conjugates, a magnet, with a field strength of ~2600 gauss, was placed on one side of the capillary tube, and the Hey cells accumulated on the tube wall closest to the magnet. When the magnet was removed, the accumulated Hey cell aggregates dispersed rapidly back into the circulating stream. The cells did not show any response to the magnet if the same magnetic nanoparticles were used but without the YSA peptide ligand. The capture of the cancer cells by the magnet demonstrated the peptide-functionalized nanoparticles caused the cells to become magnetically attractable. Therefore, it may be feasible to effectively remove disseminated cancer cells from the circulation or peritoneal cavity using a dialysis-based approach.

The specific binding of the YSA-conjugated magnetic nanoparticles to Hey cells was verified by using confocal microscopy studies. Hey cells were incubated in chamber slides and allowed to adhere to the slides overnight. The next day, cells were washed and incubated with Rhodamine-tagged magnetic nanoparticles or with the conjugates of

the Rhodamine-tagged magnetic nanoparticle and YSA peptide. Cells were then fixed, and the binding of the magnetic nanoparticles to the cells was examined under fluorescence. Cells incubated with Rhodamine-tagged nanoparticles showed little or no binding to the particles (Figure 4.2.A) while cells incubated with Rhodamine-tagged nanoparticle−YSA peptide conjugates showed binding of the particles over a large amount of the cell surface area (Figure 4.2.B). A higher magnification of one of the Hey cells with Rhodamine-tagged nanoparticle−YSA peptide conjugates is shown in Figure 4.2.C. This result indicates that the magnetic nanoparticles bind specifically to the Hey cells through the YSA peptide/EphA2 interaction and that nonspecific binding of non-YSA-tagged particles approached background levels.

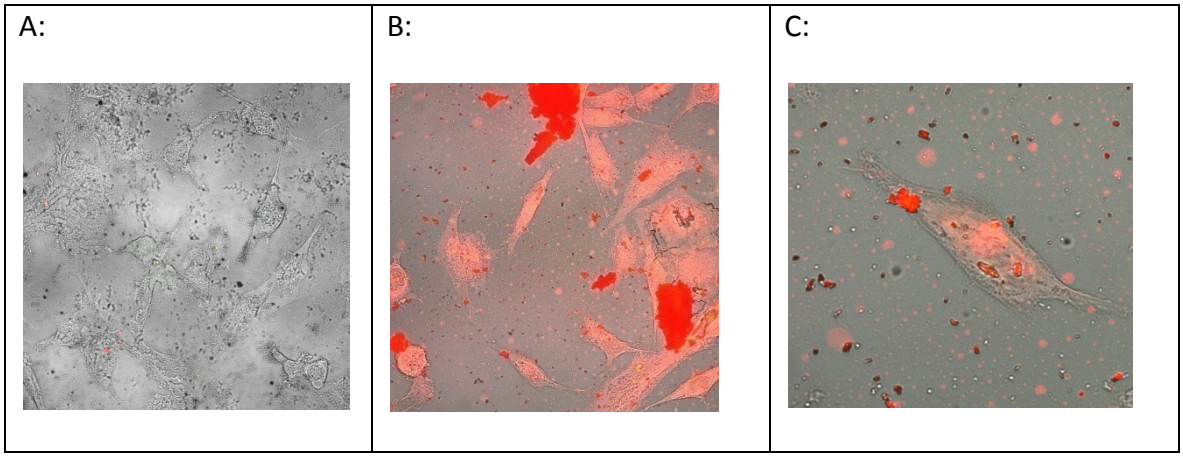


Figure 4.2. Confocal microscopic images (bright field and fluorescent overlays) of *in vitro* targeting of Hey cells. (a) Hey cells incubated with Rhodamine-tagged magnetic nanoparticles with no peptide conjugate (200X). (b) Hey cells incubated with Rhodamine-tagged nanoparticle−YSA peptide conjugates (200×). (c) Higher magnification of Hey cells labeled with Rhodamine-tagged nanoparticle−YSA peptide conjugates (400×).

For testing cell capture in vivo, approximately $1.4 \times 10^6$ FDA-loaded Hey cells in 500 µL of PBS were introduced by injection into the peritoneum of an anesthetized female nu/nu mouse and allowed to disperse for 5 min with gentle abdominal massage to facilitate cell diffusion. The abdomens of the mice were exposed to 488 nm light under a stereo microscope, and there was no visible fluorescent signal at or around the injection site. This was followed by the injection of 500 µL of Rhodamine-tagged magnetic nanoparticle−YSA peptide conjugates. After an additional 5 min of incubation with abdominal massage, the abdomens of the mice were examined under the microscope and no visible fluorescent signal was observed. After a 2600 gauss magnet with a size of ~1 $cm^3$ was placed on the skin of the abdomen for 30 s and then removed, the mouse was exposed to 488 nm light again (Figure 4.3.A). A green emission from the FDA-loaded Hey cells was clearly visible through the skin at the site of magnet placement (Figure 4.3.A and 4.3.B), which indicated a large accumulation of Hey cells at this site. When the excitation wavelength was switched to 530 nm to excite the Rhodamine tag, a red emission was visible through the skin at the same spot indicating the existence of Rhodamine-tagged nanoparticulate conjugates (Figure 4.3.C), which was consistent with the presence of the dark mass under the bright field (Figure 4.3.D). When the magnet was moved over the region and then pulled about 1 cm away from the original aggregation site, the green and red fluorescent spots shifted to the new location. The lack of any visible fluorescent signal prior to applying a magnet onto the mice suggested the dispersion of cells and nanoconjugates. The results obtained with a magnet applied indicate that the Hey cells were captured by the magnetic

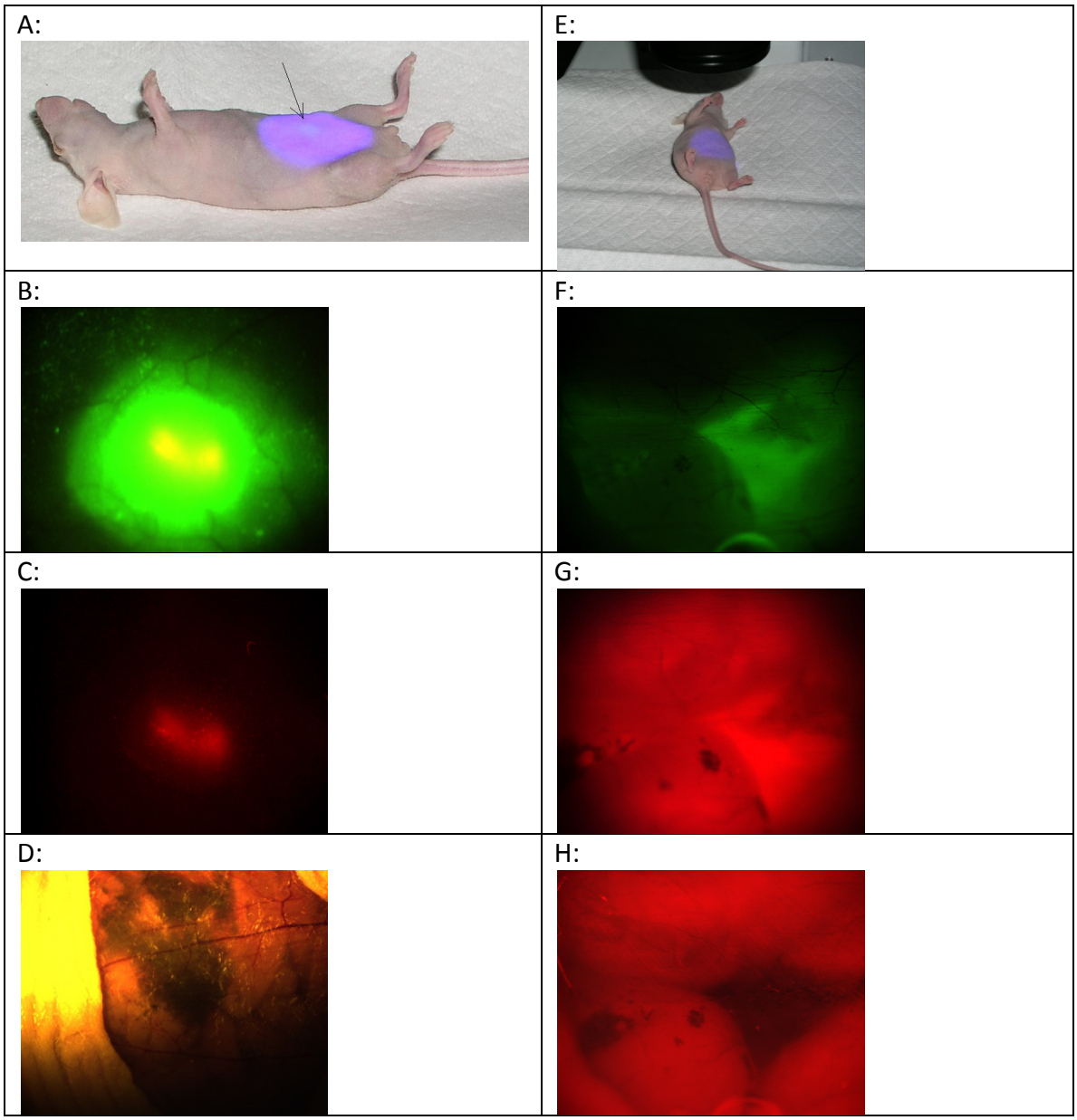


Figure 4.3: In vivo peritoneal targeting of Hey and BG-1 cells with magnetic nanoparticle−YSA peptide conjugates. (a) Green fluorescence of FDA-loaded Hey cells in the center of illumination through the abdominal skin of an anesthetized mouse. The cells were pulled to the cavity surface by the magnet via the nanoparticulate conjugates. (b) Close view of the FDA-loaded Hey cells emitting green through the skin at the site of the magnet. (c) The nanoparticulate conjugates emitting red through the skin at the site of the Hey cells shown in image b. (d) Magnetic nanoparticle−YSA peptide conjugates observed through the peritoneum under a bright field at the site of the magnet. (e) No visible fluorescence of FDA-loaded BG-1 cells through the abdominal skin of an anesthetized mouse under the illumination after the magnet was removed. (f) Close view of the green fluorescing BG-1 cells after the abdominal skin was removed. (g) The nanoparticulate conjugates emitting red at the site of the BG-1 cells shown in image f. (h) Magnetic nanoparticle−YSA peptide conjugates observed under a bright field at the site of the BG-1 cells. Images were taken using a Canon C5050Z digital camera on an Olympus SZX12 stereo microscope with green and red filters, a mercury short arc HBO lamp, and using a 1.6× objective.

nanoparticulate conjugates in the peritoneal cavity of the mouse via YSA peptide/EphA2 recognition and then were consolidated onto the topside of the cavity by the magnet.

The same study was conducted on FDA-loaded BG-1 ovarian cells. Although the fluorescence of BG-1 cells in vitro was as intense as that of the Hey cells, no visible fluorescent emission through the skin was observed upon exposure of the abdomen of the mouse to the 488 nm excitation light (Figure 4.3.E). Fluorescence was visible through the peritoneum once the outer abdominal skin was removed (Figure 4.3.F). The emission was much weaker compared to the one produced by the same number of Hey cells. Intense red fluorescence was clearly seen when the excitation wavelength was switched to the 530 nm range (Figure 4.3.G), and the nanoparticles were easily seen under a bright field (Figure 4.3.H). This indicated that the lack of BG-1 cell aggregates was not due to a shortage of Rhodamine-tagged magnetic particle conjugates. Thus, the low intensity of the fluorescent emissions from the BG-1 cells could be attributed to a smaller number of cells being sequestered by the nanoparticulate conjugates because of relatively low EphA2 receptor expression by the BG-1 cell line. A total of four trials were run for each cell line producing similar results.

The difference in extraction efficiencies of the Hey and BG-1 cells implies the specificity of YSA peptide, which was confirmed by in vivo experiments on magnetic extraction of a mixed population of Hey and BG-1 cells within the peritoneal cavity. The Hey cells were incubated with FDA, and the BG-1 cells were incubated with 5(6)-Carboxyeosin diacetate (CDA) with a 560 nm emission. An equal number of cells from each cell line was mixed and introduced into the peritoneal cavity of three Balb/c female

mice. After 5 min of cell incubation and abdominal massage, magnetic nanoparticulate conjugates were injected into the peritoneal cavity and incubated for 5 min. The peritoneal fluid was extracted and filtered magnetically before being examined using a hemocytometer to determine the number of green fluorescent (Hey) and red fluorescent (BG-1) cells. Although the initially mixed cell populations contained 50% Hey and 50% BG-1 cells, Hey cells accounted for 95−100% of extracted cell populations on average from the three trials (Figure 4.4). The scarcity of BG-1 cells in extracted cell populations was consistent with the specificity of YSA peptide−magnetic nanoconjugates. The highly specific binding of the YSA peptide to the EphA2 receptor enabled the magnetic conjugates to differentiate EphA2-rich ovarian carcinoma cells from EphA2-poor cells.

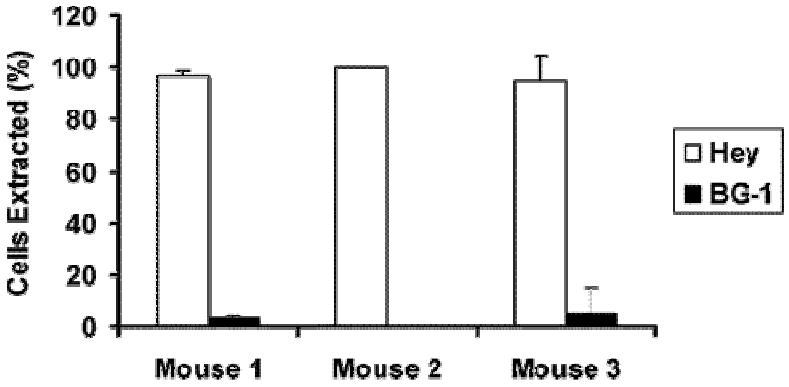


Figure 4.4: Extraction efficiencies of the Hey and BG-1 cells. Compositions of Hey and BG-1 cells in the cell populations extracted from the peritoneum of three Balb/C female mice. The ratios were averaged from five counts performed on each of three mice. Error bars show the standard deviations.

Our initial findings demonstrate that magnetic nanoparticle−YSA peptide conjugates can target and remove metastatic cancer cells from the fluid of the abdominal cavity or circulatory system. Such results suggest the feasibility of a dialysis-like system for the extraction of cancer cells, which, combined with surgery and chemotherapy, may improve the long-term survival rates for cancer patients. In ovarian cancer cases, significant removal of disseminated cancer cells from the abdominal cavity could lead to reduction of the malignant cell population and reduce the odds of metastatic spread. Additional studies, including evaluation of toxic effects from magnetic nanoparticles, are needed before this method can advance to clinic trial stage. Further improvement of this concept may include refinement of the extraction process with an array of peptides using patient specific tumor protein expression profiles. Since small peptides have been reported to prevent tumor cell adherence onto tissues in a murine model using a bladder tumor cell line,[53] they might also be incorporated into the magnetic cell extraction technique to reduce the possibility of tumor implants and therefore greatly enhance the efficiency of preventing metastatic spread of cancer. Since EphA2 is also highly expressed in other types of cancers, applications of the YSA peptide−magnetic nanoconjugates could be expanded beyond ovarian cancers. Furthermore, this in vivo extraction approach utilizing magnetic nanoparticles may also be used in principle for the treatment of viral diseases by targeting and removing viruses and virus-infected cells and therefore bolster the immune system to fight infections.

**Next Steps**

The work described in this study has been expanded to include additional studies. The Ascites Study is a study to determine whether magnetic nanoparticles conjugated to YSA peptides can capture human ovarian cancer cell lines resident in ascites fluid collected from ovarian cancer patients. The Ovarian Cancer Survival Study is a study testing the efficacy of the technology at improving longevity using a metastatic ovarian cancer mouse model. Both studies are discussed in detail in Chapters 5 and 6 respectively.

# CHAPTER 5

# ISOLATION OF OVARIAN CANCER CELLS FROM THE PERITONEAL (ASCITES) FLUID OF OVARIAN CANCER PATIENTS USING SUPERPARAMAGNETIC COBALT SPINEL FERRITE NANOPARTICLES WITH PEPTIDE CONJUGATES

Serous effusions from patients with late stage (III, IV) ovarian carcinoma contain adenocarcinoma cells with metastatic potential. Selective removal of these cells from serous fluids could abate metastases and increase 5 year survival rates. We have previously demonstrated that superparamagnetic nanoparticles conjugated to a mimetic peptide with high affinity for EphA2, a receptor expressed on the surface of ovarian cancer cells, can be used to harvest these cells from the abdomen of experimental mice. In this study, we demonstrate that these nanoparticles can be used to successfully isolate free floating ovarian cancer cells from peritoneal (ascites) fluid collected from human ovarian cancer patients. Our results demonstrate the potential - clinical significance of our methodology in the treatment of ovarian cancer.

## Introduction

Carcinoma of the ovaries frequently results in the accumulation of fluids in the peritoneal and pleural cavities. [54] Lymphatic obstruction and over-production of peritoneal fluids by the epithelial cells of the peritoneal cavity are responsible for the bulk of the fluid accumulation.[55, 56] The constituents of these effusions include malignant cells exfoliated from the primary tumor as well as dendritic and other

immunological cell types. Previous studies have shown that the presence of immune cells in the peritoneal cavity of ovarian cancer patients is seldom sufficient to prevent the expansion of carcinomas. Cancer cells generate factors[57, 58] that prevent the requisite maturation required for dendritic cells to present tumor antigens and mount an effectual anti-tumor response.[59, 60] For this reason, alternative strategies are required to help abate the metastatic potential of free floating cancer cells in the peritoneal fluid of ovarian cancer patients.

The lethality of ovarian cancer is partially credited to its being relatively asymptomatic in the early stages and its rapid metastatic spread intraperitoneally. The presence of malignant cells in accumulated ascites is often indicative of a poor prognosis for the majority of patients.[61, 62] The dangers associated with leaving the malignant cells unabated are almost unquestionably mortal. Unhindered malignant cells with metastatic potential can establish tumor sites at foci distant to the primary tumor locus and result in an untreatable expansion of the disease. The 5-year survival rates of patients with stage III, and IV ovarian carcinomas are typically as low as 30% and 18% respectively.[63]

Immunochemical methods have been extensively applied to selectively identify carcinomas in peritoneal effusions. Various studies have identified antigens with high expression profiles in malignant ovarian cancer cells. The antibody to the human epithelial antigen (HEA), Ber-EP4 [64, 65] , the extracellular domain of the MUC16 cell surface protein, CA125 [66-69], and a receptor tyrosine kinase (RTK), EphA2 [70], have been determined to be highly selective markers for free floating ovarian cancer cells. These

markers are currently being leveraged by various targeted modalities to avoid the collateral damage associated with the less discriminate radiation and chemo therapies.[71, 72] Our previous studies have indicated the potential viability of reducing metastatic implantation and increasing 5-year survival rates of ovarian cancer patients by reducing the titer of malignant cells in peritoneal or other serous effusions.[42] We have previously shown that a peptide mimetic of ephrin with high affinity for the EphA2 receptor can be conjugated to superparamagnetic nanoparticles for targeted extraction of ovarian cancer cells from the peritonea of experimental mice. We demonstrate here the potential clinical significance of this methodology by in vitro isolation of ovarian cancer cells from human ascites fluids.

**Materials and Methods**

Nanoparticle Synthesis.

The superparamagnetic $CoFe_2O_4$ nanoparticles were synthesized with a microemulsion technique and the mean diameter was 8 nm with a size distribution of less than 15%. The detailed experimental procedures have been reported elsewhere.[13]

Nanoparticle Coating and Peptide Conjugation.

600 mg of $CoFe_2O_4$ nanoparticles were added to 300 mL of 5M NaOH and sonicated for 10 min (Fisher Dismembrator 60 – power setting of 19). 1800 mg of glucuronic acid was added to the solution and sonication continued for 1.5 hours. The product was magnetically separated using a 5000 gauss magnet, washed 3x in PBS and

resuspended in 600 mL of distilled $H_2O$ bringing the nanoparticle concentration to approximately 1 mg/mL. Particles used in control studies were taken from this stock solution. To add peptide conjugates, the nanoparticles coated with glucuronic acid were magnetically filtered from 300 mL of the stock solution and resuspended in 30 mL of 0.2 M sodium bicarbonate, pH 9.6. 3 mL from a solution of 0.088 M sodium periodate was added and allowed to react in the dark for 20 minutes. The nanoparticles were again magnetically filtered from solution using a 5000 gauss magnet and resuspended in 30 mL of 0.2 M sodium bicarbonate, pH 9.6. 60 mg of the N-terminally Rhodamine-conjugated peptide GGGGYSAYPDSVPMMSK (2127.9 g/mol) was dissolved in 6 mL of 0.2 M sodium bicarbonate, pH 9.6, and then pooled with the 30 mL nanoparticle solution. The reaction was allowed to proceed on a platform shaker at room temperature and in reduced light for two hours. 360 µL of sodium cyanoborohydride (5 M) was added to the solution in a fume hood and the reaction proceeded for an additional 30 minutes under the same conditions. 1.8 mL of 2-aminoethanol was then added to cap unreacted aldehydes and the reaction proceeded for an additional 30 minutes. The final product was magnetically separated from the solution using a 5000 gauss magnet and washed 10x with 0.1 M sodium phosphate buffer and then resuspended in 300 mL of distilled $H_2O$. The average diameter of the nanoparticle (approximately 8 nm), the density of the particle (5.29 g/mL), and the mass of the peptide (2127.9 Da) were used to calculate an approximate peptide to particle ratio of nearly 81:1, assuming total reactant consumption.

Peptide Synthesis.

The GGGGYSAYPDSVPMMSK peptide was synthesized using standard Fmoc chemistry.[52] A Rhodamine tag was conjugated on the N-terminus, and the four N-terminal glycine residues were used to distance the Rhodamine from the binding region and prevent steric hindrance of EphA2 receptor binding.

Ascites Fluid Preparation.

Ascites samples were obtained from the Ovarian Cancer Institute of Atlanta, Georgia. Collection methods have been well documented.[73] Ascites samples were stored at -80$^{o}$ C in 10% DMSO and thawed in a 37$^{o}$C water bath in preparation for use.

Cell Extraction.

For each sample being tested five 12 x 75 mm round-bottom tubes were labeled as follows: Tube 1 – pure ascites, Tube 2 – filtrand, Tube 3 – filtrate, Tube 4 – filtrand control, Tube 5 – filtrate control. 500 µL of ascites fluid was added to Tube 1, 2 and 4. 700 µL of ice cold PBS (10% FBS, 1% sodium azide) was added to Tube 1 and it was stored on ice for analysis. 200 µL of peptide conjugated magnetic nanoparticles (1 mg/mL) and 500 µL of ice cold PBS (10% FBS, 1% sodium azide) were added to Tube 2. Tube 2 was vortexed for 15 seconds and shaken for 10 minutes by hand. Tube 2 was then attached to a 5000 gauss magnet for 10 minutes. With the magnet attached to the tube, the fluid was pipetted from Tube 2, placed in Tube 3, and Tube 3 was stored on ice for analysis. The captured magnetic nanoparticles were washed in sterile PBS 3x and

resuspended in 300 µL of same. The 300 µL nanoparticle solution was filtered through the cap of a 12 x 75 mm round-bottom tube, the volume was raised to 1200 µL using sterile PBS, and Tube 2 was stored on ice for analysis. 200 µL of magnetic nanoparticles having no peptide conjugate (1 mg/mL) and 500 µL of ice cold PBS (10% FBS, 1% sodium azide) were added to Tube 4. Tube 4 was vortexed 15 seconds, shaken for 10 minutes by hand, and then attached to a 5000 gauss magnet for 10 minutes. While attached to the magnet, the fluid was pipetted from Tube 4, placed in Tube 5, and Tube 5 was stored on ice for analysis. The captured magnetic nanoparticles were washed in sterile PBS 3x and resuspended in 300 µL of same. The 300 µL nanoparticle solution was filtered through the cap of a 12 x 75 mm round-bottom tube, the volume was raised to 1200 µL using sterile PBS, and Tube 4 was stored on ice for analysis. Tubes 1-5 were analyzed immediately using a BD LSR flow cytometer (BD Biosciences).

Cell Surface Staining.

300 µL of ascites fluid was resuspended in 12 x 75 mm round-bottom tubes containing 500 µL of ice cold PBS (10% FBS, 1% sodium azide). All manipulations involving fluorophore-conjugated antibodies were performed in the dark. The samples were centrifuged at 800 RPM and 4$^{o}$ C for 5 minutes and the supernatant volume was reduced to the 300 µL mark at the base of the tube. 100 µL of ice cold PBS (10% FBS, 1% sodium azide) was added to the sample and the tube was gently agitated to re-suspend the cells. 10 µL of the primary antibody was added and the sample was left to incubate on ice for 30 min. 500 µL of ice cold PBS (10% FBS, 1% sodium azide) was added to each

sample and the samples were centrifuged at 800 RPM and 4$^{o}$ C for 5 minutes. DIRECT STAINING –The previous washing step was performed 3 times and the cells were resuspended in 1200 µL of ice cold PBS (10% FBS, 1% sodium azide) and analyzed immediately using a BD LSR flow cytometer (BD Biosciences). INDIRECT STAINING –The washing step was performed 3 times and the cells were resuspended in 100 µL of ice cold PBS (10% FBS, 1% sodium azide). 10 µL of the secondary antibody was added and the sample was left to incubate on ice for 30 min. 500 µL of ice cold PBS (10% FBS, 1% sodium azide) was added to each sample and the samples were centrifuged at 800 RPM and 4$^{o}$ C for 5 minutes. This washing step was performed 3 times and the cells were resuspended in 1200 µL of ice cold PBS (10% FBS, 1% sodium azide) and analyzed immediately using a BD LSR flow cytometer (BD Biosciences).

Flow Cytometry.

For each sample analysis using the BD LSR flow cytometer (BD Biosciences) the software configurations (BD Facs/Diva, BD Biosciences) remained consistent. Forward (FSC) and side scatter (SSC) patterns were recorded with a four decade log amplifier. The threshold was set to 2000 and the voltages for the FSC, SSC, FITC, and PE-A parameters were set to 505, 236, 500, and 401 respectively. For each trial 10,000 events were recorded. Gating of populations was established for a particular patient sample and copied to successive trials to preserve statistical viability.

Flourescence Microscopy.

100 µL of the solutions from each tube used for flow cytometry analysis was added to a falcon tube along with 10 µL of Trypan Blue and a small volume was plated for viewing. A 2500 gauss magnet was used to aggregate the magnetic nanoparticles in the solutions from Tube 2 and the aggregate and fluid were placed on a microscope slide for viewing (Olympus X51 Inverted Flourescence Microscope) and imaging (Olympus DP-71).

**Results**

Flow cytometry has been successfully employed in other studies to differentiate the cell populations resident in peritoneal and pleural effusions.[74] In the described study we employed flow cytometry to analyze pure ascites samples, the filtrand removed from these samples using peptide-conjugated and non-peptide-conjugated superparamagnetic nanoparticles, and the filtrate remaining in the sample after the filtrand was removed. Bivariate analysis was used to establish significant variation between the number of cells extracted using peptide-conjugated nanoparticles and the number extracted using nanoparticles with no peptide conjugate. Immunophenotyping techniques were used to verify whether the cells being extracted resided in populations testing positive for markers associated with ovarian adenocarcinoma cells or antigen presenting cells that might be displaying these markers.

<u>Identifying Extracted Cell Populations.</u>

A baseline of resident cell populations in ascites samples was determined by observing bivariate displays of forward and side scatter patterns produced when the untreated samples were analyzed using a BD LSR flow cytometer (BD Biosciences). Dot plots for 3 separate trials conducted on patient samples 914 and 923 are featured in Figure 5.1.A-C and Figure 5.2.A-C respectively. The distributions in the scattergrams

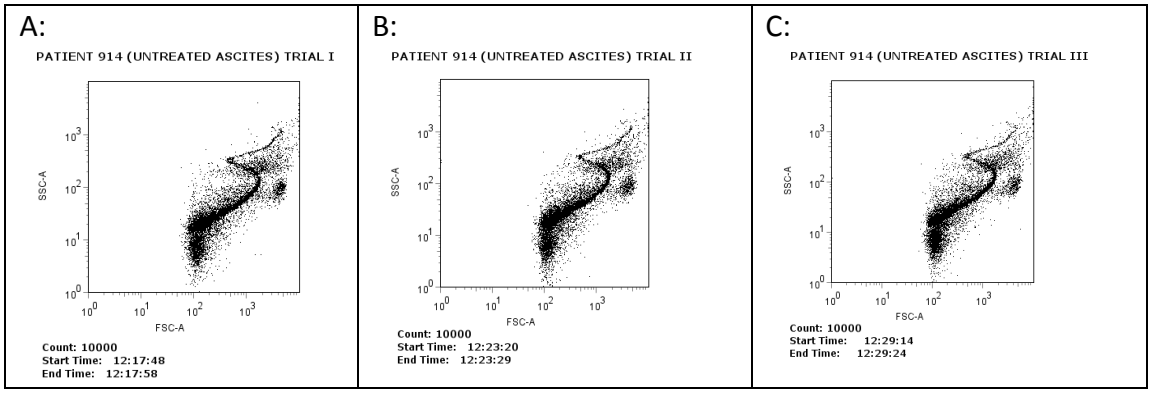


Figure 5.1: Dot plots for flow cytometry analysis (Trials 1-3) of untreated ascites sample from patient 914.

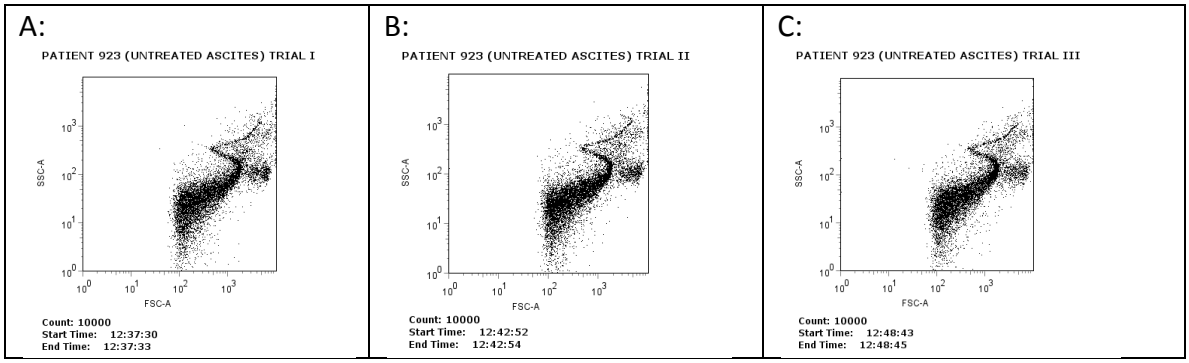


Figure 5.2: Dot plots for flow cytometry analysis (Trials 1-3) of untreated ascites sample from patient 923.

display morphological consistency across each trial. Quantitative confirmation of this consistency was obtained by gating the visually discreet populations on a density plot of the first trial for each patient (Figures 5.3 and 5.4), copying these gates to each

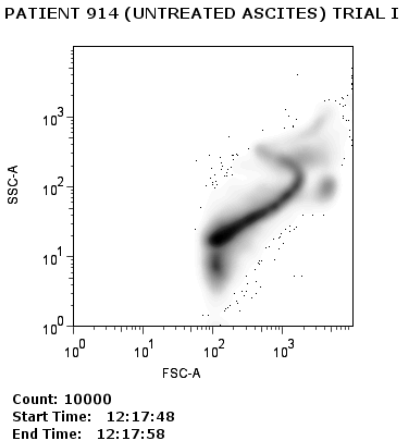


Figure 5.3: Density plot of flow cytometry analysis of ascites sample for patient 914 (Trial 1) used for population gating.

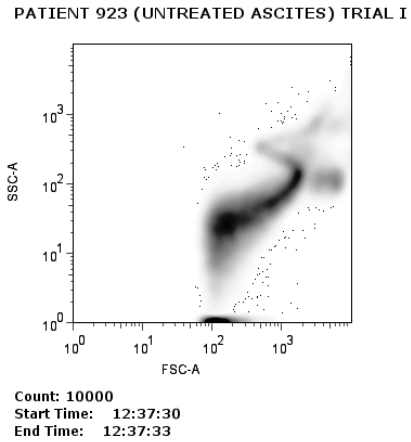


Figure 5.4: Density plot of flow cytometry analysis of ascites sample for patient 923 (Trial 1) used for population gating.

successive trial, and displaying the percent of total recorded events (% Total) for each gated population (Figures 5.5.A-C and 5.6.A-C). The three trial average % Total for each gated population is featured in Tables 5.1 and 5.2 for patients 914 and 923 respectively.

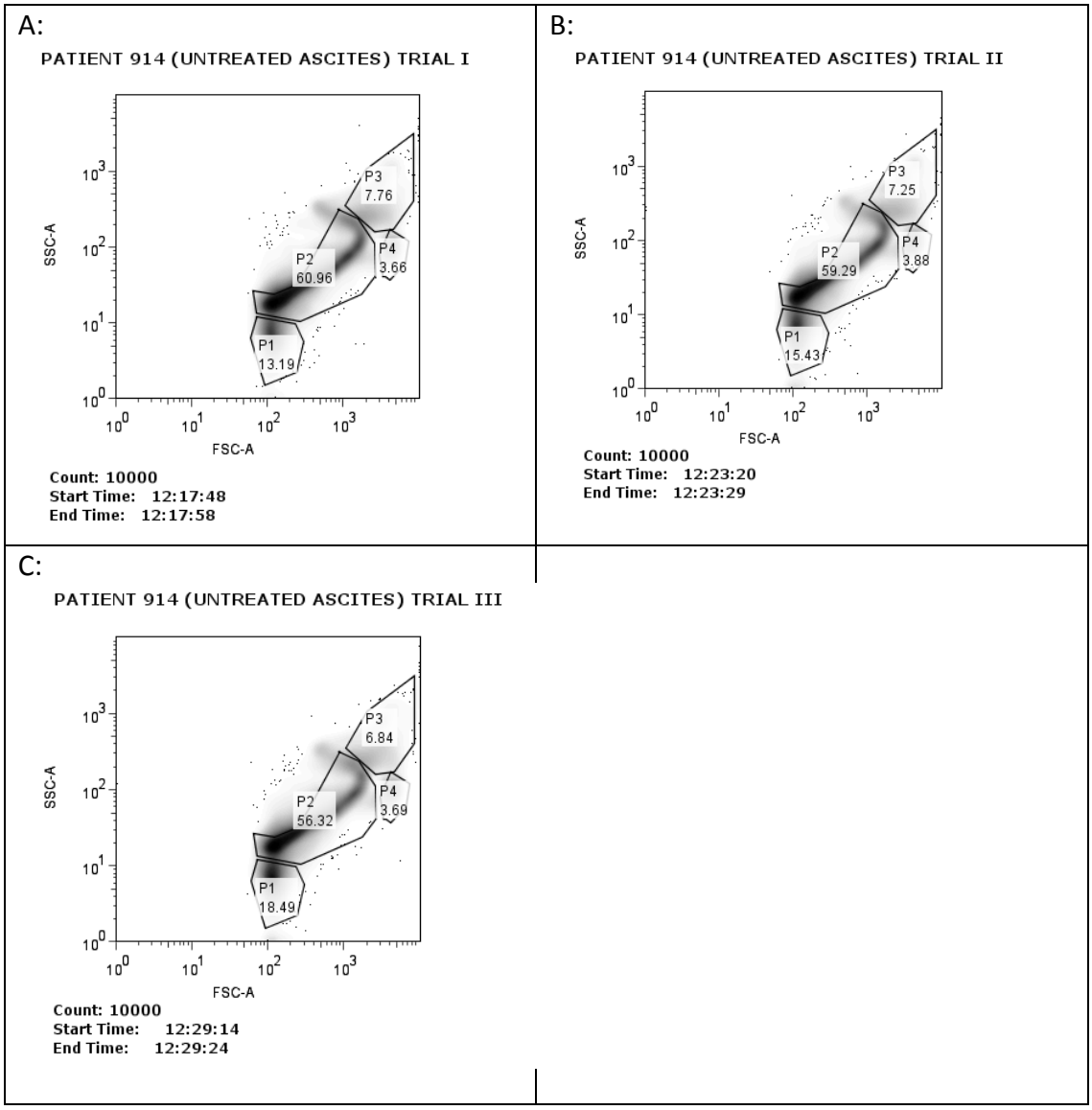


Figure 5.5: Density plot of flow cytometry analysis of ascites samples for patient 914 (Trials 1-3) showing gated populations, frequencies, and population labels (1-4).

Table 5.1: % Total for each population gated on density plots obtained from flow cytometry analysis of the untreated ascites samples of patient 914 (Averaged for Trials 1-3).

| POPULATION | AVERAGE (TRIALS 1-3) | STD DEVIATION (TRIALS 1-3) |
|---|---|---|
| 1 | 15.70 | 2.66 |
| 2 | 58.86 | 2.35 |
| 3 | 7.28 | 0.46 |
| 4 | 3.74 | 0.12 |

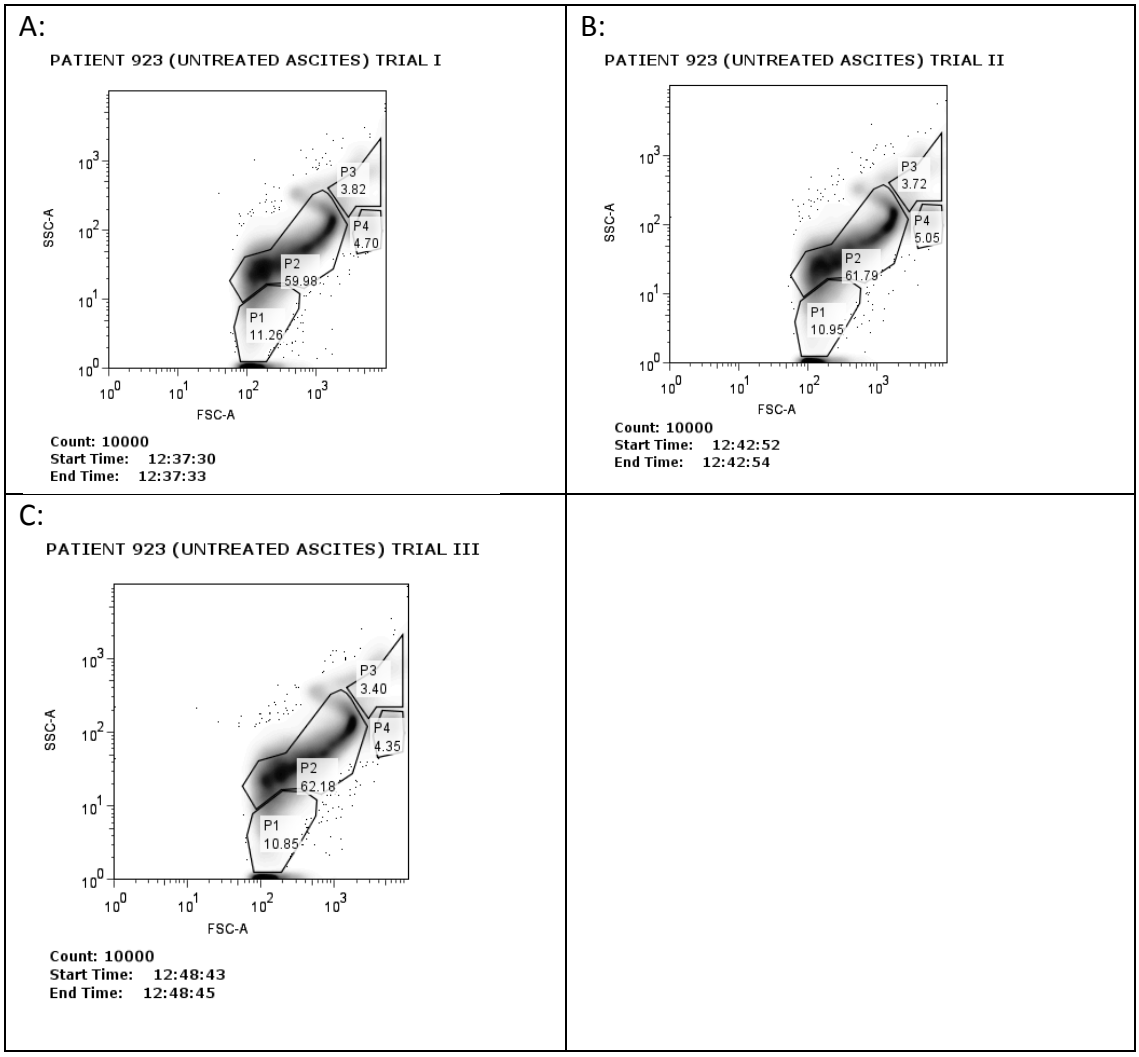


Figure 5.6: Density plot of flow cytometry analysis of ascites samples for patient 923 (Trials 1-3) showing gated populations, frequencies, and population labels (1-4).

Table 5.2: % Total for each population gated on density plots obtained from flow cytometry analysis of the untreated ascites samples of patient 923 (Averaged for Trials 1-3).

| POPULATION | AVERAGE (TRIALS 1-3) | STD DEVIATION (TRIALS 1-3) |
|---|---|---|
| 1 | 11.02 | 0.21 |
| 2 | 61.32 | 1.17 |
| 3 | 3.65 | 0.22 |
| 4 | 4.70 | 0.35 |

Superparamagnetic $CoFe_2O_4$ nanoparticles (200 µL – 1 mg/mL) coated with glucuronic acid and having N-terminally Rhodamine-conjugated 17 residue peptide functions (GGGGYSAYPDSVPMMSK) were added to 1.0 mL peritoneal effusion samples diluted in sterile PBS (dilution factor 1:2) and given 10 minutes to incubate at ambient temperature. The superparamagnetic nanoparticle conjugates (filtrand) were magnetically filtered from the samples during a 10 minute exposure to a 5000 gauss magnet. The filtrand was washed 3x with sterile PBS, resuspended in 300 µL of same, and filtered through a 12 x 75 mm falcon tube cap at 800 RPM ($4^o$ C) for 5 minutes. The volume of the filtrand sample was increased to 1200 µL. The filtrate remaining from the extraction was added to a 12 x 75 mm falcon tube. The filtrand and filtrate were analyzed using the BD LSR flow cytometer (BD Biosciences) (Figures 5.7.A-C, 5.8.A-C, 5.9.A-C, and 5.10.A-C). The morphologies of the dot plots featured in Figures 5.7 and 5.8 are dissimilar to the dot plots in Figures 5.1 and 5.2. The gates from the untreated ascites trial for each patient were superimposed over the dot plots obtained from the filtrand and filtrate samples to determine the % Total delta for each population (Figures 5.11.A-C, 5.12.A-C, 5.13.A-C, and 5.14.A-C). To reduce background interference caused

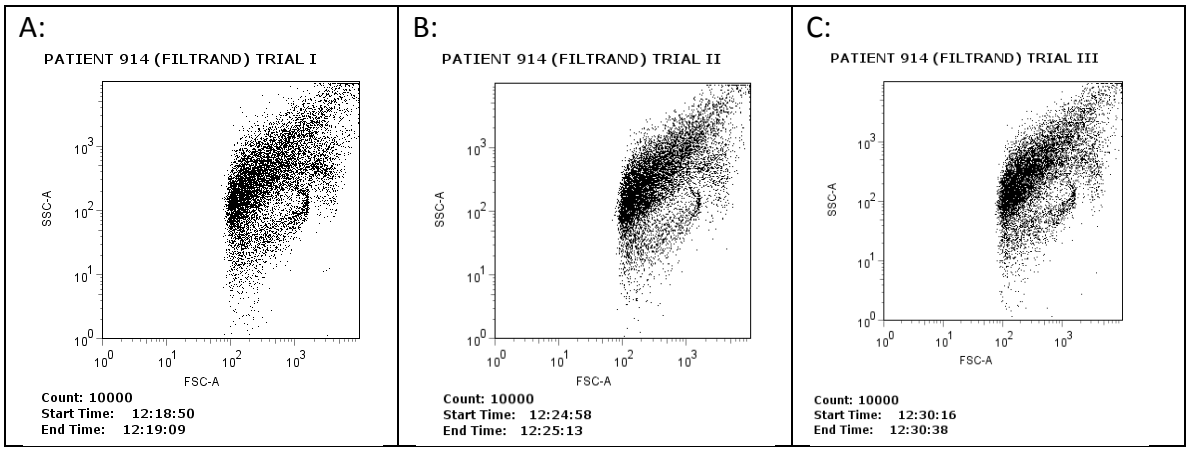


Figure 5.7: Dot plots for flow cytometry analysis (Trials 1-3) of filtrand from patient 914.

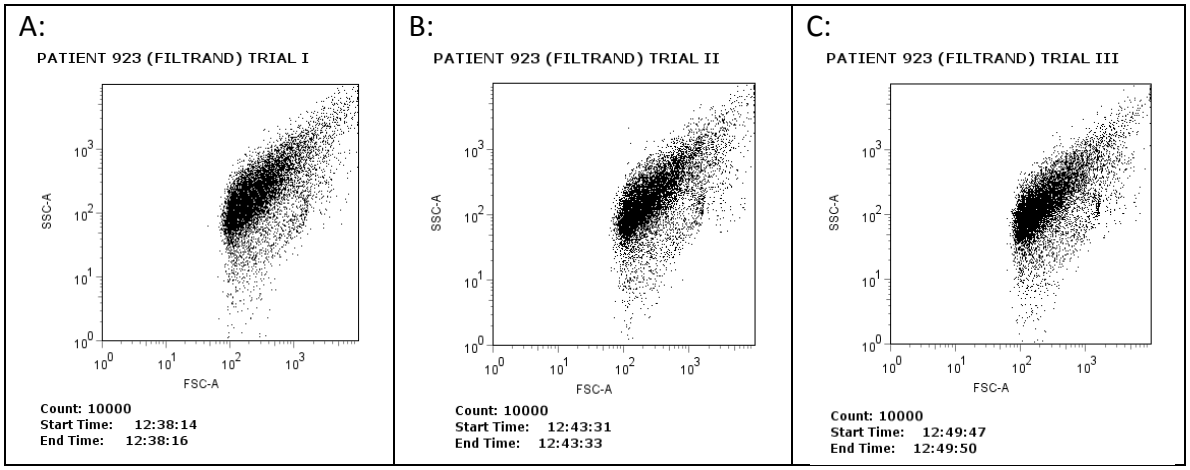


Figure 5.8: Dot plots for flow cytometry analysis (Trials 1-3) of filtrand from patient 923.

by aggregates of the coated magnetic nanoparticles alone, 200 µL of the glucuronic acid-coated nanoparticles with and without peptide conjugates were added to separate 12 x 75 mm Falcon tubes containing 1.0 mL sterile PBS and the samples were analyzed using the BD LSR flow cytometer (BD Biosciences) (Figure 5.15.A-F, Table 5.7). The bivariate plot produced by the nanoparticles was gated and the gates for populations 2 and 3 of the ascites samples were adjusted to minimize overlap with this region. The experiment

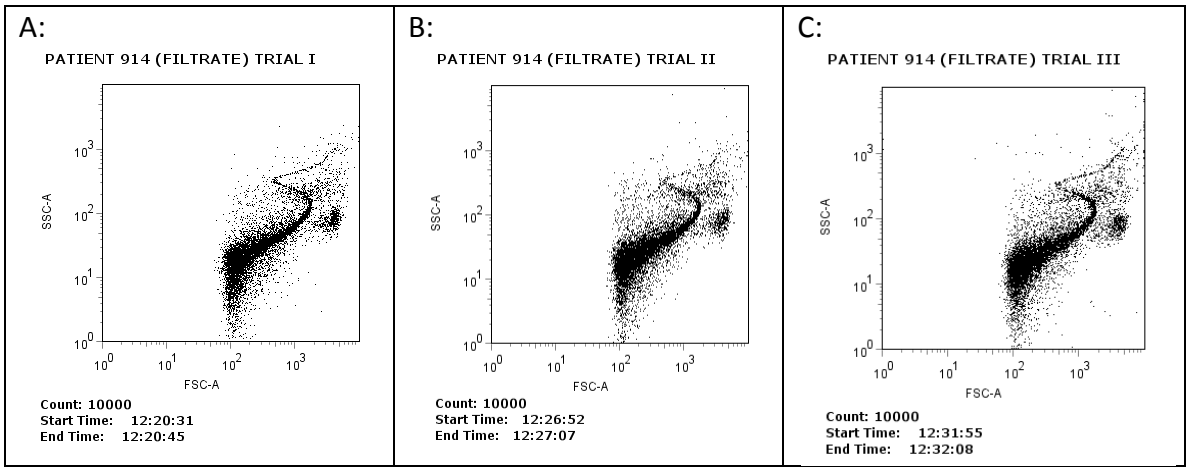


Figure 5.9: Dot plots for flow cytometry analysis (Trials 1-3) of filtrate from patient 914.

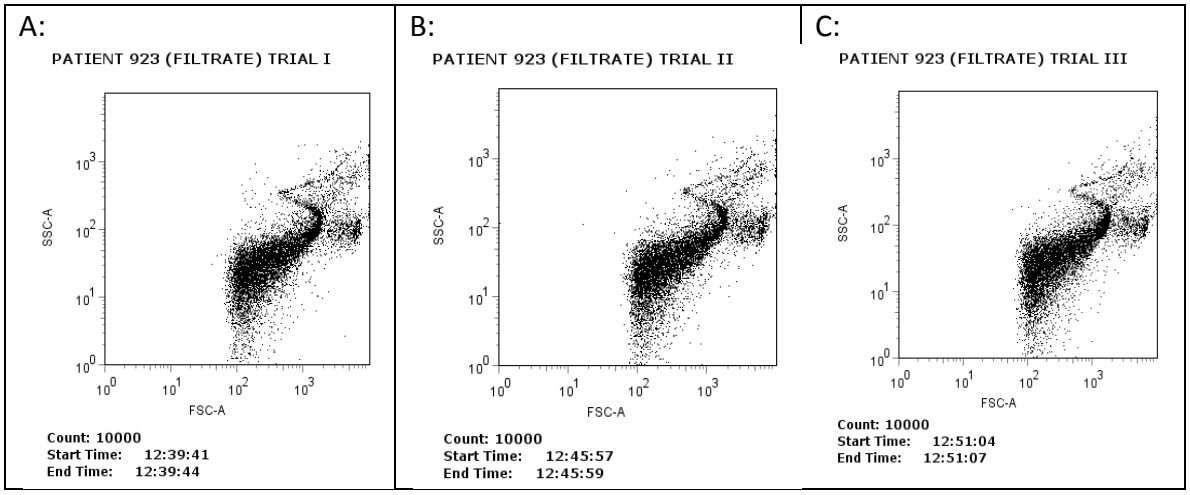


Figure 5.10: Dot plots for flow cytometry analysis (Trials 1-3) of filtrate from patient 923.

was repeated three times on each patient sample and then conducted three more times using glucuronic acid coated superparamagnetic nanoparticles with no peptide conjugates (Figures 5.16.A-C, 5.17.A-C, 5.18.A-C, and 5.19.A-C).

Visual inspection of the plots of FSC versus SSC for each patient's untreated ascites samples yielded at least 4 distinct subpopulations and the regions encompassed

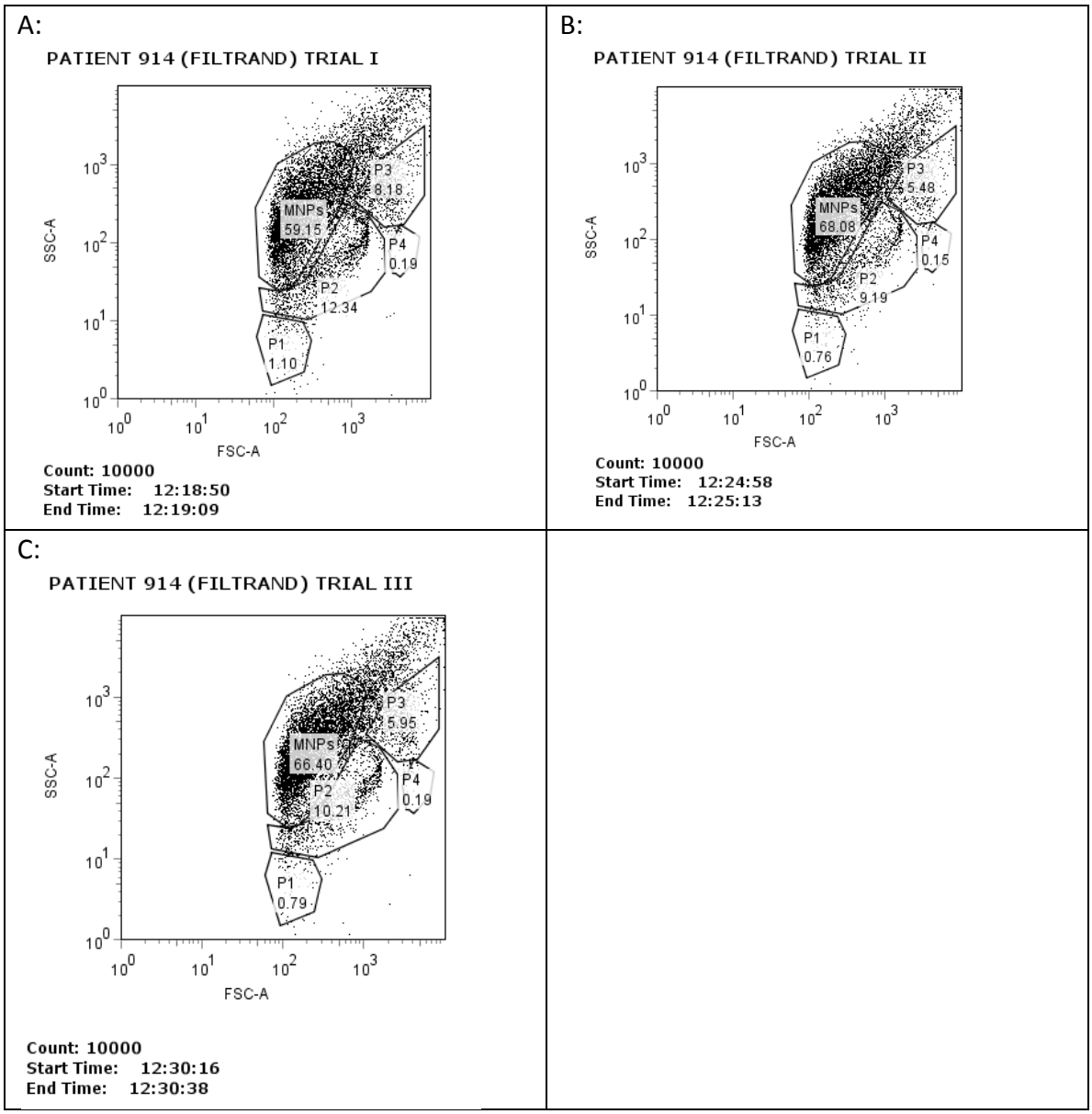


Figure 5.11: Dot plot of flow cytometry analysis of filtrand samples for patient 914 (Trials 1-3) showing gates copied from untreated ascites trial (Trial 1), frequencies, and population labels (1-4).

Table 5.3: % Total for each population gated on dot plots obtained from flow cytometry analysis of the filtrand samples of patient 914 (Averaged for Trials 1-3).

| POPULATION | AVERAGE (TRIALS 1-3) | STD DEVIATION (TRIALS 1-3) |
|---|---|---|
| 1 | 0.88 | 0.19 |
| 2 | 10.58 | 1.61 |
| 3 | 6.54 | 1.44 |
| 4 | 0.18 | 0.02 |

by gates P1 and P2 initially held the largest average number of events (Tables 5.1 and 5.2). The average % Total values for each population from the filtrand and filtrand control trials are featured in Tables 5.3, 5.4, 5.8, and 5.9. An average of 5.60% +/- 1.54% (mean +/- standard deviation), 17.97% +/- 2.81%, 89.84% +/- 20.58%, and 4.81% +/- 0.56% of the cells in the ascites samples from patient 914 were extracted using peptide conjugated nanoparticles from populations P1, P2, P3 and P4 respectively (See Calculation 1) while 0.19% +/- 0.13%, 0.46% +/- 0.19%, 4.53% +/- 0.74 %, and 0.27% +/- 0.27% were extracted using nanoparticles with no peptide conjugates from the same respective gated populations. For patient 923 samples an average of 13.70% +/- 1.0%, 20.92% +/- 2.24%, 32.05% +/- 2.37%, and 2.13% +/- 0.87% of cells were extracted using peptide conjugated nanoparticles and 2.45% +/- 0.64%, 5.02% +/- 0.45%, 6.58% +/- 0.91%, and 0.00% of cells were extracted using nanoparticles with no peptide conjugates from populations P1, P2, P3, and P4 respectively.

**CALCULATION 1**: Sample calculation used to determine the percentage of cells extracted from a gated population. It was determined that an average of 5.60% +/- 1.54% (mean + standard deviation) of the cells was extracted from population P1 of ascites samples taken from patient 914 using the following data:

The average % Total of gate P1 for three untreated ascites samples was 15.70% +/- 2.66%.
The average % Total of gate P1 for three filtrand trials was 0.88% +/- 0.19%.

$y = 0.88 \quad \sigma_y = 0.19$
$t = 15.70 \quad \sigma_t = 2.66$
$g = y/t$ $\quad g = 0.88 / 15.70 = 0.0560$ or 5.60%

**Error propagation:**

$$\sigma_g = \sqrt{\left(\frac{0.88}{(15.7)^2}\right)^2 \cdot (2.66)^2 + \left(\frac{1}{15.7}\right)^2 \cdot (0.19)^2} = 0.0153831190729 = 1.54\%$$

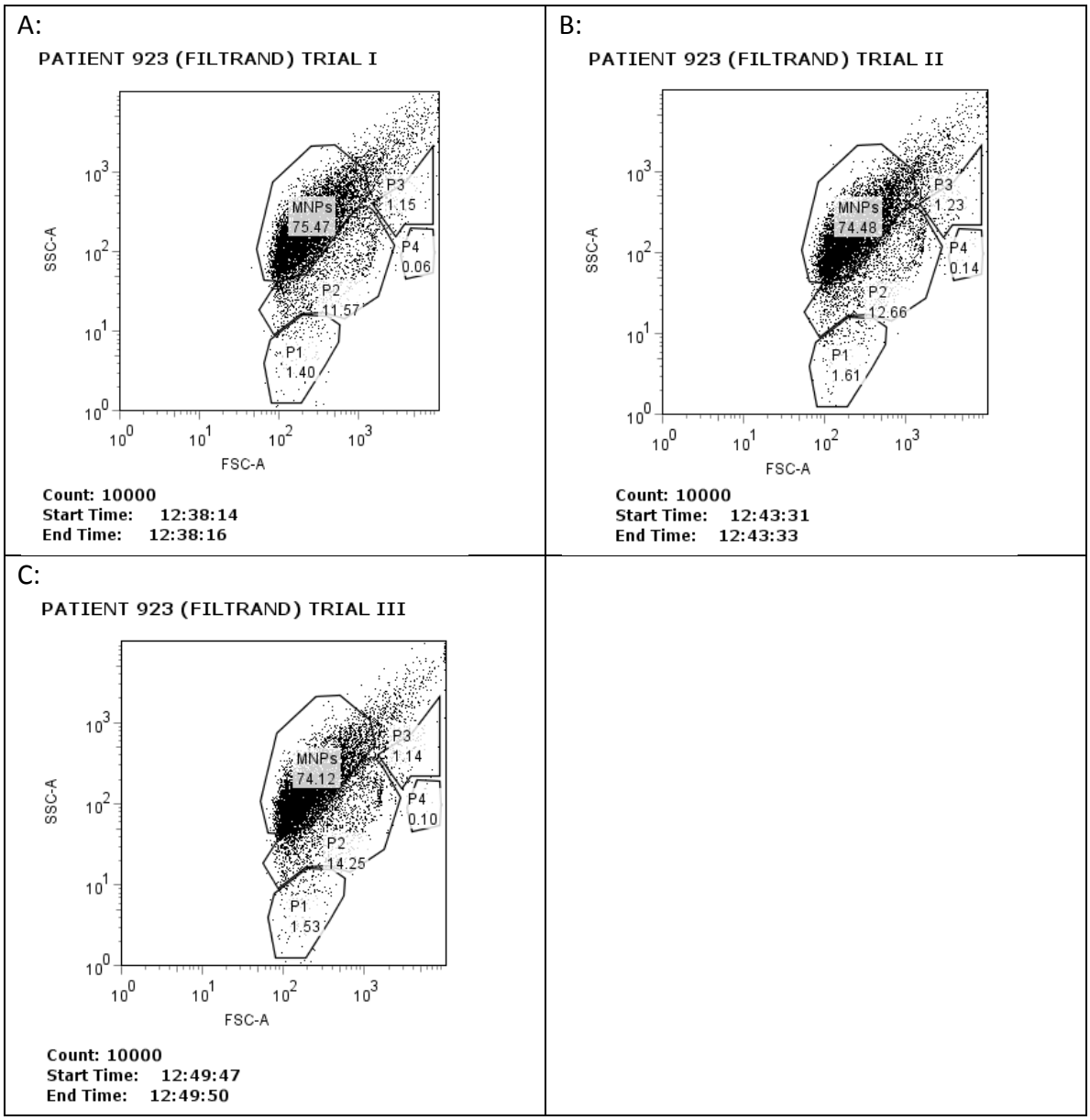


Figure 5.12: Dot plot of flow cytometry analysis of filtrand samples for patient 923 (Trials 1-3) showing gates copied from untreated ascites trial (Trial 1), frequencies, and population labels (1-4).

Table 5.4: % Total for each population gated on dot plots obtained from flow cytometry analysis of the filtrand samples of patient 923 (Averaged for Trials 1-3).

| POPULATION | AVERAGE (TRIALS 1-3) | STD DEVIATION (TRIALS 1-3) |
|---|---|---|
| 1 | 1.51 | 0.11 |
| 2 | 12.83 | 1.35 |
| 3 | 1.17 | 0.05 |
| 4 | 0.10 | 0.04 |

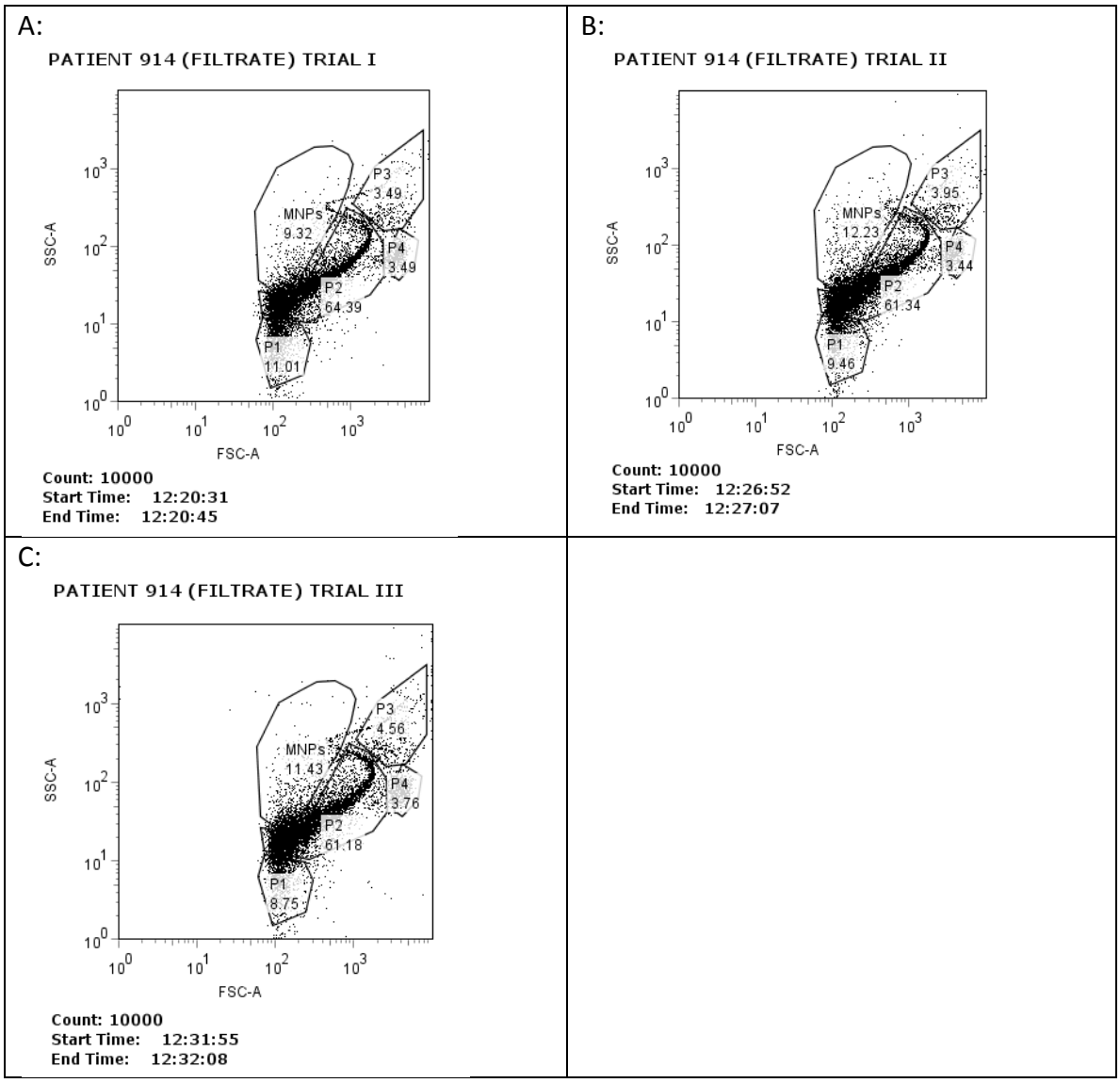


Figure 5.13: Dot plot of flow cytometry analysis of filtrate samples for patient 914 (Trials 1-3) showing gates copied from untreated ascites trial (Trial 1), frequencies, and population labels (1-4).

Table 5.5: % Total for each population gated on dot plots obtained from flow cytometry analysis of the filtrate samples of patient 914 (Averaged for Trials 1-3).

| POPULATION | AVERAGE (TRIALS 1-3) | STD DEVIATION (TRIALS 1-3) |
|---|---|---|
| 1 | 9.74 | 1.16 |
| 2 | 62.30 | 1.81 |
| 3 | 4.00 | 0.54 |
| 4 | 3.56 | 0.17 |

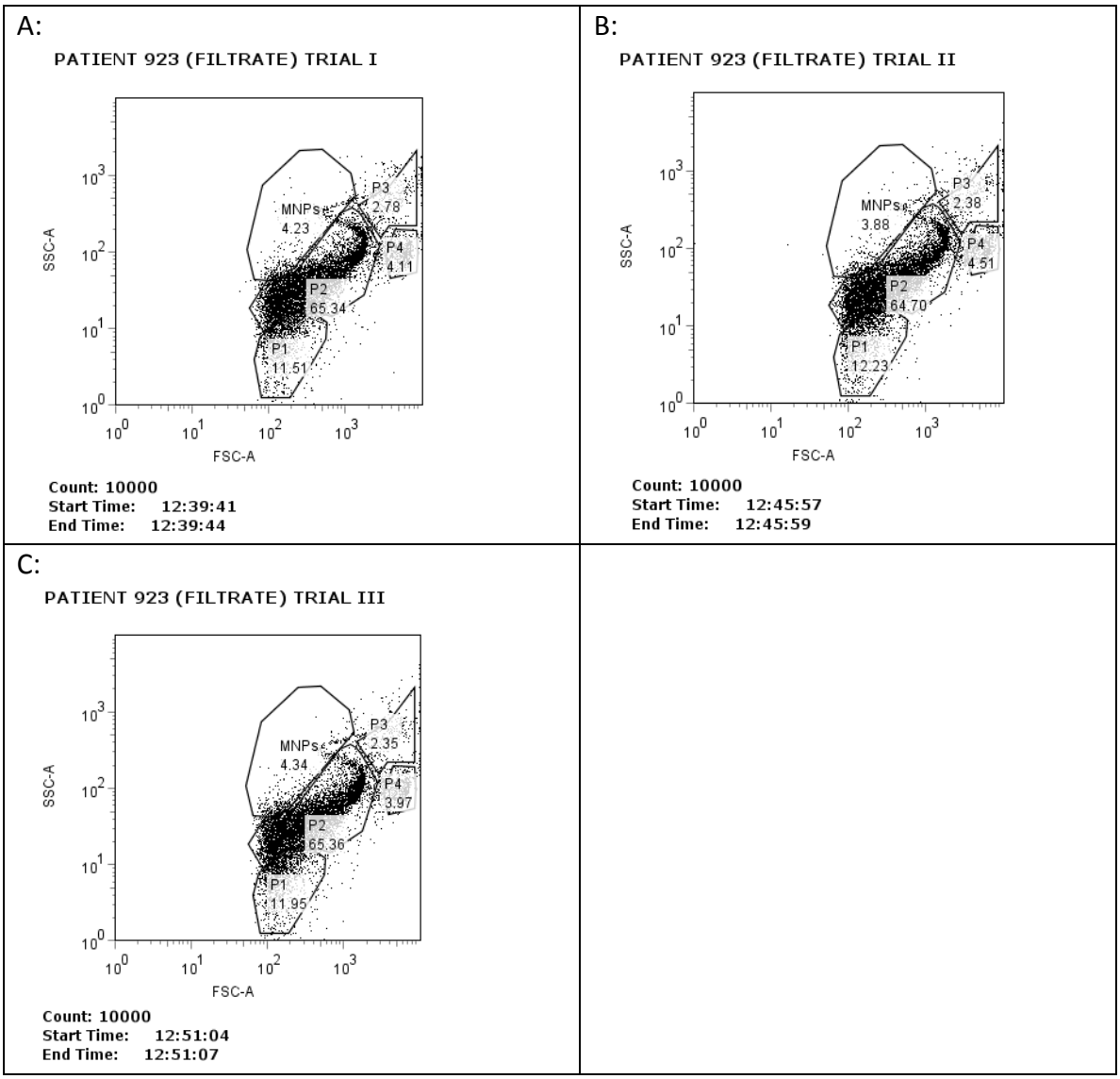


Figure 5.14: Dot plot of flow cytometry analysis of filtrate samples for patient 923 (Trials 1-3) showing gates copied from untreated ascites trial (Trial 1), frequencies, and population labels (1-4).

Table 5.6: % Total for each population gated on dot plots obtained from flow cytometry analysis of the filtrate samples of patient 923 (Averaged for Trials 1-3).

| POPULATION | AVERAGE (TRIALS 1-3) | STD DEVIATION (TRIALS 1-3) |
|---|---|---|
| 1 | 11.90 | 0.36 |
| 2 | 65.13 | 0.38 |
| 3 | 3.24 | 1.16 |
| 4 | 4.20 | 0.28 |

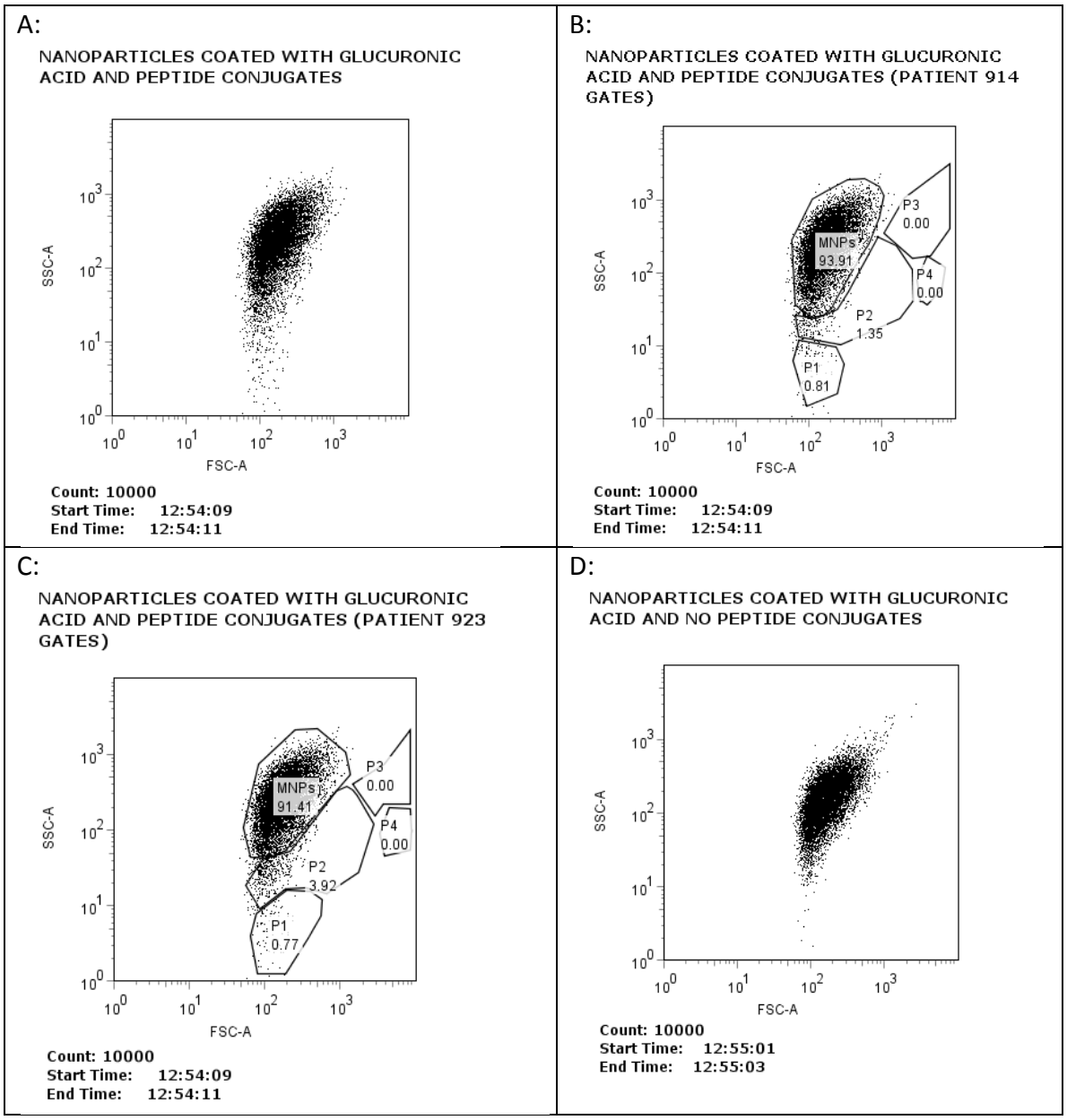


Figure 5.15: A: Dot plot of flow cytometry analysis of superparamagnetic nanoparticles coated with glucuronic acid and peptide functions B-C: Dot plot of flow cytometry analysis of superparamagnetic nanoparticles coated with glucuronic acid and peptide functions showing gates copied from untreated ascites trial (Trial 1) for patient sample 914(5.15.B) and 923(5.15.C). D: Dot plot of flow cytometry analysis of superparamagnetic nanoparticles coated with glucuronic acid and no peptide functions E-F: Dot plot of flow cytometry analysis of superparamagnetic nanoparticles coated with glucuronic acid and no peptide functions showing gates copied from untreated ascites trial (Trial 1) for patient sample 914(5.15.E) and 923(5.15.F).

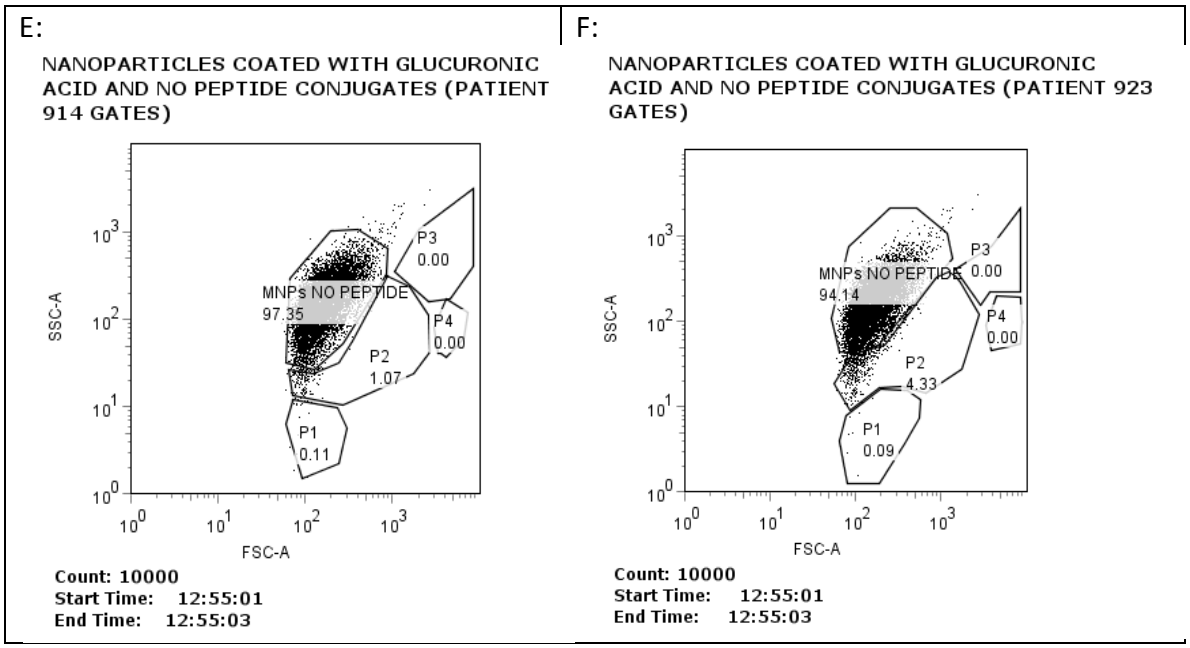


Figure 5.15 continued

Table 5.7: % Total for each population gated on dot plots obtained from flow cytometry analysis of the superparamagnetic nanoparticles coated with glucuronic acid and peptide functions for all three patient samples.

| POPULATION | NANOPARTICLE W/ PEPTIDE % Total PATIENT SAMPLE 914 | NANOPARTICLE W/O PEPTIDE % Total PATIENT SAMPLE 914 | NANOPARTICLE W/ PEPTIDE % Total PATIENT SAMPLE 923 | NANOPARTICLE W/O PEPTIDE % Total PATIENT SAMPLE 923 |
|---|---|---|---|---|
| 1 | 0.81 | 0.11 | 0.77 | 0.09 |
| 2 | 1.35 | 1.07 | 3.92 | 4.33 |
| 3 | 0.00 | 0.00 | 0.00 | 0.00 |
| 4 | 0.00 | 0.00 | 0.00 | 0.00 |

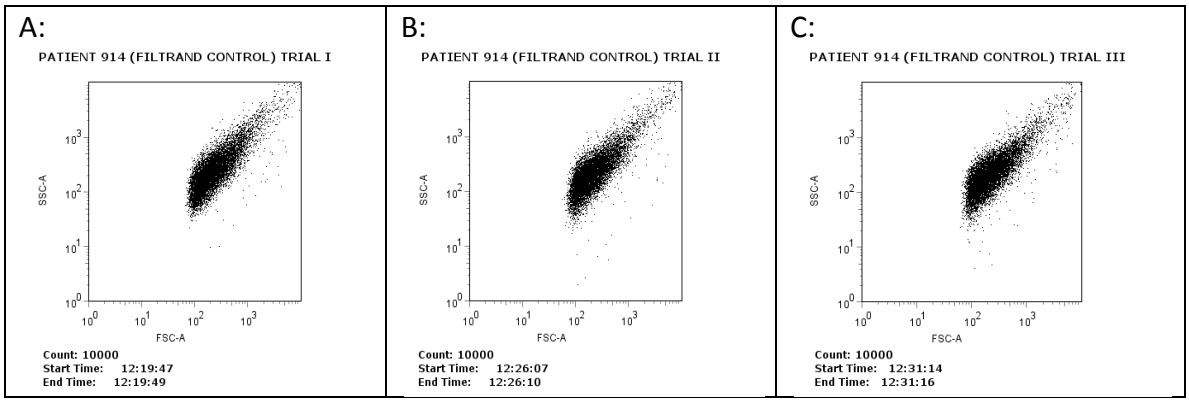


Figure 5.16: Filtrand extracted from patient samples (Patient 914) using nanoparticles having no peptide conjugates.

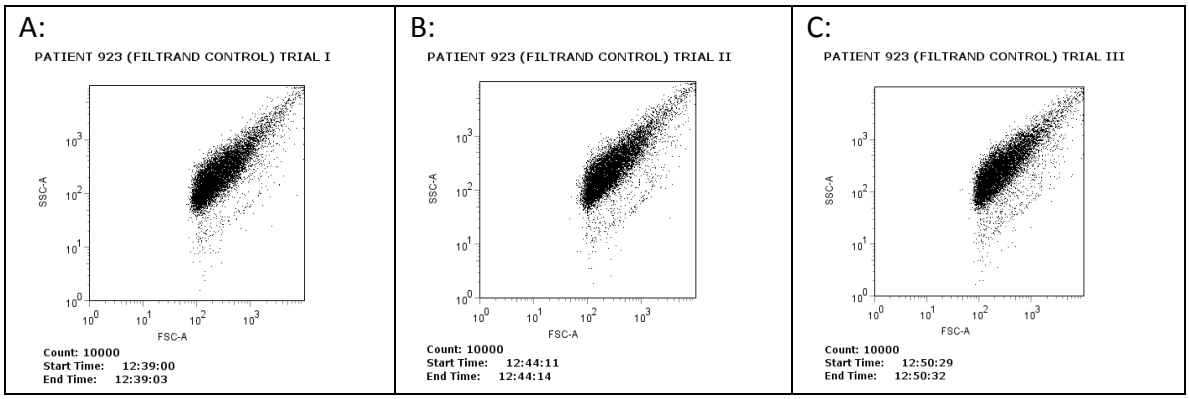


Figure 5.17: Filtrand extracted from patient samples (Patient 923) using nanoparticles having no peptide conjugates.

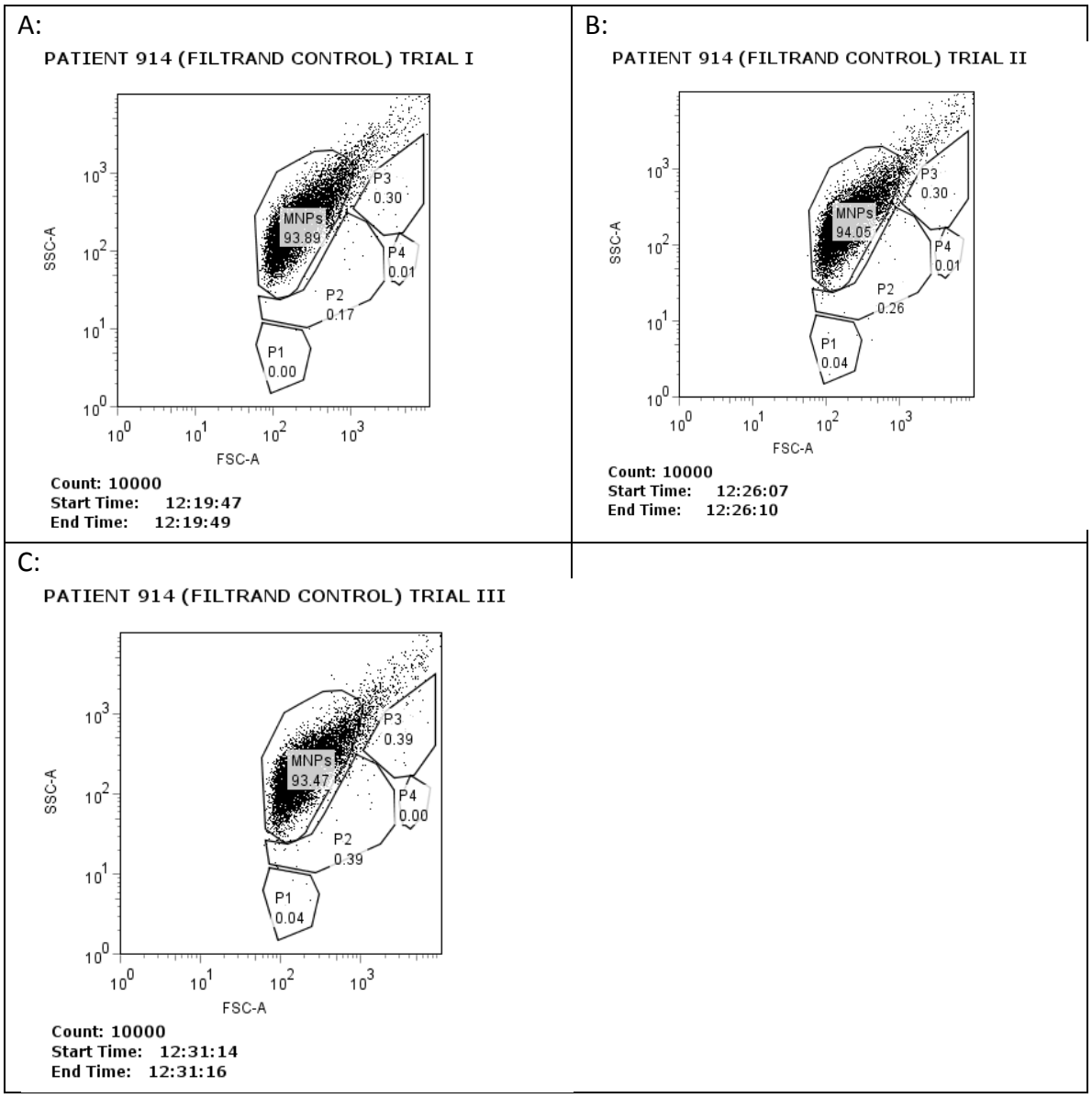


Figure 5.18: Filtrand extracted from patient samples (Patient 914) using nanoparticles having no peptide conjugates. Population gates were copied from previous trials performed on untreated ascites and pure nanoparticle samples.

Table 5.8: % Total for each population gated on dot plots obtained from flow cytometry analysis of the filtrand control samples of patient 914 (Averaged for Trials 1-3).

| POPULATION | AVERAGE (TRIALS 1-3) | STD DEVIATION (TRIALS 1-3) |
|---|---|---|
| 1 | 0.03 | 0.02 |
| 2 | 0.27 | 0.11 |
| 3 | 0.33 | 0.05 |
| 4 | 0.01 | 0.01 |

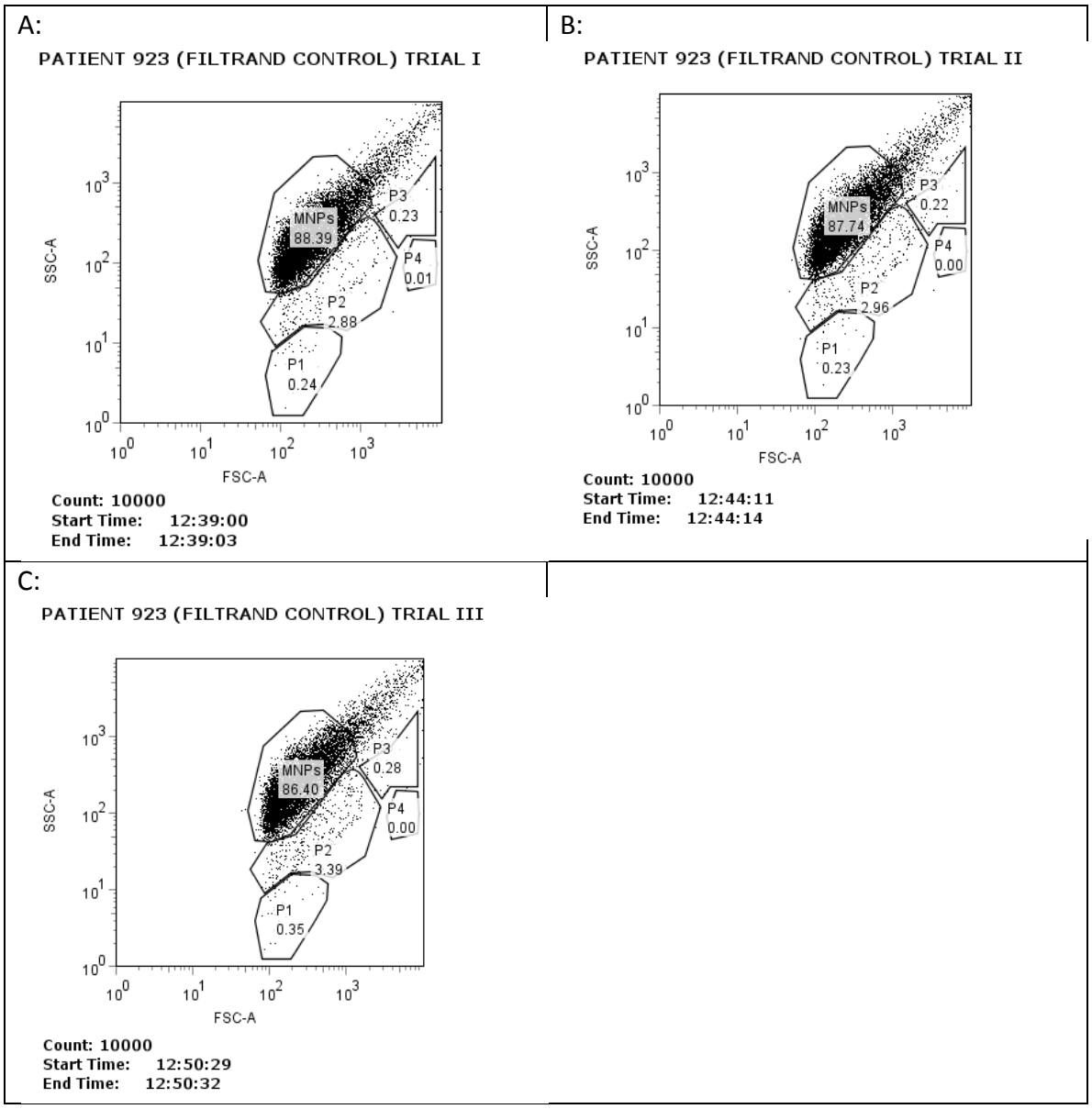


Figure 5.19: Filtrand extracted from patient samples (Patient 923) using nanoparticles having no peptide conjugates. Population gates were copied from previous trials performed on untreated ascites and pure nanoparticle samples.

Table 5.9: % Total for each population gated on dot plots obtained from flow cytometry analysis of the filtrand control samples of patient 923 (Averaged for Trials 1-3).

| POPULATION | AVERAGE (TRIALS 1-3) | STD DEVIATION (TRIALS 1-3) |
|---|---|---|
| 1 | 0.27 | 0.07 |
| 2 | 3.08 | 0.27 |
| 3 | 0.24 | 0.03 |
| 4 | 0.00 | 0.01 |

Demonstrating the Binding of Ovarian Cancer Cells to Peptide Conjugated Nanoparticles.

GGGGYSAYPDSVPMMSK peptide conjugation to nanoparticles using the reductive amination technique described in the Methods section was verified by taking magnetically aggregated particles that had been cleansed in multiple washes with PBS and viewing them using fluorescence microscopy. Figure 5.20 shows an aggregation of magnetic nanoparticles with Rhodamine-conjugated peptides viewed using an Olympus Rhodamine filter on an Olympus X51 inverted fluorescence microscope. The red fluorescence produced by the aggregate was taken as confirmation that the peptides had been successfully linked.

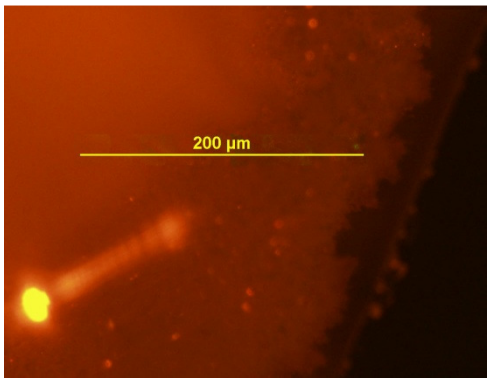


Figure 5.20: Fluorescence microscopy image (20x) of superparamagnetic nanoparticles coated with glucuronic acid and Rhodamine-conjugated peptides taken on an Olympus X51, equipped with an Olympus DP-71 camera, and using an Olympus Rhodamine filter. The particles in this image were aggregated using a 2500 gauss magnet to enhance visibility.

To visually confirm the adsorption of cells to the nanoparticles subsequent to flow cytometry analysis, a 100 µL sample of the filtrand was stained with 10 µL of Trypan Blue and imaged using bright field microscopy (Figure 5.21). Having been

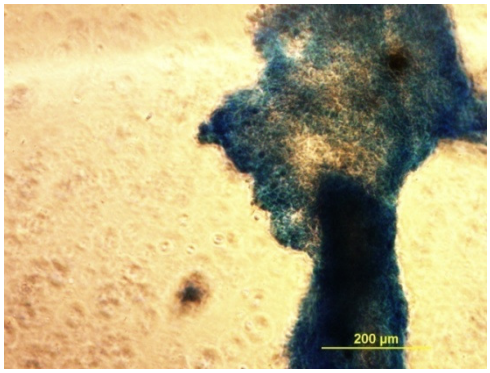


Figure 5.21: Microscope bright field image (10x) of filtrand from ascites sample stained with Trypan Blue. Ascites samples had been previously stored in 10% DMSO at -80$^{o}$C and would contain dead cells that would not prevent Trypan Blue from traversing their membranes. In this image we see the aggregation of dead cells bound to nanoparticles magnetically extracted from the patient samples.

previously stored at -80$^{o}$C, it was assumed that the ascites samples would contain dead cell populations. Dead cells can no longer inhibit the passage of Trypan Blue across the cell membrane and would be enhanced visually under bright field imaging using this technique. A 2500 gauss magnet was used to aggregate the magnetic nanoparticles into large clusters to provide further image enhancement. In Figure 5.21 the nanoparticle aggregate appears blue, suggesting the adherence of dead cells.

<u>Demonstrating that Peptide Conjugated Nanoparticles Can Successfully Extract Ovarian Cancer Cells from Human Ascites Fluid.</u>

Extracted cell counts were compared between experimental and control samples for each patient and trial using Chi-square analysis. The null hypothesis tested was that there was no significant difference between the numbers of cells collected in the experimental and control groups for each gated population. The cell counts from the

filtrand obtained using superparamagnetic nanoparticles coated with glucuronic acid and conjugated to a 17 residue peptide sequence (GGGGYSAYPDSVPMMSK) made up the experimental data set (a) and the cell counts from the filtrand obtained using superparamagnetic nanoparticles coated with glucuronic acid and no peptide conjugates made up the control data set (c). The minimum accepted p value of significance was 0.05. If the p value was greater than 0.05 it was concluded that the conjugated peptide had no significant effect on the cell numbers extracted. For p values lower than 0.05 we determined that cell counts were significantly enhanced using the peptide conjugate. The census of each starting population was taken from the flow cytometry analysis of the pure ascites samples used for each trial ($H_1$ and $H_0$ for experimental and control groups respectively). An example calculation is illustrated in Calculation 1 and the results from the analysis can be seen in Tables 5.10 and 5.11 for patients 914 and 923 respectively. The p values for the majority of the patient trials fell well below 0.05 and it was concluded that the superparamagnetic nanoparticles with the 17 residue peptide conjugate were capable of extracting a significantly higher number of cells than particles with no peptide conjugates. The only trials yielding p values higher than 0.05 came from population 4 of samples analyzed from patient 923. It was determined that any cells extracted from this population were captured non-specifically.

To verify the proclivity of the 17 residue peptide (GGGGYSAYPDSVPMMSK) to target cell populations expressing markers commonly expressed by adenocarcinomas peritoneal effusions were immunostained using a panel of monoclonal antibodies

**CALCULATION 2**: Sample calculation using Chi-square analysis to determine the statistical significance of cell numbers extracted using superparamagnetic nanoparticles conjugated to ephrin mimetic peptides.

| | CAPTURED | NOT CAPTURED | |
|---|---|---|---|
| EXPERIMENTAL | a | b | $H_1$ |
| CONTROL | c | d | $H_0$ |
| | $V_1$ | $V_0$ | t |

Chi square = $\frac{(t)(ad-bc)^2}{(V_1)(V_0)(H_1)(H_0)}$

Data from Trial I of the samples analyzed from Patient 914:

a = 1234 (Cell count from population 1 of the filtrand obtained using nanoparticles with peptide conjugates)
$H_1$ = 6096 (Cell count from population 1 of the untreated ascites sample)
b = $H_1$-a = 4862
c = 17 (Cell count from population 1 of the filtrand obtained using nanoparticles with no peptide conjugates)
$H_0$ = 6096 (Cell count from population 1 of the untreated ascites sample used to test the control)
d = $H_0$-c = 6079
t = $H_1$ + $H_0$ = 12192
$V_1$ = a + c = 1251
$V_0$ = b + d = 10941

Chi square = 1319.30

Because a 2 x 2 chi square table was used the degrees of freedom (df) equaled 1. The Chi square and df values were used to calculate p values.

Table 5.10: Chi-square analysis on filtrand from Patient 914's ascites samples.

| POPULATION | TRIAL | CHI-SQUARE VALUE | P-value | TOTAL CELLS IN EXPERIMENTAL POPULATION | CELLS CAPTURED FROM EXPERIMENTAL POPULATION | TOTAL CELLS IN CONTROL POPULATION | CELLS CAPTURED FROM CONTROL POPULATION |
|---|---|---|---|---|---|---|---|
| 1 | 1 | 114.79 | $8.76 \times 10^{-27}$ | 1319 | 110 | 1319 | 0 |
| 1 | 2 | 66.53 | $3.46 \times 10^{-16}$ | 1543 | 76 | 1543 | 4 |
| 1 | 3 | 69.33 | $8.34 \times 10^{-17}$ | 1849 | 79 | 1849 | 4 |
| 2 | 1 | 1319.30 | $7.25 \times 10^{-289}$ | 6096 | 1234 | 6096 | 17 |
| 2 | 2 | 916.94 | $2.04 \times 10^{-201}$ | 5929 | 919 | 5929 | 26 |
| 2 | 3 | 1004.24 | $2.15 \times 10^{-220}$ | 5632 | 1021 | 5632 | 39 |
| 3 | 1 | 1614.27 | 0.00 | 776 | 818 | 776 | 30 |
| 3 | 2 | 771.939 | $6.81 \times 10^{-170}$ | 725 | 548 | 725 | 30 |
| 3 | 3 | 908.76 | $1.22 \times 10^{-199}$ | 684 | 595 | 684 | 39 |
| 4 | 1 | 16.66 | $4.50 \times 10^{-5}$ | 366 | 19 | 366 | 1 |
| 4 | 2 | 12.51 | $4.05 \times 10^{-4}$ | 388 | 15 | 388 | 1 |
| 4 | 3 | 19.50 | $1.00 \times 10^{-5}$ | 369 | 19 | 369 | 0 |

Table 5.11: Chi-square analysis on filtrand from Patient 923's ascites samples.

| POPULATION | TRIAL | CHI-SQUARE VALUE | P-value | TOTAL CELLS IN EXPERIMENTAL POPULATION | CELLS CAPTURED FROM EXPERIMENTAL POPULATION | TOTAL CELLS IN CONTROL POPULATION | CELLS CAPTURED FROM CONTROL POPULATION |
|---|---|---|---|---|---|---|---|
| 1 | 1 | 88.49 | $5.10 \times 10^{-21}$ | 1126 | 140 | 1126 | 24 |
| 1 | 2 | 112.99 | $2.16 \times 10^{-26}$ | 1095 | 161 | 1095 | 23 |
| 1 | 3 | 81.09 | $2.16 \times 10^{-19}$ | 1085 | 153 | 1085 | 35 |
| 2 | 1 | 594.18 | $3.10 \times 10^{-131}$ | 5998 | 1157 | 5998 | 288 |
| 2 | 2 | 689.52 | $5.68 \times 10^{-152}$ | 6179 | 1266 | 6179 | 296 |
| 2 | 3 | 779.11 | $1.88 \times 10^{-171}$ | 6218 | 1425 | 6218 | 339 |
| 3 | 1 | 74.85 | $5.07 \times 10^{-18}$ | 382 | 115 | 382 | 23 |
| 3 | 2 | 87.38 | $8.95 \times 10^{-21}$ | 372 | 123 | 372 | 22 |
| 3 | 3 | 65.83 | $4.91 \times 10^{-16}$ | 340 | 114 | 340 | 28 |
| 4 | 1 | 3.60 | 0.06 | 470 | 6 | 470 | 1 |
| 4 | 2 | 14.20 | $1.65 \times 10^{-4}$ | 505 | 14 | 505 | 0 |
| 4 | 3 | 1.00 | 0.32 | 435 | 1 | 435 | 0 |

having a high affinity for those markers. The receptor tyrosine kinase, EphA2, is expressed prolifically in patients with ovarian carcinoma.[70] Prior studies have shown that the peptide sequence YSAYPDSVPMMS acts as an ephrin mimetic and is highly selective for EphA2.[49] It was assumed that nanoparticles functionalized with a derivative of this peptide sequence (GGGGYSAYPDSVPMMSK) would preferentially bind cells in populations testing positive for EphA2 expression. Human epithelial antigen (HEA)[64] and the extracellular domain of the MUC16 cell surface protein, CA125,[66-69] have been investigated extensively as potential diagnostic aids for identifying malignant adenocarcinomas in serous effusions. Human epithelial antigen (HEA) is a glycoprotein epitope that exhibits elevated expression levels in metastatic adenocarcinomas.[75] Ber-EP4 has a high affinity for HEA and is commonly used to verify HEA expression.[64] Serum levels of CA125 are elevated in 90% of the patients with ovarian cancer.[76] HEA and CA125 levels were expected to be elevated in the same cell populations expressing high levels of EphA2. Although increased EphA2 expression has been linked to ovarian

carcinomas it is not exclusively expressed by this cell type.[77] The Eph receptor family is one of the largest RTK families and Eph/ephrin receptor signaling is intimately coupled with cell movement, maintenance of cellular boundaries, and blood vessel remodeling.[78, 79] An ephrin mimetic would be expected to bind any cell expressing an Eph receptor but it would also be expected to preferentially bind cells with higher Eph expression.[42] It was postulated that EphA2 receptors or fragments may also be displayed by antigen presenting cells (APC). Macrophages and dendritic cells commonly participate in the anti-tumor response and were expected to populate the serous effusions of ovarian cancer patients.[80] If this were the case, APCs could be targeted by the 17 residue peptide as well. To verify this eventuality, these effusions were also stained with monoclonal antibodies selective for a common dendritic cell and macrophage marker (CD83 and MAC387 respectively). The cell surface molecule,CD83, is one of the most prominent maturation markers for fully mature dendritic cells.[81] The presence of this marker in populations that also tested positive for EphA2 expression would help to substantiate the presence of dendritic cells presenting the EphA2 antigen. However, because tumor cells typically release factors that prevent dendritic cell maturation, low expression levels of this marker were expected.[57, 58]

Single parameter frequency histograms were used to analyze both control and experimental samples. The untreated ascites samples for each patient were used as control specimens and the autoflourescence levels were recorded using a four decade log amplifier. Experimental samples of peritoneal effusions from each patient were challenged in separate trials with anti-CD83, anti-MAC387, BerEP4, anti-EphA2 and anti-

CA125. Each monoclonal antibody had a FITC conjugate, or a secondary antibody with a phycoerythrin conjugate (EphA2). The histograms from the experimental samples were superimposed over those of the control to determine whether there were any variances between the two (Figures 5.22-5.37). From these graphs we can see that 0.22% (Figure 5.23) of the 10,000 events counted for patient 914 samples showed a positive expression for the EphA2 receptor and occurred in gated population P1. The values for P2, P3 and P4 were 16.15% (Figure 5.25), 12.87% (Figure 5.27), and 0.30% (Figure 5.29) respectively. The percentages showing positive EphA2 expression in the samples from patient 923 were 0.36% (Figure 5.31, gate P1), 5.60% (Figure 5.33, gate P2), 2.71% (Figure 5.35, gate P3), and 0.58% (Figure 5.37, gate P4). The covariance between the expression levels of EphA2 and CA125 appear to be positive in gated populations P1, P2, and P3 (Figure 5.22-5.27) of samples from patient 914 and gated populations P1, P2, P3, and P4 (Figure 5.30-5.37) of samples from patient 923. For instance, CA125 and EphA2 were expressed negligibly in P1 of samples from patient 914 (0.16% and 0.22% respectively, Figure 5.22 and 5.23) and in greater numbers (30.90% for CA125 and 16.15% for EphA2) in gated population P2 (Figure 5.24 and 5.25). The highest number of cells expressing CA125, EphA2, HEA, and MAC387 came from gates P2 and P3 for samples from patient 914 (Figure 5.24-5.27). However, infrequent HEA expression was seen correspondingly as 1.43% and 0.75 % in both these populations. For samples from patient 923 the number of cells expressing HEA was 8.06% for P2 (Figure 5.32) and 1.52% for P3 (Figure 5.34). There was also a positive covariance between the number of cells expressing EphA2, HEA, CA125, and MAC387 in P2, P3, and P4 (Figure 5.32-5.36)

and the highest numbers of cells expressing these markers came from P2 (Figure 5.32 and 5.33).

As expected, the expression levels of CD83 were very low for both patient samples. The average CD83+ cell count across all four populations in samples from patient 914 was 0.12% +/- 0.14% (mean +/- standard deviation) and 0.19% +/- 0.28% for patient 923 suggesting that mature dendritic cells were mostly absent from these ascites samples.

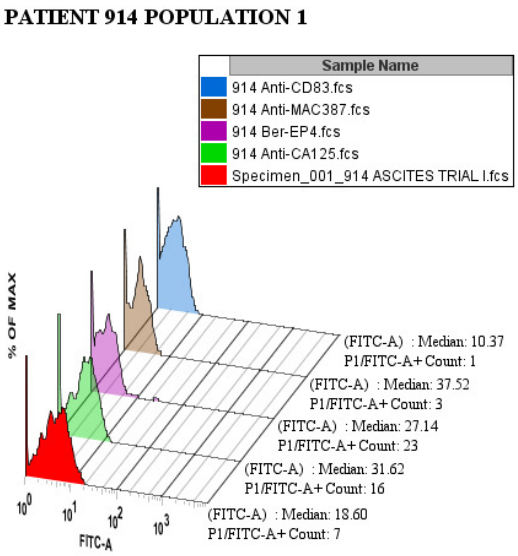


Figure 5.22: Patient sample 914 was stained with a panel of FITC-conjugated monoclonal antibodies. The cell counts and fluorescent intensities for cells testing positive in P1 are compared to autofluorescent levels in a sample of unstained ascites.

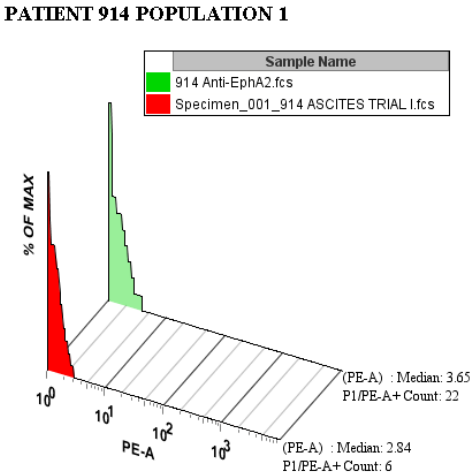


Figure 5.23: Patient sample 914 was stained with PE-conjugated anti-EphA2. The cell counts and fluorescent intensities for cells testing positive in P1 are compared to autofluorescent levels in a sample of unstained ascites.

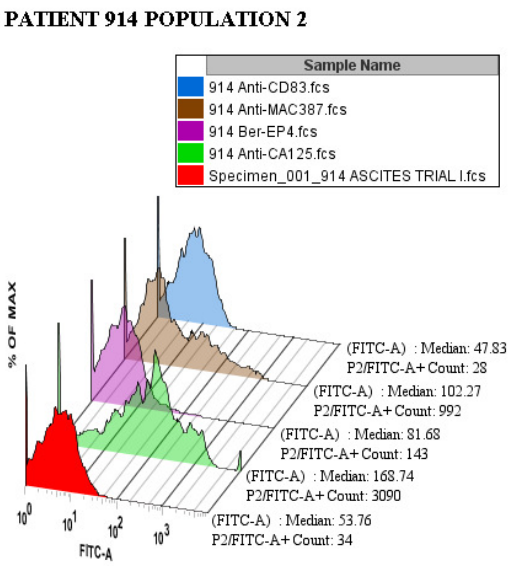


Figure 5.24: Patient sample 914 was stained with a panel of FITC-conjugated monoclonal antibodies. The cell counts and fluorescent intensities for cells testing positive in P2 are compared to autofluorescent levels in a sample of unstained ascites.

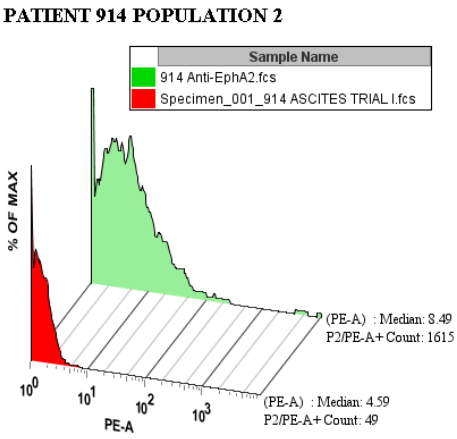


Figure 5.25: Patient sample 914 was stained with PE-conjugated anti-EphA2. The cell counts and fluorescent intensities for cells testing positive in P2 are compared to autofluorescent levels in a sample of unstained ascites.

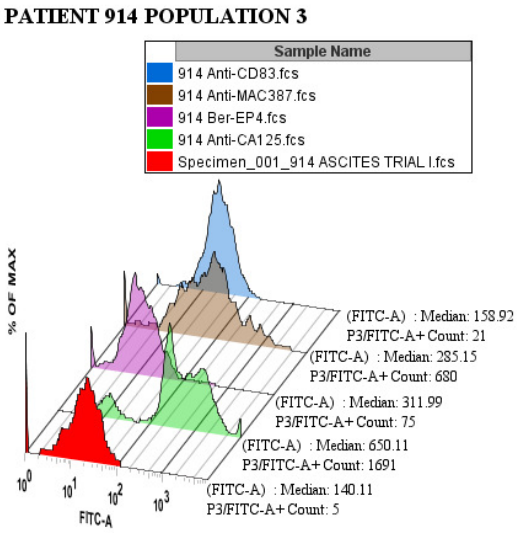


Figure 5.26: Patient sample 914 was stained with a panel of FITC-conjugated monoclonal antibodies. The cell counts and fluorescent intensities for cells testing positive in P3 are compared to autofluorescent levels in a sample of unstained ascites.

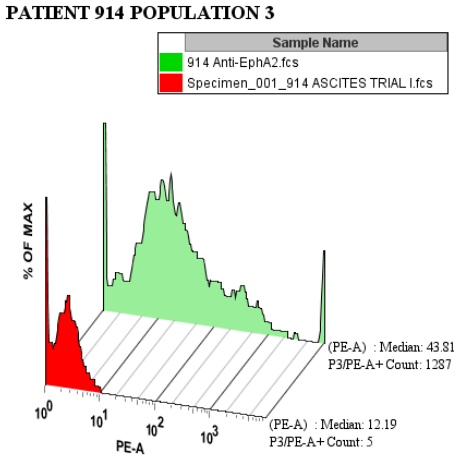


Figure 5.27: Patient sample 914 was stained with PE-conjugated anti-EphA2. The cell counts and fluorescent intensities for cells testing positive in P3 are compared to autofluorescent levels in a sample of unstained ascites.

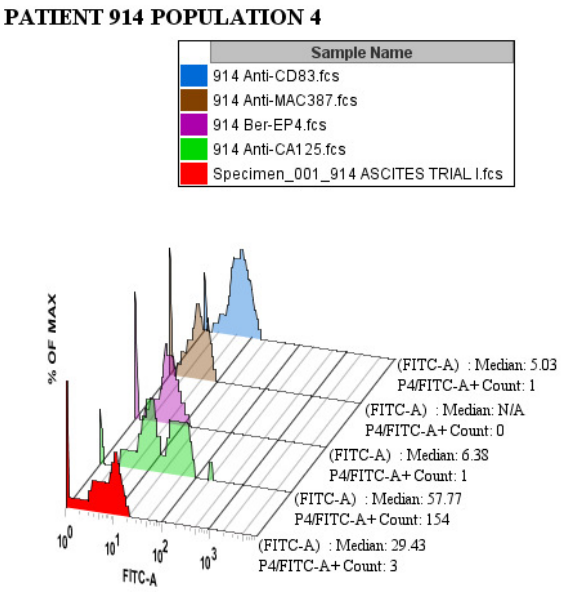


Figure 5.28: Patient sample 914 was stained with a panel of FITC-conjugated monoclonal antibodies. The cell counts and fluorescent intensities for cells testing positive in P4 are compared to autofluorescent levels in a sample of unstained ascites.

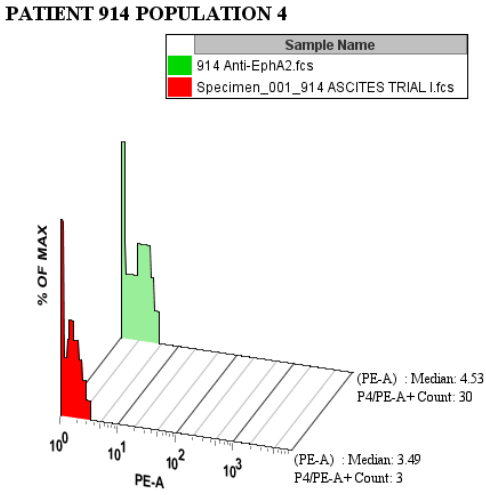


Figure 5.29: Patient sample 914 was stained with PE-conjugated anti-EphA2. The cell counts and fluorescent intensities for cells testing positive in P4 are compared to autofluorescent levels in a sample of unstained ascites.

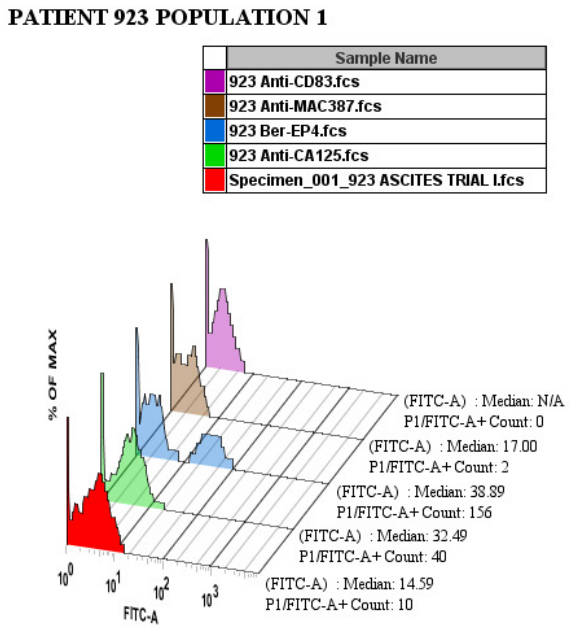


Figure 5.30: Patient sample 923 was stained with a panel of FITC-conjugated monoclonal antibodies. The cell counts and fluorescent intensities for cells testing positive in P1 are compared to autofluorescent levels in a sample of unstained ascites.

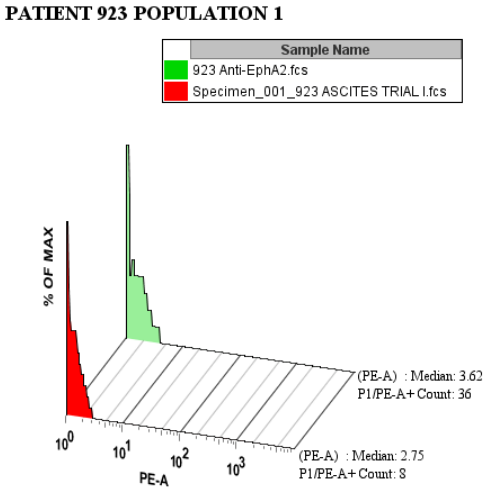


Figure 5.31: Patient sample 923 was stained with PE-conjugated anti-EphA2. The cell counts and fluorescent intensities for cells testing positive in P1 are compared to autofluorescent levels in a sample of unstained ascites.

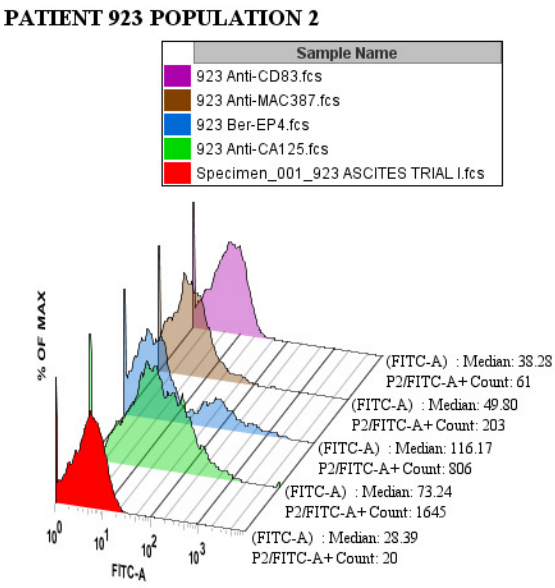


Figure 5.32: Patient sample 923 was stained with a panel of FITC-conjugated monoclonal antibodies. The cell counts and fluorescent intensities for cells testing positive in P2 are compared to autofluorescent levels in a sample of unstained ascites.

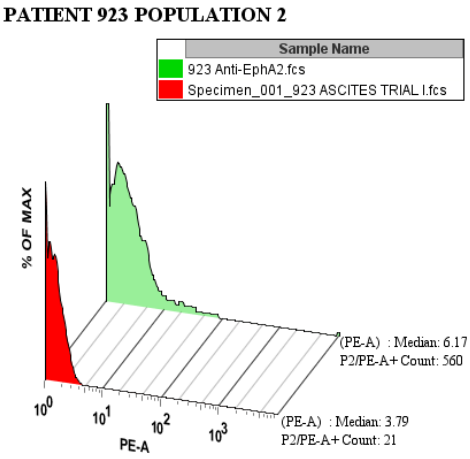


Figure 5.33: Patient sample 923 was stained with PE-conjugated anti-EphA2. The cell counts and fluorescent intensities for cells testing positive in P2 are compared to autofluorescent levels in a sample of unstained ascites.

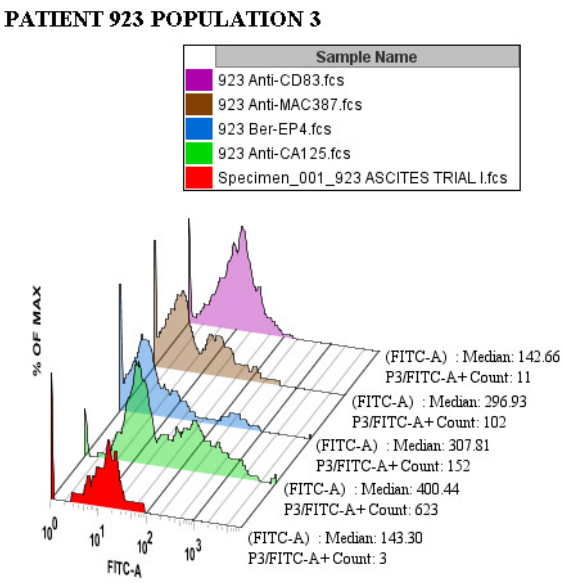


Figure 5.34: Patient sample 923 was stained with a panel of FITC-conjugated monoclonal antibodies. The cell counts and fluorescent intensities for cells testing positive in P3 are compared to autofluorescent levels in a sample of unstained ascites.

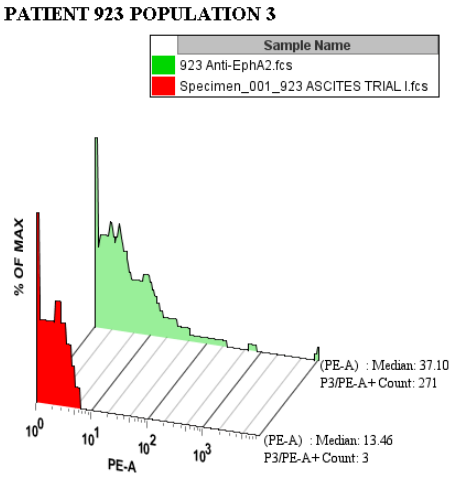


Figure 5.35: Patient sample 923 was stained with PE-conjugated anti-EphA2. The cell counts and fluorescent intensities for cells testing positive in P3 are compared to autofluorescent levels in a sample of unstained ascites.

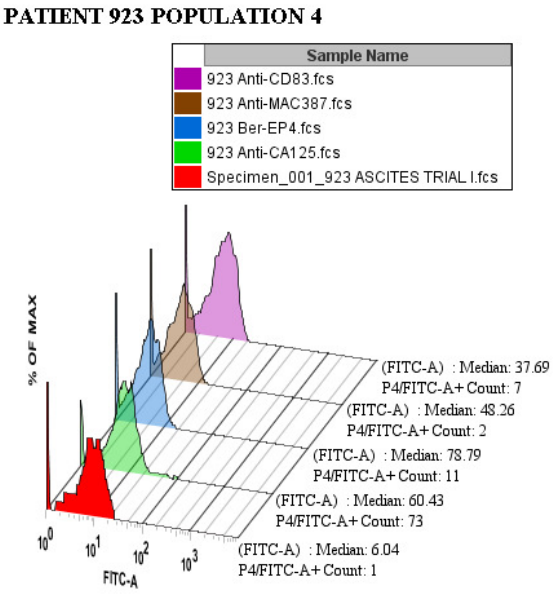


Figure 5.36: Patient sample 923 was stained with a panel of FITC-conjugated monoclonal antibodies. The cell counts and fluorescent intensities for cells testing positive in P4 are compared to autofluorescent levels in a sample of unstained ascites.

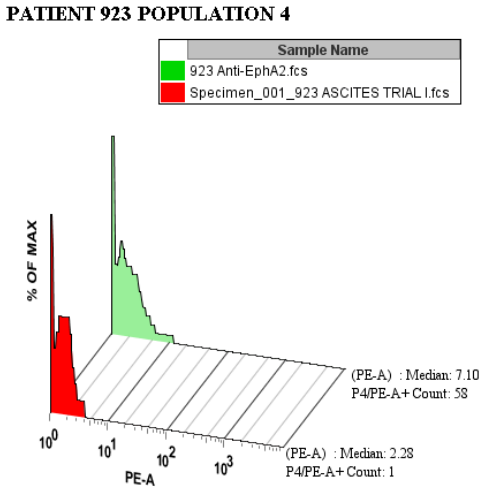


Figure 5.37: Patient sample 923 was stained with PE-conjugated anti-EphA2. The cell counts and fluorescent intensities for cells testing positive in P4 are compared to autofluorescent levels in a sample of unstained ascites.

Discussion.

In our previous study, we demonstrated that ovarian cancer cells could be selectively removed from the peritonea of mice using magnetic nanoparticles conjugated to a derivative of the ephrin mimetic peptide YSAYPDSVPMMS. Based on these results we proposed that our technique might be employed as a viable modality for preventing the metastatic spread of carcinoma cells in ovarian cancer patients.[42] In this study, we provide further evidence of this possibility by demonstrating that ovarian cancer cells can be selectively removed from human peritoneal effusions using superparamagnetic nanoparticles conjugated to the ephrin mimetic peptide GGGGYSAYPDSVPMMSK. The EphA2 receptor has been previously shown to be highly expressed in ovarian cancer cells and to bind specifically to the YSAYPDSVPMMS peptide.

Flow cytometry was used to analyze ascites samples from two patients diagnosed with late stage serous papillary ovarian cancers. Bivariate displays of forward and side scatter patterns obtained from sample analyses were examined and visually discreet regions were gated. The number of cells isolated using the peptide conjugated nanoparticle was highly significant relative to non-conjugated particles ($p < 0.01$, Chi-square test). As a further test of the effectiveness of our method, we looked for a correlation between the cells extracted and the expression of EphA2. We found that for both patient samples the highest numbers of cells were extracted from the populations having the highest numbers of cells expressing EphA2 and there was a positive covariance between these variables in all four populations.

To validate that the extracted cells expressing EphA2 were ovarian cancer cells, we tested for the presence of two additional established markers of ovarian cancer cells. We found that all three markers were significantly expressed in the human ascites cell populations where we were able to extract significantly large numbers of cells using the peptide conjugated nanoparticles. Collectively our findings are consistent with the hypothesis that magnetic nanoparticles with ligands having a high affinity for antigens expressed on ovarian cancer cells can be used to isolate free floating cancer cells from the peritoneal fluid. Since it is widely acknowledged that these free floating ovarian cancer cells are responsible for the majority of ovarian cancer metastases, it is our hope that our method may eventually be applied to clinical practice with therapeutic benefit.

# CHAPTER 6

# OVARIAN CANCER SURVIVAL STUDY

## Introduction

Another important progression from our initial capture studies was the validation as to whether the proposed cell capture modality would be successful at prolonging the lives of patients afflicted with ovarian carcinomas. To move toward that goal the therapy would need to be tested against a metastatic ovarian cancer animal model. To date, many groups have found that while the development of subcutaneous tumors in animal models can be facile the development of a metastatic model is much more challenging. Coupled with the difficult development issues comes the equally difficult task of monitoring the dissemination of micrometastases which can often remain outside the range of detectability. The ideal model would be comprised of tumorogenic cells with a high proliferative potential. The proliferation would also need to be measurable both qualitatively and quantitatively.

## The Model

Vascular endothelial growth factor (VEGF) is a growth factor involved in angiogenesis. A constant blood supply is critical to the rapid expansion of highly prolific cell lines. Malignant cell lines have this need and their expansive potential is increased by high levels of this growth factor. In an effort to develop an ovarian cancer cell line with high proliferation potential, Zhang et al. transfected a murine ovarian cancer cell line (ID8) with the gene for VEGF expression.[35] The cell line was also transfected with

the gene for green fluorescent protein (GFP) expression, which has become a common technique for monitoring the metastatic spread of malignant cells. The modified ID8 cell line (ID8 GFP VEGF) had two advantages. By expressing its own copies of the VEGF protein it could stimulate angiogenesis and thereby increase the proximitive blood supply. By expressing GFP its dissemination could be visibly monitored. It had even been shown that the presence of GFP in cells could be quantitatively measured by taking optical density measurements using a microplate reader.[37] Combining the ID8 GFP VEGF cell line with the analytical technique gave us the highly proliferative and traceable cell line we were seeking.

Prior to employing the model we would need to test it and establish our data points. Mimicking the published model of Zhang et al. we resolved to inoculate 6-7 week old female C57BL/6 mice with the ID8 GFP VEGF cell line. A control group of the same age and breed was inoculated with and ID8 cell line expressing only GFP (ID8 GFP). Comparing the progression of the two cell lines helped us to establish average longevity and work out a method for quantifying the number of metastases. Many of the specifics of testing this model have already been covered in Chapter 2. As previously mentioned, 4 mice from each of the ID8 GFP and ID8 GFP VEGF groups would be analyzed at 4 different time points (2,4,6, and 8 weeks). The external ventral region around the peritoneum was photographed using bright field to log either the existence of or lack of visible tumors. Each mouse was then necropsied. The peritoneal cavity was exposed and photographed using bright and dark field microscopy with the peritoneal wall intact. Figure 6.1.A and 6.1.B were taken at week 4 of a mouse from the

ID8 GFP group. Figure 6.2.A and 6.2.B were taken at week 4 of a mouse from the ID8 GFP VEGF group. The dark field exposures were excited at 488 nm and metastatic sites are visible in Figure 6.2.B. The liver, lung, spleen, and a 1 cm X 1 cm section of the peritoneal wall were removed and then photographed using dark and bright field microscopy. The organs were chosen because of their localization to the peritoneum

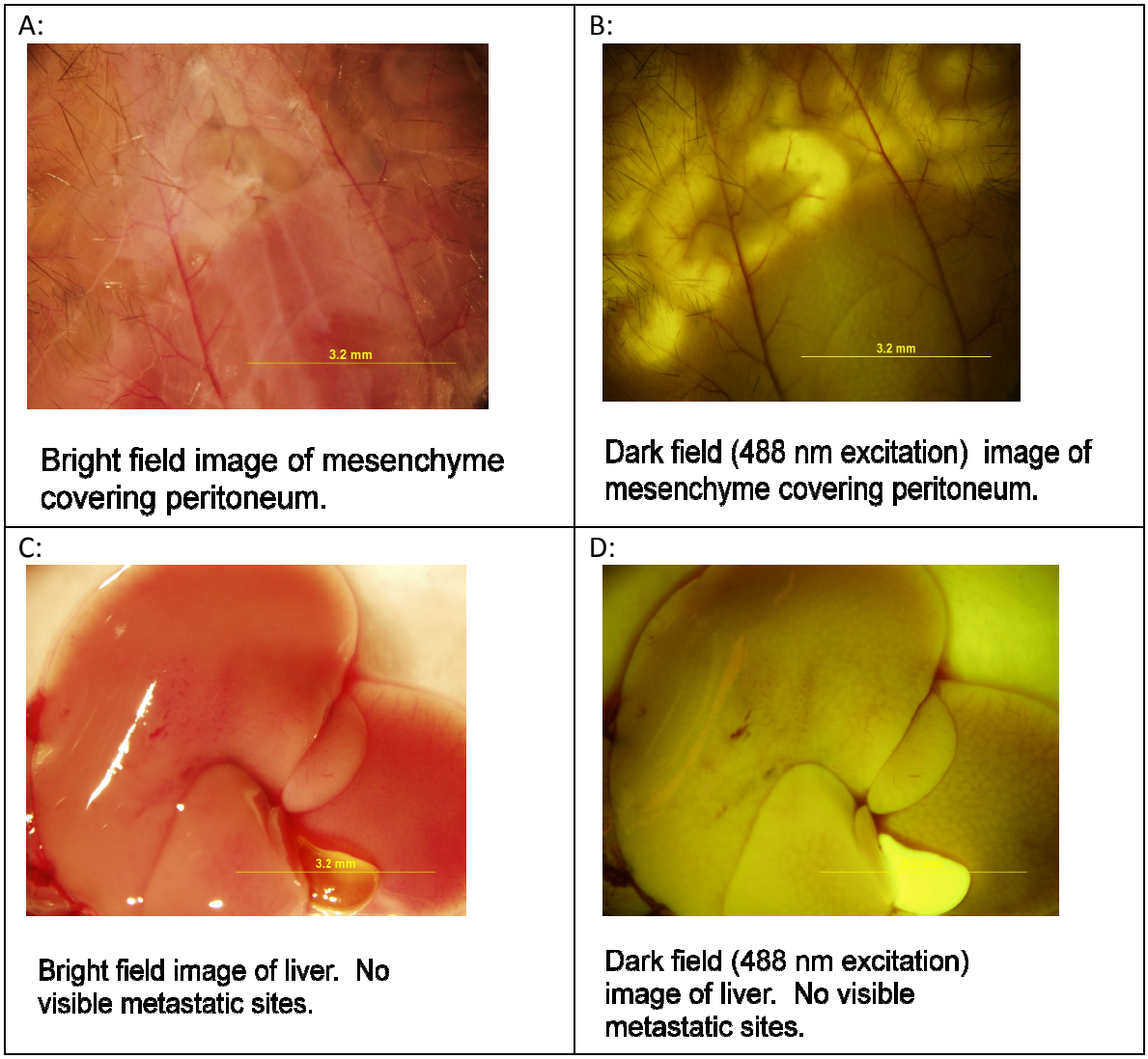


Figure 6.1: Panel of bright field and dark field images taken of a necropsied mouse from the ID8 GFP group at week 4.

E:

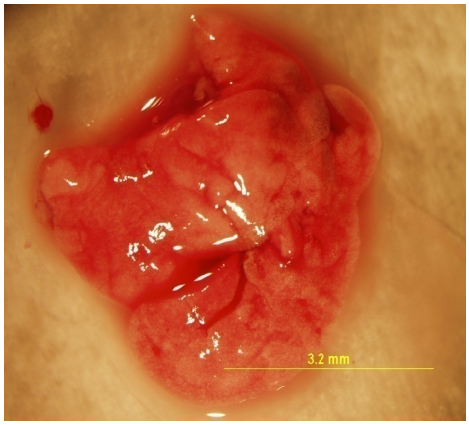


Bright field image of lung. No visible metastatic sites.

F:

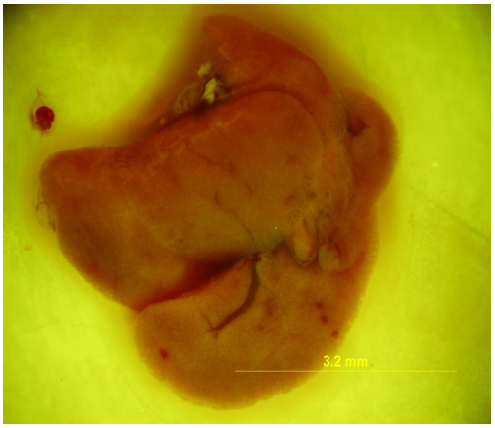


Dark field (488 nm excitation) image of lung.

G:

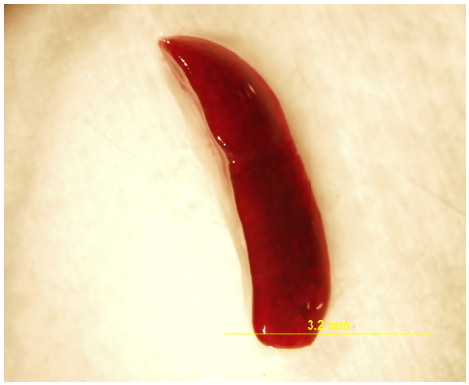


Bright field image of spleen.

H:

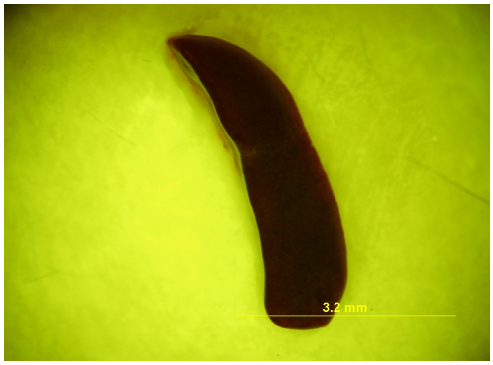


Dark field (488 nm excitation) image of spleen.

I:

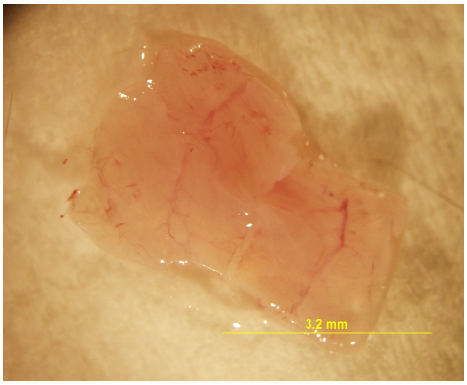


Bright field image of 1 x 1 cm section of the peritoneal wall.

J:

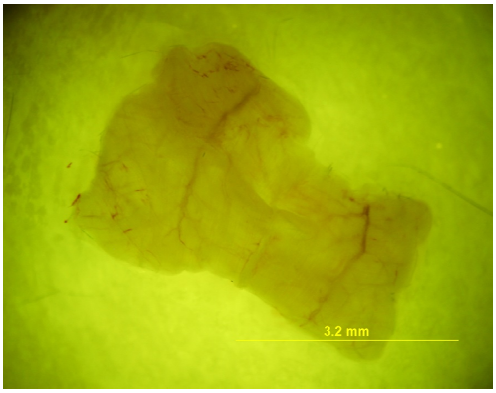


Dark field (488 nm excitation) image of peritoneal wall.

Figure 6.1 continued

A:

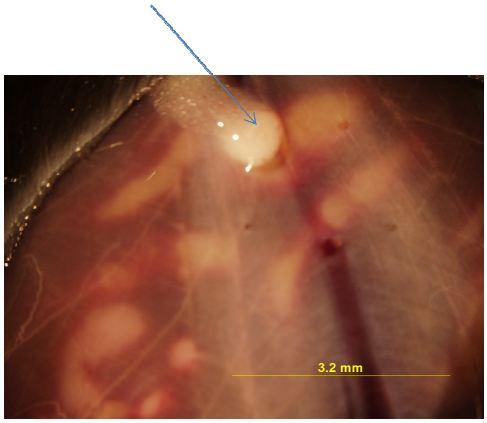


Bright field image of mesenchyme covering peritoneum. Tumor located near what was probably the inoculation site.

B:

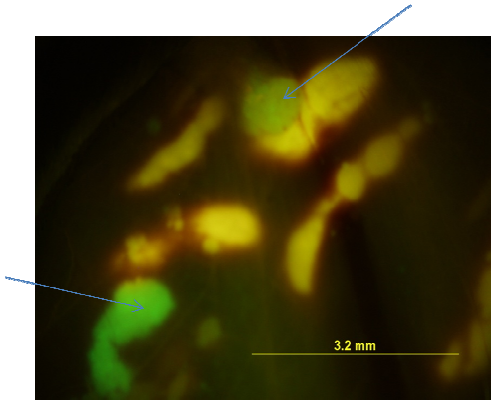


Dark field (488 nm excitation) image of mesenchyme covering peritoneum. Arrows indicate tumor and metastatic sites.

C:

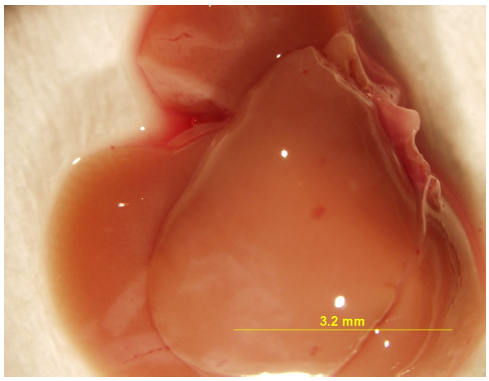


Bright field image of liver. No visible metastatic sites.

D:

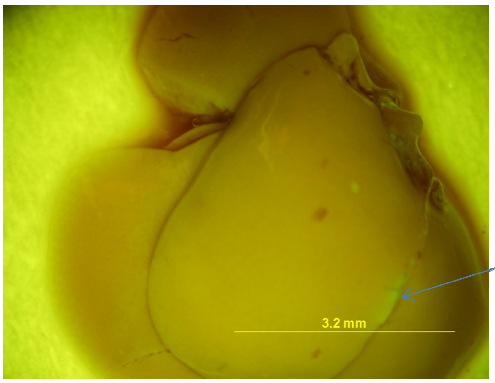


Dark field (488 nm excitation) image of liver. Some fluorescence may be connective tissue.

Figure 6.2: Panel of bright field and dark field images taken of a necropsied mouse from the ID8 GFP VEGF group at week 4.

E:

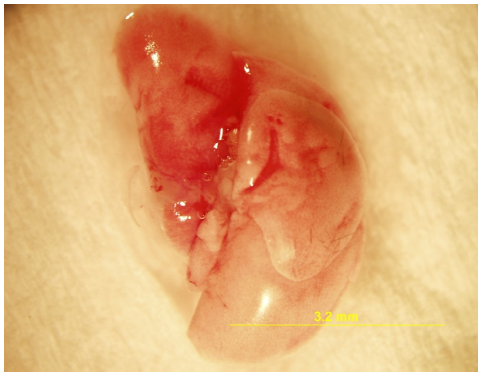

Bright field image of lung.

F:

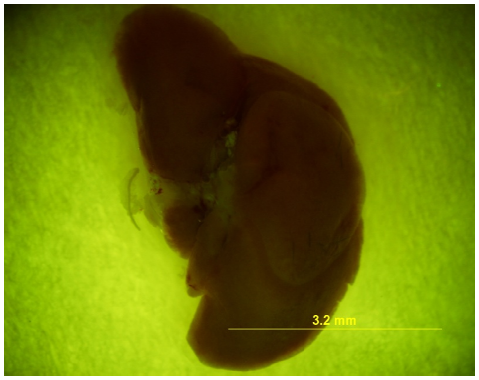

Dark field (488 nm excitation) image of lung.

G:

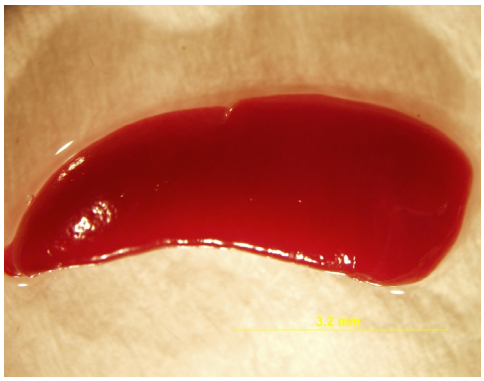

Bright field image of spleen. Appears much larger than spleens observed at 2 week time point.

H:

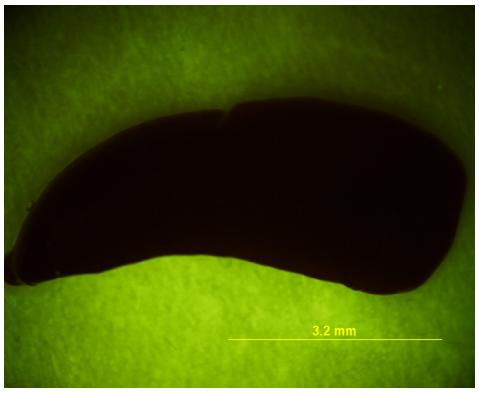

Dark field (488 nm excitation) image of spleen.

I:

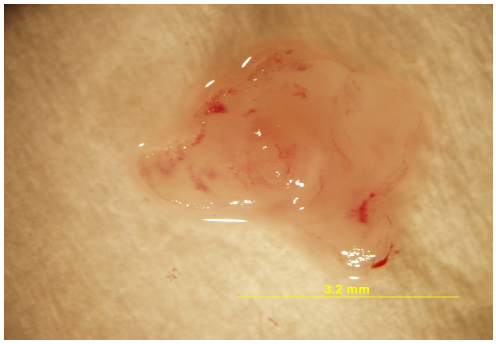

Bright field image of 1 x 1 cm section of the peritoneal wall.

J:

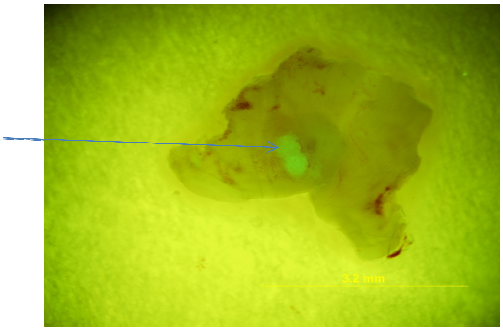

Dark field (488 nm excitation) image of peritoneal wall. Tumor fluoresces (arrow).

Figure 6.2 continued

and continual contact with the peritoneal fluids. The representative photos taken from mice in the ID8 GFP group at week 4 are featured in Figure 6.1.C-6.1.J. There is no significant visible fluorescence in any of the dark field photos which would indicate that the ID8 GFP line is not well established or has not localized in any of the observed regions. Representative photos taken from mice in the ID8 GFP VEGF group at week 6 are featured in Figure 6.2.C-6.2.J. There appear to be visible indications of metastatic sites on the liver (Figure 6.2.D) and a possibly subcutaneous tumor nodule in the peritoneal wall section (Figure 6.2.J) that was probably near the injection site. An interesting observation is the large difference between the sizes of the spleens taken from the control and experimental groups. The experimental group spleen (Figure 6.2.H) appears significantly larger than the control. The visual evidence from week 4 appeared to indicate that the ID8 GFP VEGF proliferation was more expansive than that of the control.

To obtain a more quantitative comparison of the expansive nature of the two cell lines, the excised tissues and organs were homogenized and the slurry produced was analyzed for optical density. The results of the optical density measurements obtained for the organs and tissues from each mouse analyzed in both the control and experimental groups presented in Figures 6.3.A-6.3.E. The standard deviation for the four trials is included in the plot and the data was normalized to optical density per mg of organ or tissue. The data from these graphs illustrates that by week 4 the ID8 GFP VEGF cell line was more prolific than the control. The bright field and dark field photographs taken of tissues and organs from the mice in the control and experimental

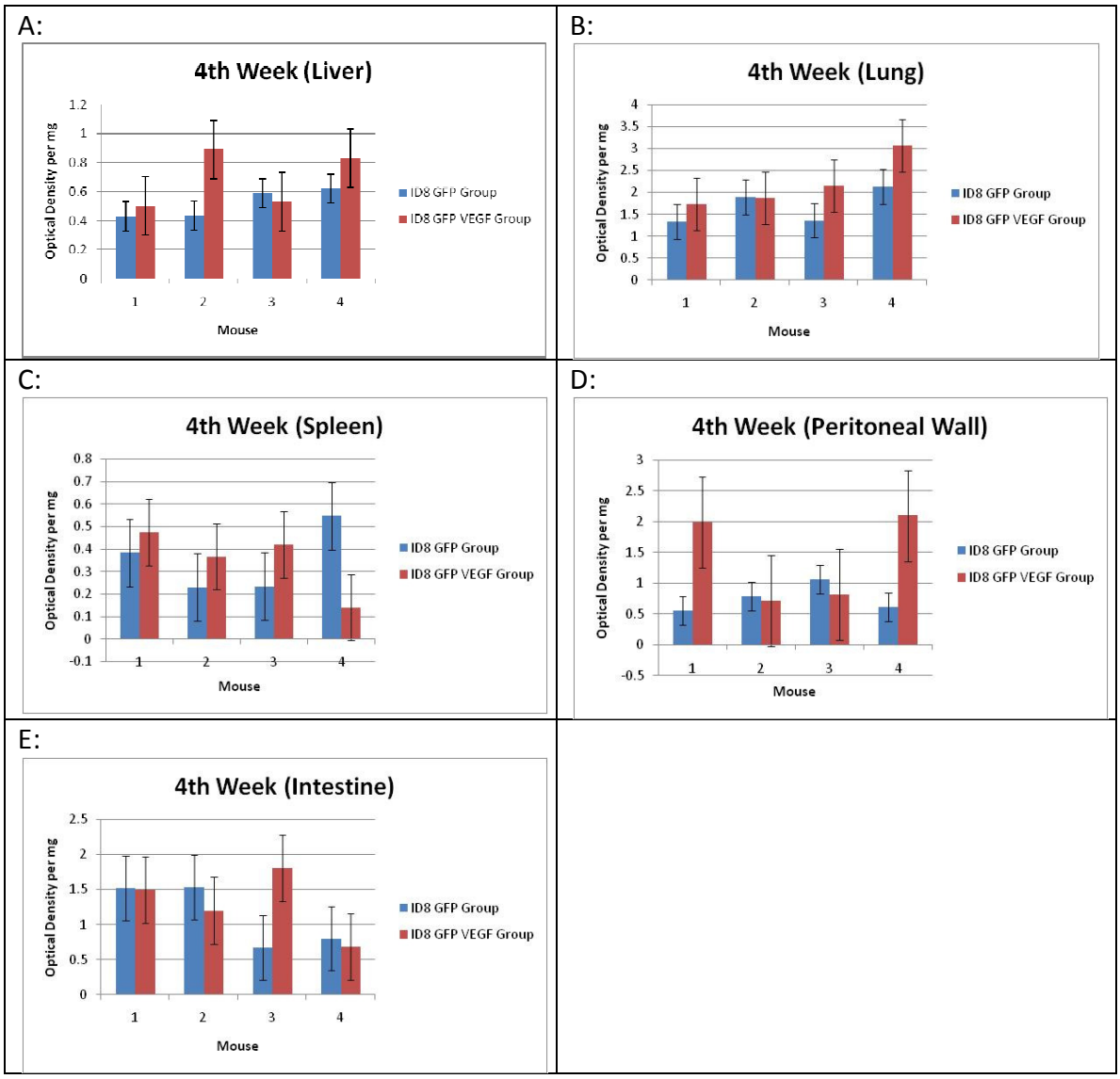


Figure 6.3: Week 4 comparisons of optical density measurements taken on tissues and organs removed from ID8 GFP and ID8 GFP VEGF groups.

groups at Week 6 are featured in Figures 6.4.A-6.4.J and 6.5.A-6.5.J. The superiority of the expansive potential of the ID8 GFP VEGF cell line over that of the ID8 GFP group is visibly apparent when comparing the dark field images of the exposed peritonea (Figures 6.4.B and 6.5.B).

A:

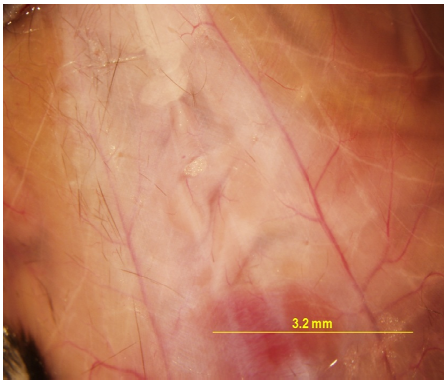


Bright field image of mesenchyme covering peritoneum.

B:

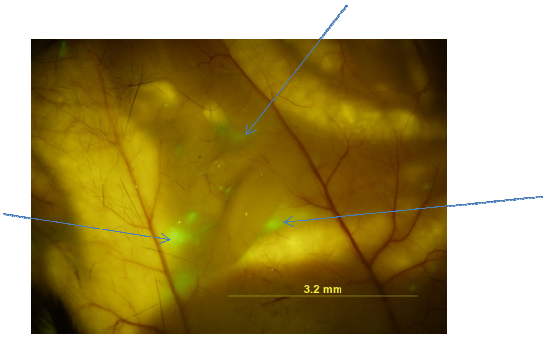


Dark field (488 nm excitation) image of mesenchyme covering peritoneum. Several metastatic sites visible in the arrows indicated by arrows.

C:

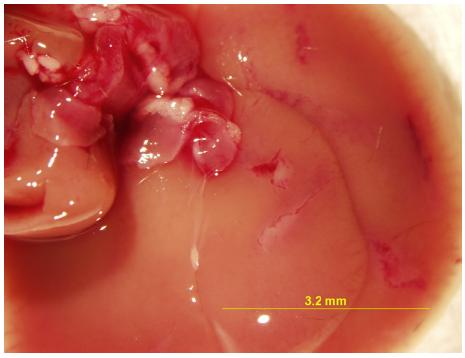


Bright field image of liver. Multiple lesions appear on liver that may have been made during necropsy.

D:

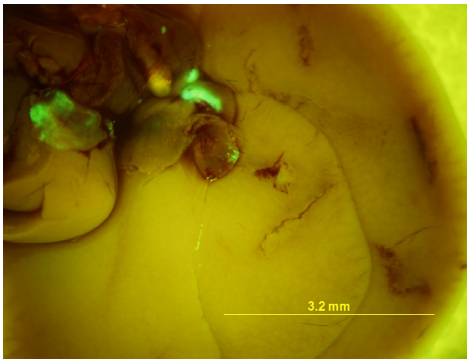


Dark field (488 nm excitation) image of liver. Fluorescent sites may be connective tissue and not metastatic.

Figure 6.4: Panel of bright field and dark field images taken of a necropsied mouse from the ID8 GFP group at week 6.

E:


Bright field image of lung. No visible metastatic sites.

F:

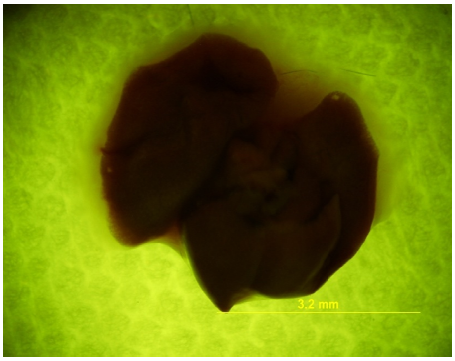


Dark field (488 nm excitation) image of lung.

G:

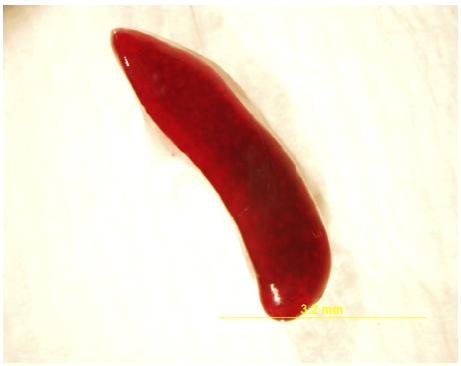


Bright field image of spleen.

H:

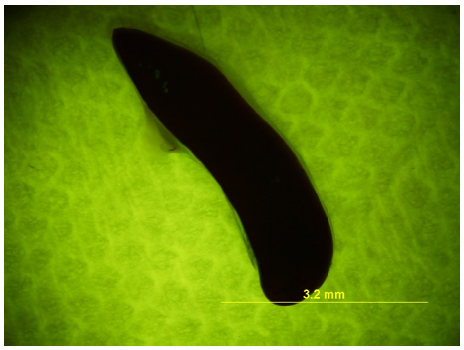


Dark field (488 nm excitation) image of spleen.

I:

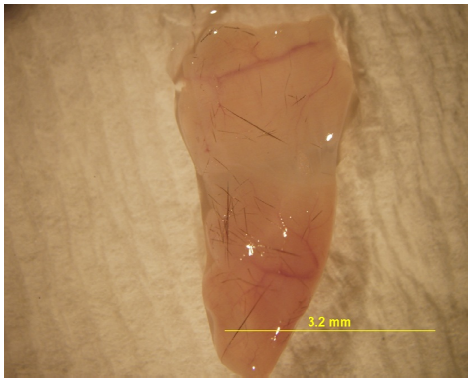


Bright field image of 1 x 1 cm section of the peritoneal wall.

J:

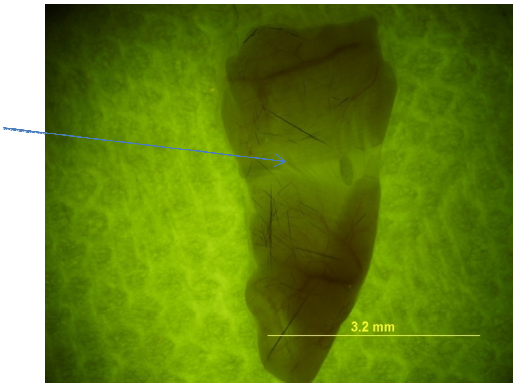


Dark field (488 nm excitation) image of peritoneal wall. Possible tumor site indicated by arrow.

Figure 6.4 continued

A:

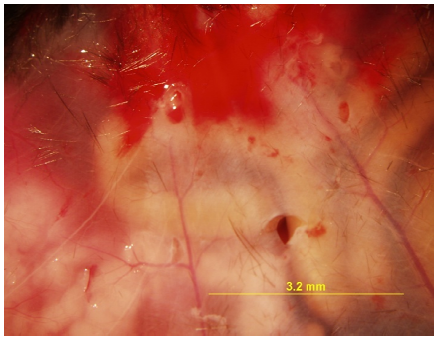


Bright field image of mesenchyme covering peritoneum.

B:

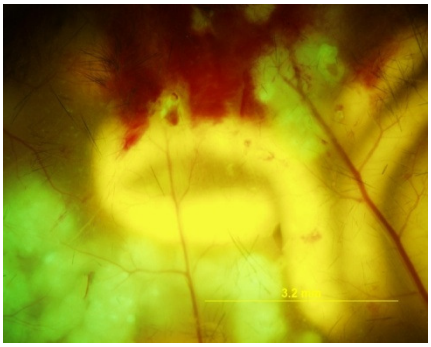

Dark field (488 nm excitation) image of mesenchyme covering peritoneum. Extensive fluorescent regions are believed to be malignant tissue.

C:

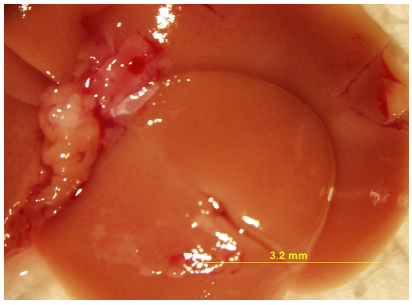


Bright field image of liver. No visible metastatic sites.

D:

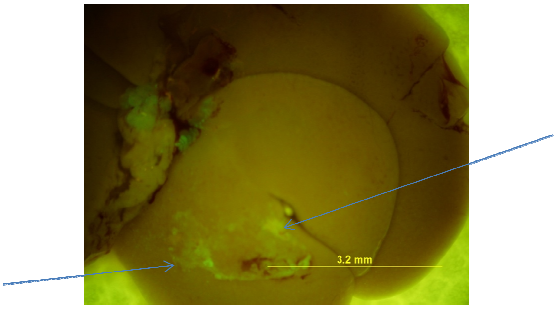


Dark field (488 nm excitation) image of liver. Arrows indicate what may be malignant tissue or connective tissue.

Figure 6.5: Panel of bright field and dark field images taken of a necropsied mouse from the ID8 GFP VEGF group at week 6.

E:

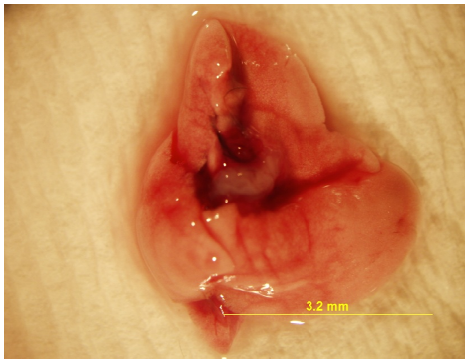


Bright field image of lung. No visible metastatic sites.

F:

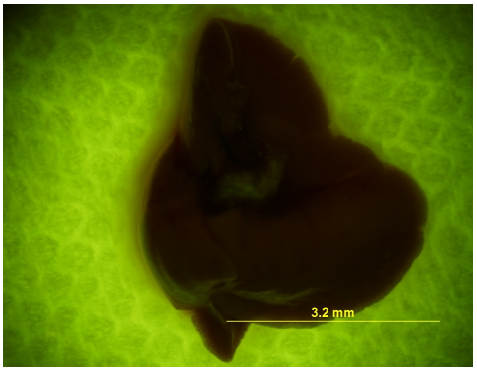


Dark field (488 nm excitation) image of lung.

G:

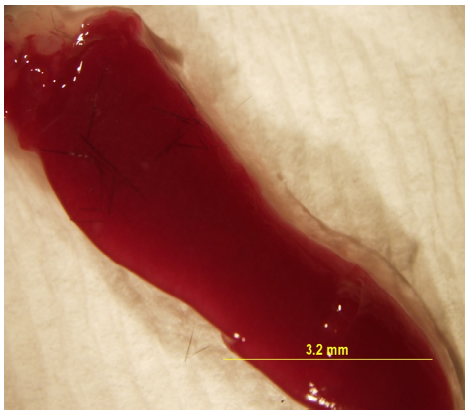


Bright field image of spleen. Spleen is very large.

H:

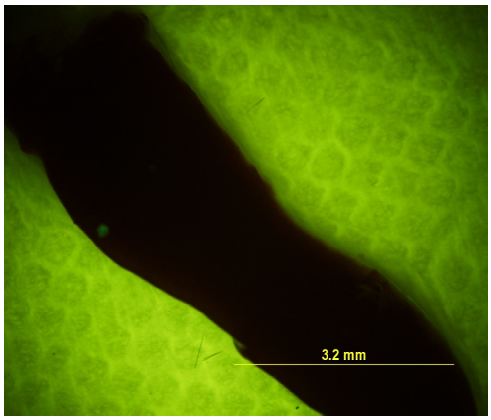


Dark field (488 nm excitation) image of spleen.

I:

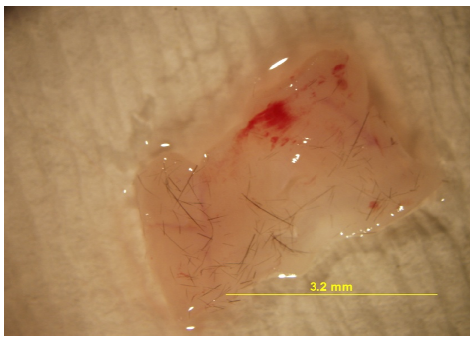


Bright field image of 1 x 1 cm section of the peritoneal wall.

J:

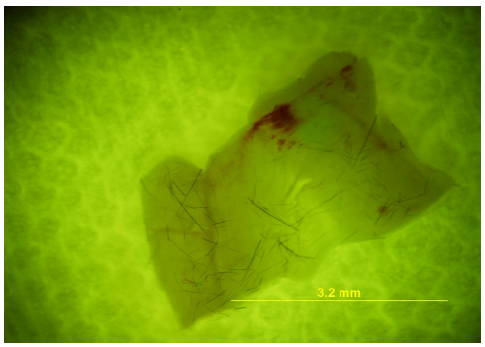


Dark field (488 nm excitation) image of peritoneal wall.

Figure 6.5 continued

The study could not be carried to week 8 because all the members of the ID8 GFP VEGF group had either died or had to be euthanized because of the accumulation of large volumes of ascites (≥ 150% of body mass). This result gave us the expected average mortality date for the ID8 GFP VEGF group. It was also clear from the continual accumulation of ascites throughout the group after week 4 that weight gain could be used as a non-invasive means to monitor metastatic progression.

**Therapy**

Having grasped the mechanics of our metastatic model and planned a strategy for data collection I moved on to working out the logistics of the therapeutic system. As mentioned in Chapter 2, three elimination methods were considered for removing the MNPs. The method illustrated in Figure 6.6.A involved infusing the mice intraperitoneally with the MNPs, allowing the MNPs to circulate in the peritoneal cavity, and eventually removing them with the circulatory pump. The design was first tested on a nu/nu 6 month old mouse that had never been injected with an ovarian cancer cell line. The extracorporeal circuit was first primed with a sterile PBS buffer solution and the mouse was cannulated in the ventral surface of the peritoneum with a 21.5 gauge 1" needle (inlet). The outlet needle was submerged into a vial of sterile PBS and the pump was engaged at a flow rate of 2 mL/min until 7 mL of the sterile PBS had been pumped into the peritoneal cavity of the mouse. The pump was disengaged and the outlet needle was used to cannulate the mouse toward the lower right flank of the peritoneal

A: Extracorporeal circuit and pump.

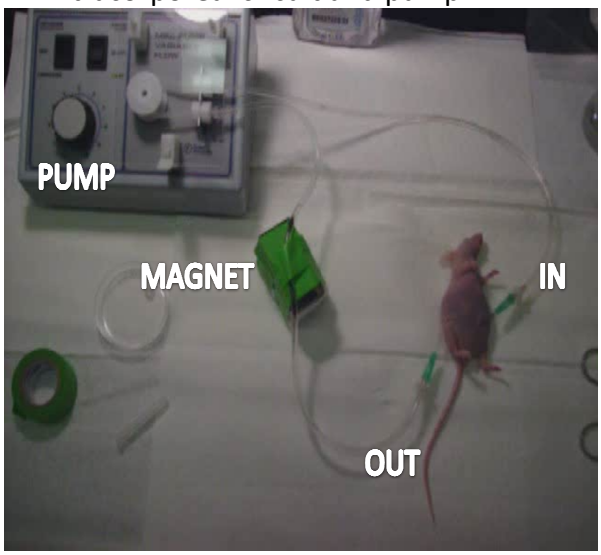


B: Arrow indicates nanoparticles that collected in section of tubing that was placed over a 2500 Gauss neodymium magnet.

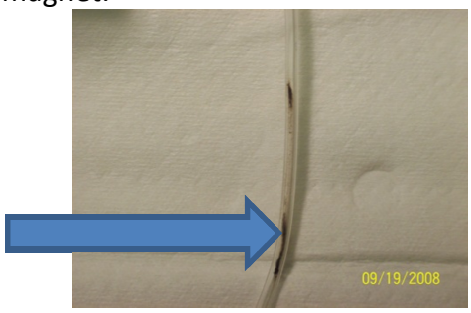


C: Photo taken 4 days postoperatively of mouse showing no signs of complications from the procedure.


D: Arrow indicates small bruise where needle perforated skin. Photo taken 4 days postoperatively.

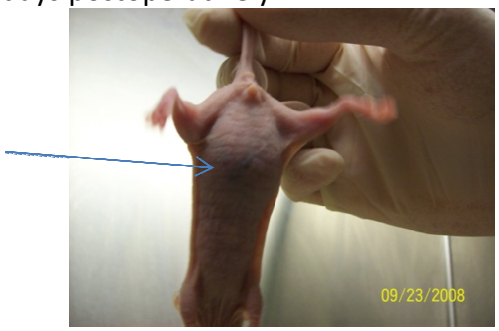


Figure 6.6: Preliminary study performed to assess the viability of eliminating magnetic nanoparticles from the peritoneum of a mouse using an extracorporeal circuit, magnet, and peristaltic pump.

cavity (Figure 6.6.A). The mouse was then injected IP with 100 µL of MNPs coated with polygalacturonic acid and having no functional conjugates. The abdomen of the mouse was massaged for 1 min to disseminate the MNPs throughout the peritoneal cavity. The pump was engaged and allowed to circulate the fluids through the peritoneum for 3

minutes. The inlet needle was removed from the peritoneum and place in a graduated cylinder where it remained until 7 mL of fluid had filled the cylinder. Figure 6.6.B shows the magnetic nanoparticles that collected in the section of tubing bound to the 2500 gauss neodymium magnet. The mouse was monitored for 4 days postoperatively and appeared to show no serious signs of complications from the procedure (Figure 6.6.C-6.6.D).

A similar procedure (Figure 6.7.A-6.7.B) was performed on a residual member of the ID8 GFP control group that had survived out to week 10 in the previously described metastatic model test. This mouse however was injected with 100 µL of MNPs (1 mg/mL) that were coated with glucuronic acid and conjugated to the YSA peptide. The cycle time on the pump was increased from 3 to 10 min and three glass capillary tubes measuring 7 in were attached to the circuit and placed between two stacked 6000 gauss neodymium magnets to increase the exposure time of the MNPs to the magnetic field. At no point during the test were particles seen collecting in the capillary tubes (Figure 6.7.B). The mouse was necropsied postoperatively and it was discovered that the peritoneum of the mouse contained a great deal of malignant growth. The particles had aggregated densely in the malignant material (Figure 6.7.C-6.7.D ). This discovery suggested that particles injected IP might bind to internal tumor sites and not be able to be non-invasively eliminated. To prevent this eventuality the experiment was repeated with a single modification. An external 25 mL mixing vial was added to the circuit where the particles could be injected and contact the cells for an extended period without needing to enter the peritoneum (Figure 6.8.A-6.8.B). Figure 6.8.C shows that the

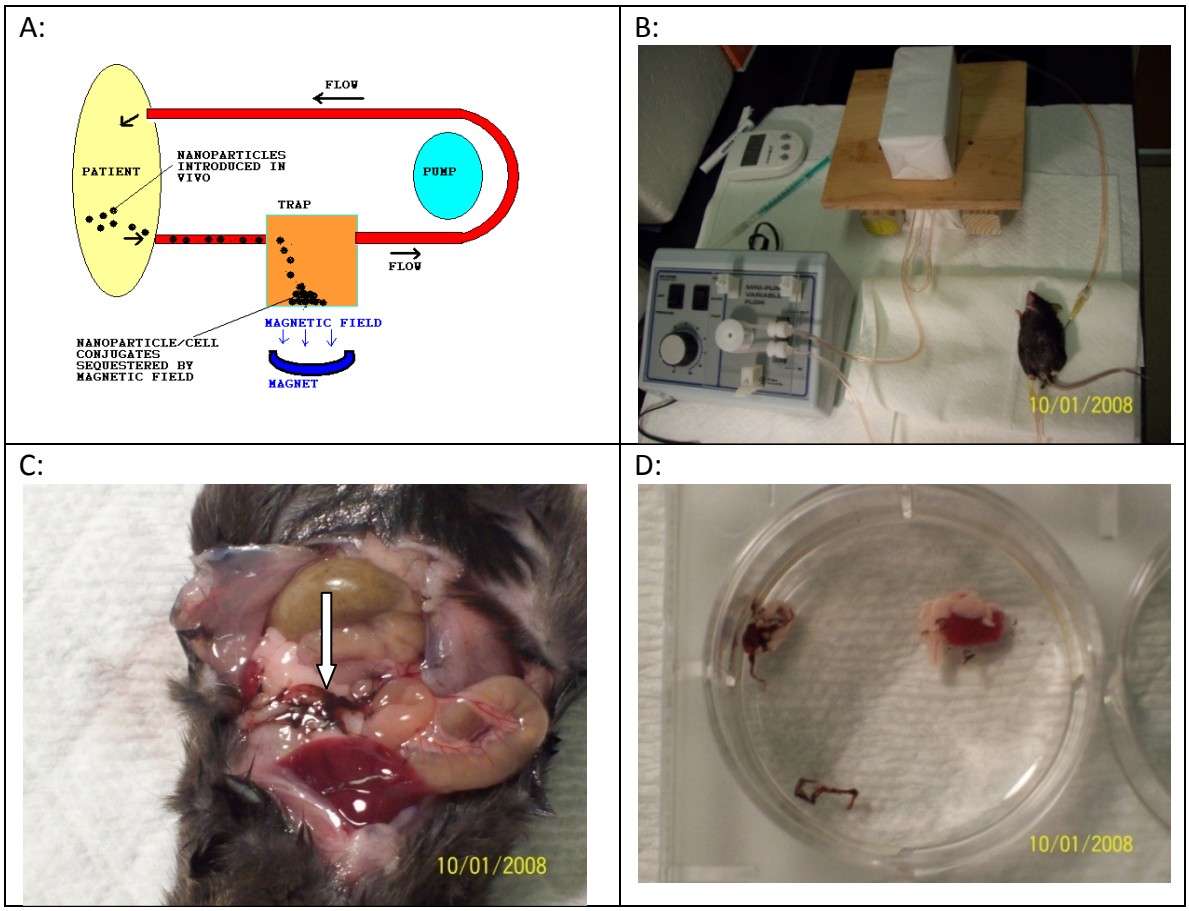


Figure 6.7: Elimination of magnetic nanoparticles injected IP. A: Schematic for particles being delivered IP. B: Photo of actual setup. C: View of exposed peritoneal region postoperatively. Arrow points to accumulation of particles on tumor mass. D: Excised tumor mass bound to MNPs. Tissues could be moved around using a magnet.

particles were successfully captured in the capillary tubing but it was noticed that the particles would occlude the capillary and the fluid pressure would break them free returning them to circulation and possibly to the peritioneum. It was this last observation that prompted the development of mechanism fully detailed in Chapter 2 (Figure 2.10). In this final embodiment the capillary tubes were supplanted with a 15 mL glass vial that would be strapped to the side of the 6000 gauss magnet. This version of the therapeutic system was tested with 5 female C57BL/6 mice that had previously

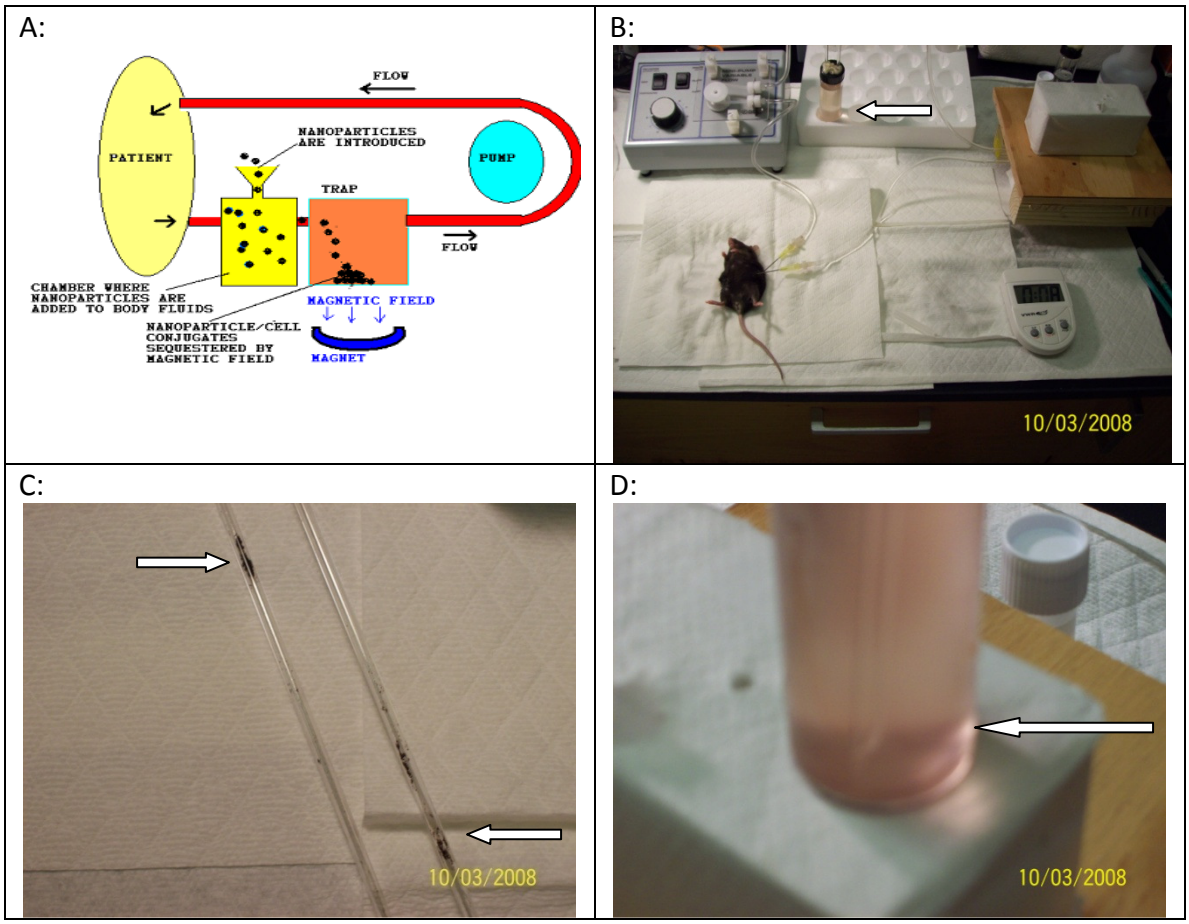


Figure 6.8: Using magnetic nanoparticles to externally remove cancer cells injected IP. A: Schematic for particles remaining external B: Photo of actual setup. The arrow is pointing to the external chamber where the MNPs have been added. C: View of particles sequestered by magnets. D: Mixing cartridge sitting on top of magnet. Arrow indicates the accumulation of magnetized cells at the bottom of the vial.

been injected IP with 7 million ID8 GFP VEGF cells. The magnetic filtrand that collected in the vial attached to the magnet was inspected using fluorescent microscopy after being washed 3x with distilled water. Figure 6.9.A shows a bright field image of the magnetic filtrand that was collected. Figure 6.9.B shows the magnetic filtrand collected using dark field microscopy (488 nm excitation). The GFP expressing cells are seen in this photo bound to the collected MNPs.

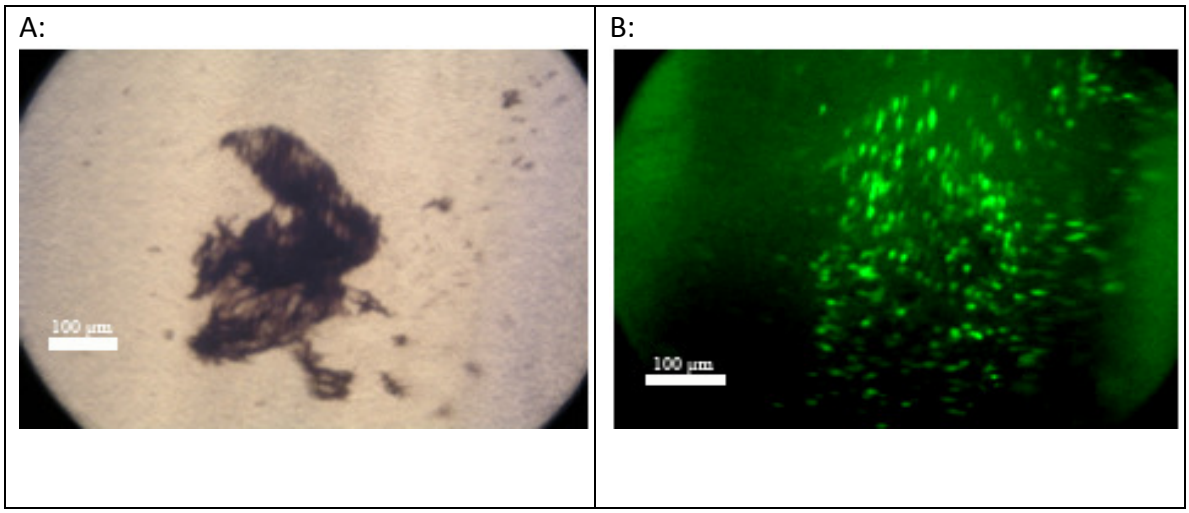


Figure 6.9: Magnetic filtrand retrieved from magnetic filter. A: Bright field image (10x). B: Dark field image showing GFP expressing cancer cells bound to magnetic particles (10x).

**Survival Study**

The data from testing the metastatic model and the preliminary engineering studies completed on the design of the therapeutic system left us with a viable means of testing the efficacy of magnetic capture as a means of preventing metastatic growth and improving longevity. This study is currently ongoing. The system implemented appears to be filtering metastatic cells from the peritoneal cavity of the mice but how this will affect longevity cannot be emphatically determined until the experimental group passes the 6 week mortality date.

# APPENDIX A

# PRELIMINARY STUDIES

## HIV-1 Capture Study

The Zeptometrix HIV-1 p24 Antigen ELISA would be used to determine the successful capture of the HIV-1 virus using magnetic nanoparticles. Prior to performing the capture study two experiments were run to determine whether the magnetic nanoparticles would interfere with the performance of the ELISA. A standard procedure with the HIV-1 p24 Antigen ELISA involves running an included known standard at various concentrations and generating a calibration curve to interpolate experimental sample results. The standards were run as they would be normally but a second row of standards containing magnetic nanoparticles were run and the results of both were compared. The manual for the ELISA states that the optical density measurement for the standard having a p24 concentration of 62.5 pg/mL should be above 0.5 and the optical density measurement for the standard having a p24 concentration of 0.0 pg/mL should be less than 0.2 for the test to be valid. Two trials were run and in the first trial $1.34 \times 10^4$ magnetic nanoparticles coated with glucuronic acid and having no antibody conjugates were added to the standard wells in the experimental row. In the second trial $6.69 \times 10^{13}$ magnetic nanoparticles were added. The optical density measurements obtained are featured in Table A.1:

Table A.1: Results from tests conducted to determine whether the magnetic nanoparticles would interfere with the normal function of the ELISA assay.

| TRIAL 1 | STANDARD CONTROL | STANDARD EXPERIMENTAL |
|---|---|---|
| 62.5 pg/mL | 0.6740 | 0.5690 |
| 0.0 pg/mL | 0.0330 | 0.0290 |

| TRIAL 2 | STANDARD CONTROL | STANDARD EXPERIMENTAL |
|---|---|---|
| 62.5 pg/mL | 0.8070 | 0.7810 |
| 0.0 pg/mL | 0.0070 | 0.0080 |

In both trials the optical density measurements were within the acceptable range. It should be noted however that the presence of the magnetic nanoparticles may have accounted for the slightly lower measurements obtained.

**Capture Study Design**

The capture study is visually represented in Figure A.1. In this study the HIV-1 virus was obtained from a stock sample and the concentration was brought within the detectable range of the HIV-1 p24 Antigen ELISA. After diluting the viral sample it was aliquoted into equal volumes in three separate vials. Vial 1 was set aside for testing using the ELISA assay and would serve as a control. Vial 2 was used to perform a viral extraction using magnetic nanoparticles having no antibody conjugates. This vial would serve as another control. Vial 3 was used to perform a viral extraction using magnetic nanoparticles conjugated with anti-HIV-1 gp120. This was the experimental group. Two successful experiments were run using different conditions. The conditions and data have been summarized in Table A.2 and Figure A.2 for the first experiment.

In the second experiment some of the conditions were changed and four vials were tested. Vials 1 and 2 were still control vials and Vial 3 and Vial 4 were experimental vials receiving different concentrations of magnetic nanoparticles with the

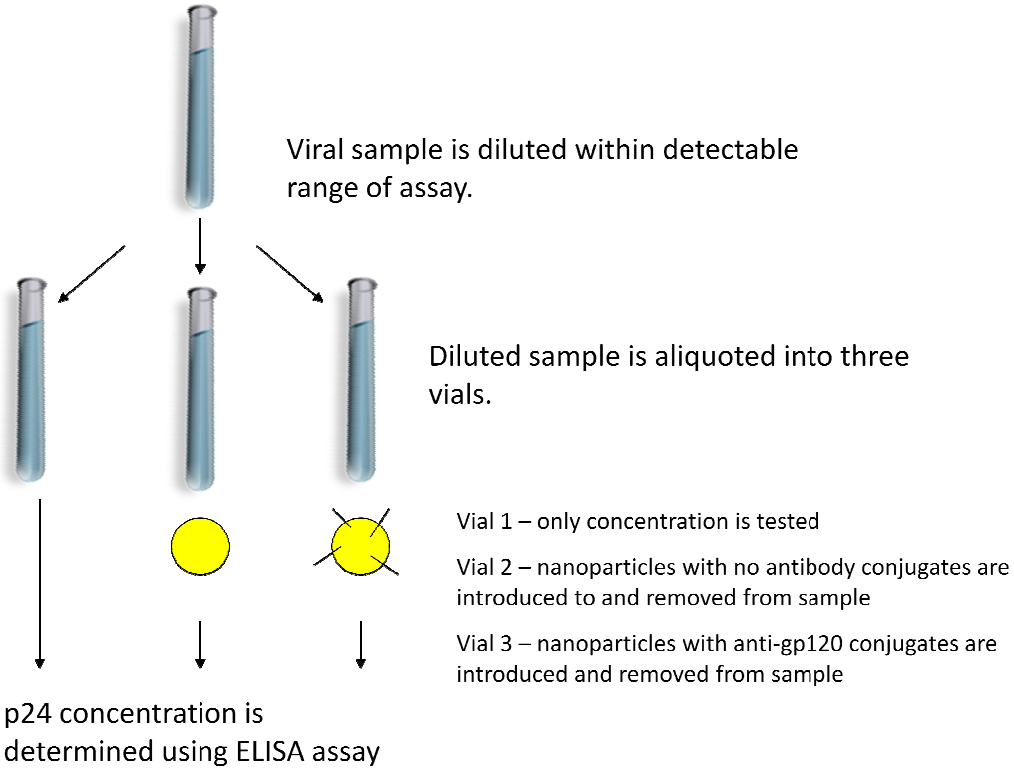


Figure A.1: Overview of HIV-1 Capture Study.

Table A.2: Summary of conditions and results for HIV-1 Capture Study Experiment I.

| **CONDITION** | **VALUE** |
|---|---|
| Temperature | Ambient |
| Incubation Time | 10 min |
| Extraction Time | 10 min |
| # of Magnetic Nanoparticles Introduced (NO Antibody Conjugates) Vial 2 | $6.69 \times 10^{13}$ |
| # of Magnetic Nanoparticles Introduced (WITH Antibody Conjugates) Vial 3 | $7.04 \times 10^{11}$ |
| Viral Particles in Sample | 57,591 |
| Average p24 Concentration in Vial 1 (average of 2 trials) | 53.197 +/- 5.130 (mean +/- standard deviation) |
| Average p24 Concentration in Vial 2 (average of 6 trials) | 53.360 +/- 2.495 (mean +/- standard deviation) |
| Average p24 Concentration in Vial 3 (average of 6 trials) | 47.498 +/- 2.733 (mean +/- standard deviation) |

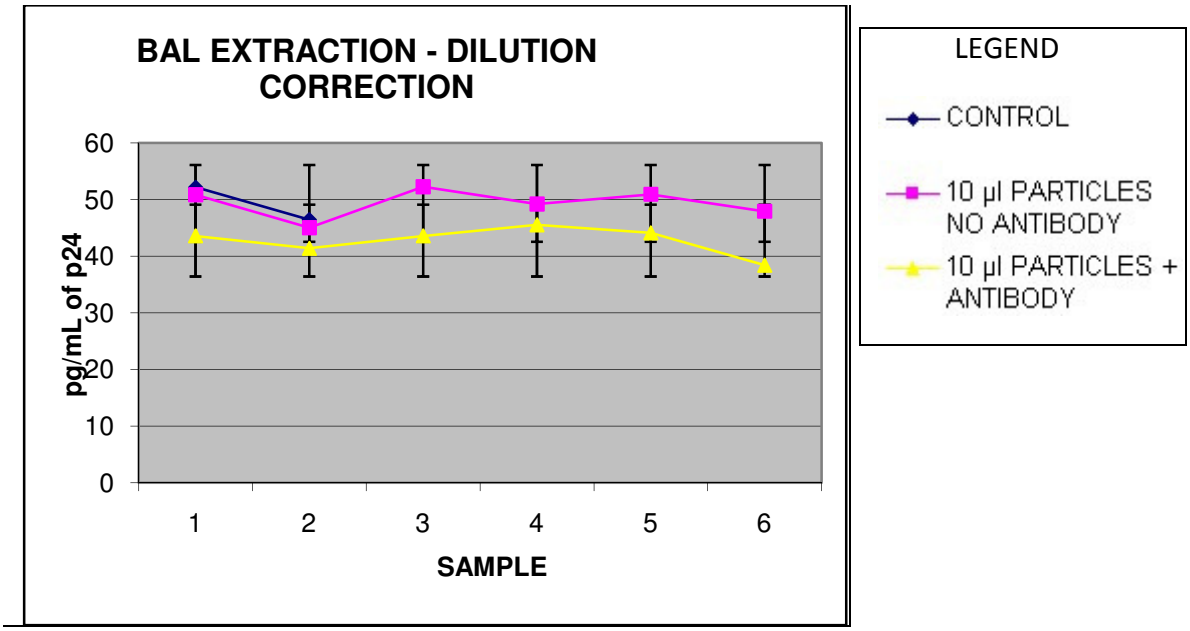


Figure A.2: Data for HIV-1 Capture Study Experiment I.

antibody conjugate. Table A.3 and Figure A.3 summarize the data obtained from this experiment.

Table A.3: Summary of conditions and results for HIV-1 Capture Study Experiment II.

| **CONDITION** | **VALUE** |
|---|---|
| Temperature | 37° C |
| Incubation Time | 30 min |
| Extraction Time | 10 min |
| # of Magnetic Nanoparticles Introduced (NO Antibody Conjugates) Vial 2 | $6.69 \times 10^{14}$ *Note- this is a order of magnitude greater than the previous experiment |
| # of Magnetic Nanoparticles Introduced (WITH Antibody Conjugates) Vial 3 | $3.52 \times 10^{12}$ |
| # of Magnetic Nanoparticles Introduced (WITH Antibody Conjugates) Vial 4 | $7.04 \times 10^{12}$ |
| Viral Particles in Sample | 55,000 |
| Average p24 Concentration in Vial 1 (average of 2 trials) | 58.845 +/- 1.420 (mean +/- standard deviation) |
| Average p24 Concentration in Vial 2 (average of 6 trials) | 48.366 +/- 4.247 (mean +/- standard deviation) |
| Average p24 Concentration in Vial 3 (average of 6 trials) | 46.141 +/- 2.771 (mean +/- standard deviation) |
| Average p24 Concentration in Vial 4 (average of 6 trials) | 22.453 +/- 2.569 (mean +/- standard deviation) |

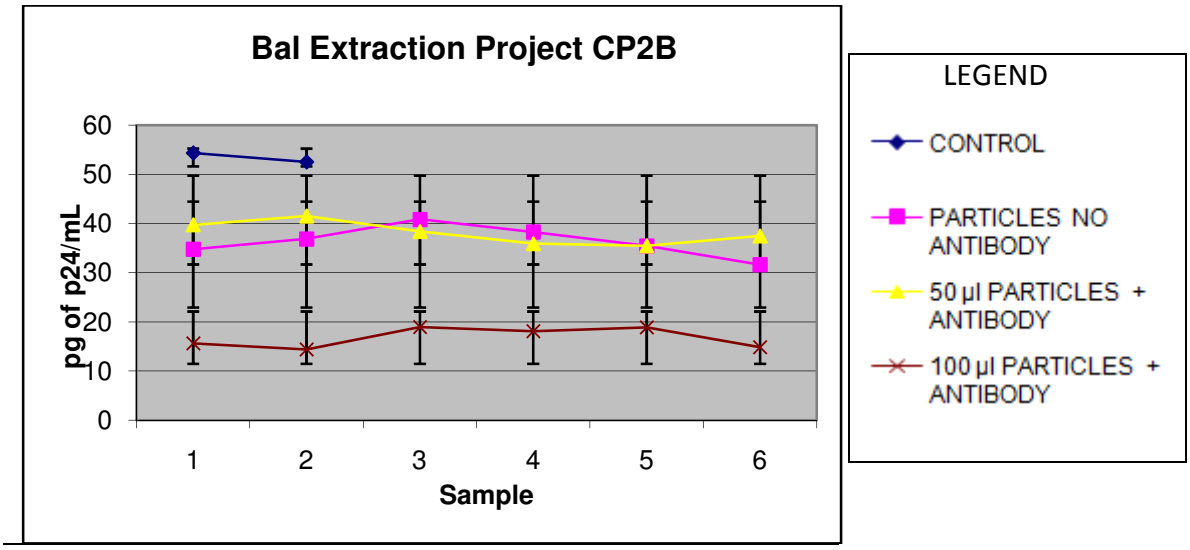


Figure A.3: Data for HIV-1 Capture Study Experiment II.

(NOTE - The average number of antibodies conjugated to each nanoparticle in Experiments 1 & 2 was calculated to be approximately 14.)

**Discussion:**

The results from the first extraction experiment show a difference between the average starting p24 concentration (53.197 +/- 5.130) and the average concentration of the experimental trials (47.498 +/- 2.7333) of 5.699 +/- 5.813. This represents a reduction in p24 concentration of 10.713% +/- 10.976% in the experimental group. In the second extraction experiment a 17.811% +/- 7.622% reduction in p24 concentration is shown for the control trial. This may be attributable to the increased incubation time (i.e. 30 min), the incubation temperature (i.e. 37° C), non-specific binding (i.e. hydrogen bonding), or the interference of particles that remained in the sample with the ELISA assay. A 21.592% +/- 5.317% (50 µL trial) and 61.845% +/- 5.206% (100 µL trial) reduction was seen in the experimental trials. Using the highest p24 concentration from trial 3 of the 100 µL experimental group (25.231 pg/mL), the lowest p24 concentration

from trial 6 of the control group (41.779 pg/mL), and the lower concentration of the initial p24 concentration (57.842 pg/mL) as our starting concentration we calculated a Chi-square value of 9.712 and a p-value of 0.002. This p-value exceeds a 99% confidence interval and indicates significant levels of p24 reduction for the 100 µL experimental group. The fact that Vial 3 showed a greater reduction in p24 concentration than the control group (Vial 2) and that the nanoparticle count used in Vial 2 ($6.69 \times 10^{14}$) significantly outnumbered the count used in Vial 3 ($3.52 \times 10^{12}$) also makes the possibility that p24 concentration was only reduced by interference (i.e. competitive inhibition) improbable. The preliminary data seems to indicate that the antibody conjugates do aid in reducing viral titer but many more studies are necessary to determine whether this approach could be a viable therapy.

**Reaction Impedance Study**

Various conditions can affect the speed of a chemical reaction. These conditions can include the presence of a catalyst, temperature, the physical state of the reactants, or the concentration of the reactants. Manipulation of any of these conditions can effectively throttle the reaction kinetics. In an equilibrium reaction increasing reaction concentration can shift the reaction balance in favor of product formation and increasing product concentrations or decreasing reactant concentrations can impede product formation. In general, it is a difficult endeavor to separate reactants from a reaction ad libitum but using magnetic nanoparticles provides a novel approach to do just that. Conjugating magnetic nanoparticles to one of the reactants allows the reactant to be selectively removed from the reaction and returned if necessary at a distant time point. This brief chapter describes a proof of concept that visually shows what I have proposed. Magnetic nanoparticles were conjugated to a reactant in a

chemiluminescent reaction to show that the production of light could be controlled at will.

**Results and Discussion**

The methods by which one produces chemiluminescence have been well researched and it was not necessary to reinvent them. Our goal was to use an already established means of producing a high quantum yield of light over a sufficient duration and modify that mechanism by introducing MNPs, thereby providing a means of controlling the progression of the reaction. Figure A.4 illustrates one mechanism that

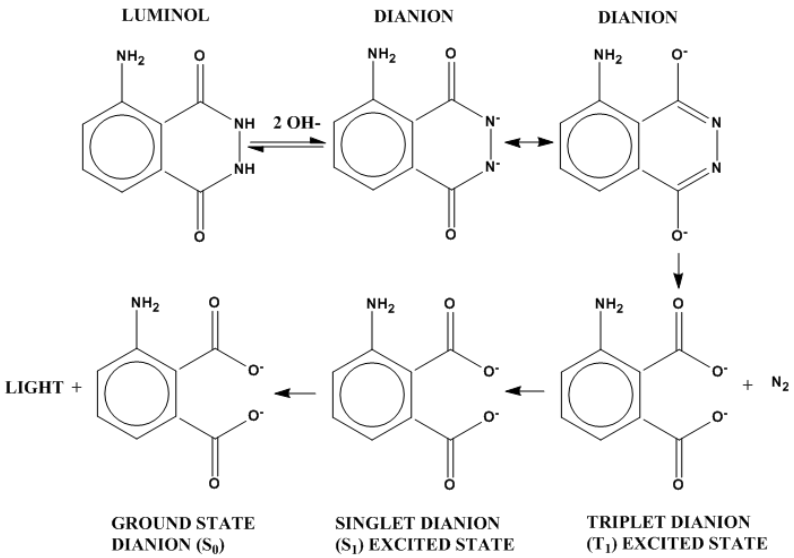


Figure A.4: Chemiluminescent reaction involving luminol.

uses luminol to produce light. The mechanism was studied to determine which reagent could serve as a particle conjugate and act to manage the reaction kinetics.

Two strategies were proposed. The first purported that the MNP could be used to control the reagents involved in the oxidation of the deprotonated hydroxyl groups on the dianon to carboxyl groups. The reaction would need to run in alkaline solution

and this would mean that the hydroxyls on the MNP surface should be deprotonated. If potassium oxide were used as an oxidant it was conceivable that the MNP anions would substitute for the oxide in $KO_2$ releasing oxygen into the solution. We found no precedents for using potassium hydroxide as an oxidant in this particular reaction so we estimated the ratios of reagents needed until we found a suitable mix. 1 mg of luminol was dissolved in 20 mL of 5 M NaOH and 10 mg of potassium hydroxide was added to the solution. The MNPs were mixed in 5 M NaOH separately for about 10 minutes to deprotonate the surface hydroxyls and then the particles were added to the solution containing luminol. The problem with this approach was that potassium oxide was practically insoluble in the alkaline solution and continually precipitated out. However, it was noted that upon adding the MNPs, bubbling was immediately observed from the precipitate and light was produced. The solubility issue with the potassium oxide caused us to quickly abandon this approach and seek another.

Further inspection of the reaction scheme in Figure A.2 lead me to believe that it might be possible to use luminol's primary amine as a conjugation point. It did not appear to be playing any role in the production of light but this was verified through a literature search. Conjugating the MNP to luminol would mean that luminol could be extracted from the reaction at any point prior to completion. To conjugate luminol to the MNP surface, carboxyl groups were first added using a 100-fold molar excess of terepthalic acid. The 1:100 molar ratio was used to limit polymerization and insure that free carboxyls would be present to form amide bonds with the primary amine of luminol.

Initially it was unclear whether the luminosity of luminol's emissions would be dependent on the polarity of the solvent. This was tested by running the experiments in

methanol, ethanol, and distilled water. Unaided visible emissions were observed in each case. However, one unusual difference was discovered.

UV/Vis spectroscopy was used to follow the conjugation process and spectra of unconjugated luminol were observed in three different solvents; methanol, ethanol, and distilled water (Figure A.5-A.7). The conjugation procedure was carried out by binding terepthalic acid to the surface of the particle that could in turn bind luminol. Spectra of these conjugates were observed as well. Strangely, the samples containing pure luminol in aqueous solution showed a shift into the UV range. This shift was also seen post conjugation to the magnetic particles. A literature search provided an explanation for the phenomena. Ghoheim et al. [82] had observed a red shift in the fluorescent spectrum of luminol when it went from a polar to non-polar solvent. It was resolved that this was

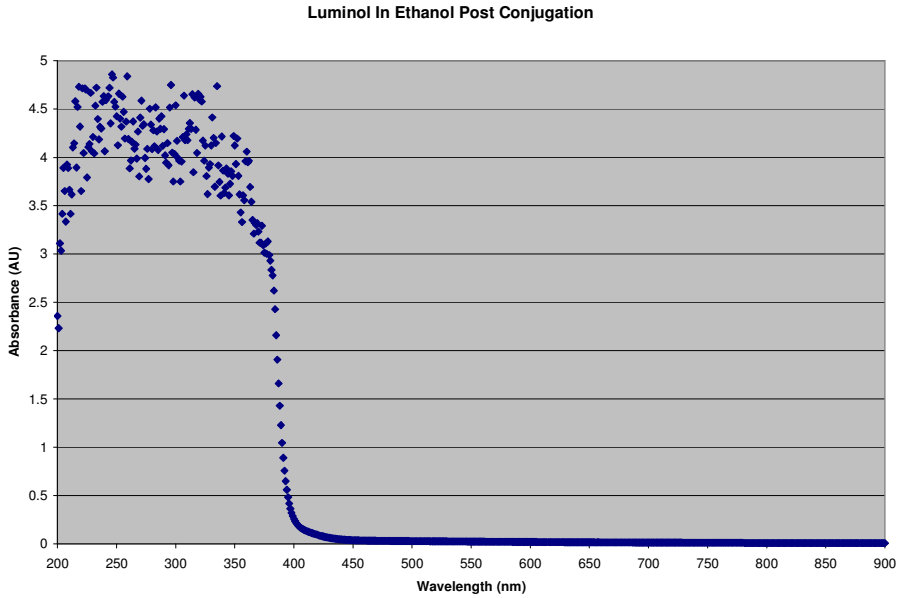


Figure A.5: UV/Vis spectrum for luminol dissolved in ethanol.

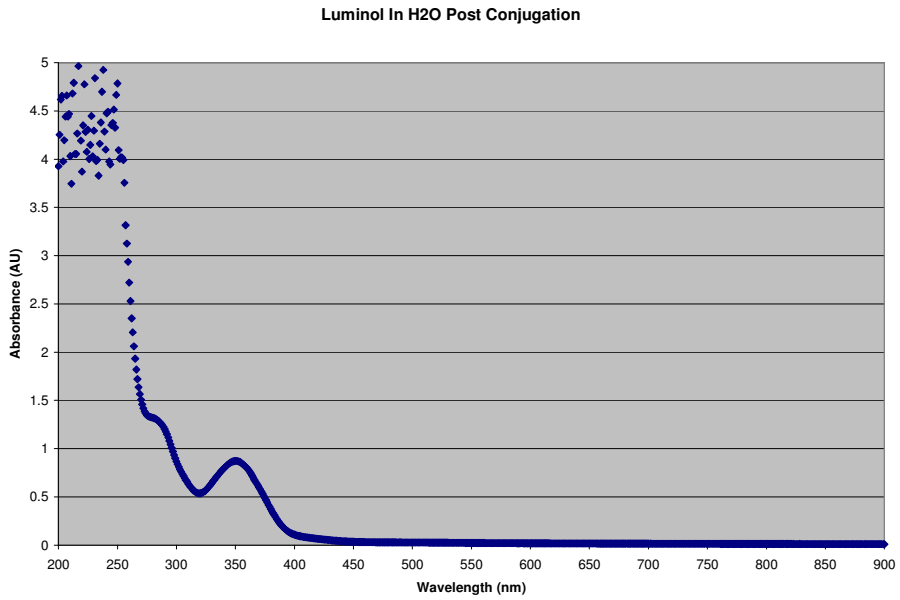


Figure A.6: UV/Vis spectrum of luminol dissolved in aqueous solution.

a result of the stabilization of the excited states in the polar solvent. Luminol emissions were a direct result of the hydrogen bonds formed with the solvent.[83] This effect enabled me to use fluorescent microscopy as an additional means of verifying luminol's conjugation to the particle surface.

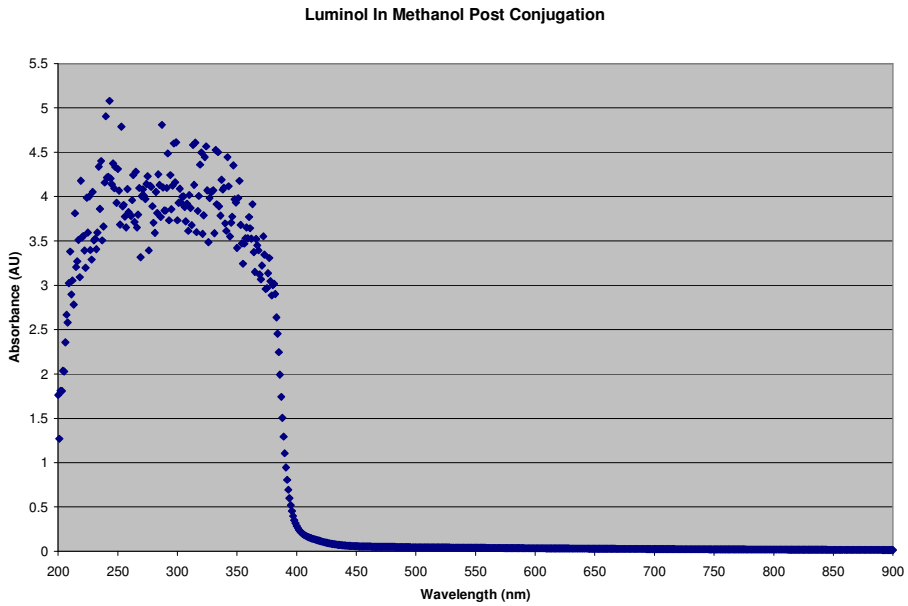


Figure A.7: UV/Vis spectrum of luminol dissolved in methanol.

Once it was evident that the luminol had been successfully conjugated to the MNP, it was necessary to verify its ability to impede reaction progression. A procedure was found for using luminol to produce visible light that involved diluting household bleach in distilled water at a ratio of 10 mL/1 L respectively. 10 mL of the diluted bleach was then added to 5 mL of 0.1 M NaOH in a clear 25 dram glass vial. A 2000 gauss magnet was placed at the side of the vial and the lights were turned out in the laboratory. 100 µL of the luminol/MNP conjugate was added to the solution in the glass vial and a blue light was immediately apparent that quickly left the solution and aggregated on the side of the vial where the magnet had been placed. If the particle/luminol aggregate was pulled from the solution by sliding the magnet above the solution line prior to the reaction running its course the light was no longer visible. Pulling the particles back into solution continued the light production process around the aggregate. The experiment verified that we had developed a simple means of

controlling reaction kinetics. However, the main caveat would be that the success of the approach would depend on the conjugability of the particle to a reagent in a manner that would not adversely affect its natural reactivity.

## REFERENCES


1. Berry, C. C.; Curtis, A. S. G., Functionalisation of magnetic nanoparticles for applications in biomedicine. *Journal of Physics D: Applied Physics* **2003,** *36*, 198-206.

2. Ito, A.; Shinkai, M.; Honda, H.; Kobayashi, T. J., *Biosci. Bioeng.* **2005,** *100*.

3. Dutza, S.; Andraa, W.; Hergta, R.; Mullera, R.; Oestreichc, C.; Schmidta, C.; Topferd, J.; Zeisbergera, M.; Bellemann, M., Influence of dextran coating on the magnetic behavior of iron oxide nanoparticles. *Journal of Magnetism and Magnetic Materials* **2007,** *311* (1), 51-54.

4. Gupta, A.; Gupta, M., Synthesis and surface engineering of iron oxide nanoparticles for biomedical applications. *Biomaterials* **2005,** *26* (18), 3995-4021.

5. Pankhurst, Q.; Connolly, J.; Jones, S. K.; Dobson, J., Applications of magnetic nanoparticles in biomedicine. *Journal of Physics D: Applied Physics* **2003,** *36*, 167-181.

6. Georganopoulou, D. G.; Chang, L.; Nam, J. M.; Thaxton, C. S.; Mufson, E. J.; Klein, W. L.; Mirkin, C. A., *Proc. Natl. Acad. Sci. USA* **2005,** *102*.

7. Herr, J. K.; Smith, J. E.; Medley, C. D.; Shangguan, D.; Tan, W., *Anal. Chem.* **2006,** *78*.

8. Nam, J. M.; Thaxton, C. S.; Mirkin, C. A., *Science* **2003,** *301*.

9. Smith, J. E.; Medley, C. D.; Tang, Z.; Shangguan, D.; Lofton, C.; Tan, W., *Anal. Chem.* **2007,** *79*.

10. Potineni, A.; Lynn, D.; Langer, R.; Amiji, M., Poly(ethylene oxide)-modified ply(B-amino ester) nanoparticles as a pH-sensitive biodegradable system for paclitaxel delivery. *Journal of Controlled Release* **2003,** *86* (2-3), 223-234.

11. Zhao, A.; Yao, P.; Kang, C.; Yuan, X.; Chang, J.; Pu, P., Synthesis and characterization of tat-mediated O-CMC magnetic nanoparticles having anticancer function. *Journal of Magnetism and Magnetic Materials* **2004,** *295* (1), 37-43.

12. Kim, J.; Yoon, T. J.; Yu, K.; Kim, B.; Park, S.; Kim, H.; Lee, K.; Park, S.; Lee, J. K.; Cho, M., Toxicity and Tissue Distribution of Magnetic Nanoparticles in Mice. *Toxicological Sciences* **2006,** *89* (1), 338-347.

13. Liu, C.; Zou, B.; Rondinone, A. J.; Zhang, Z. J., Chemical Control of Superparamagnetic Properties of Magnesium and Cobalt Spinel Ferrite Nanoparticles through Atomic Level Magnetic Couplings. *Journal of the American Chemical Society* **2000,** *122* (26).

14. Li, S.; John, V. T.; O'Connor, C.; Harris, V.; Carpenter, E., Cobalt-ferrite nanoparticles: Structure, cation distributions, and magnetic properties. *Journal of Applied Physics* **2000,** *87* (9), 6223-6225.

15. Bautista, C. M.; Bomati-Miguel, O.; Morales, M. d. P.; Serna, C. J.; Veintemillas-Verdaguer, S., Surface characterization of dextran-coated iron oxide nanoparticles prepared by laser pyrolysis and coprecipitation. *Journal of Magnetism and Magnetic Materials* **2005,** *293*, 20-27.

16. Jeong, U.; Teng, X.; Wang, Y.; Yang, H.; Xia, Y., *Adv. Mater.* **2007,** *19*.

17. Gallop, J. C., *SQUIDs, the Josephson Effects and Superconducting Electronics*. Adam Hilger: 1990.

18. Lacava, L. M.; Garcia, V. A. P.; Kuckelhaus, S.; Azevedo, R. B.; Sadeghiani, N.; Buske, N.; Morais, P. C.; Lacava, Z. G. M., Long-term retention of dextran-coated magnetite nanoparticles in the liver and spleen. *Journal of Magnetism and Magnetic Materials* **2004,** *272-276*, 2434-2435.

19. Lavhasetwar, V.; Song, C.; Humphrey, W.; Shebuski, R.; Levy, R. J., Arterial uptake of biodegradable nanoparticles: effect of surface modifications. *J. Pharm. Sci.* **1998,** *87*, 1229-1234.

20. Geiser, M.; Schurch, S.; Gehr, P., Influence of surface chemistry and topography of particles on their immersion into the lung's surface-linin layer. *J. Appl. Physiol.* **2003,** *94*, 1793-1801.

21. Roodman, G. D., Mechanisms of bone metastasis. *New England Journal of Medicine* **2004,** *350* (16), 1655-1664.

22. Barnholtz-Sloan, J. S.; Sloan, A. E.; Davis, F. G.; Vigneau, F. D.; Lai, P.; Sawaya, R. E., Incidence proportions of brain metastases in patients diagnosed (1973 to 2001) in the Metropolitan Detroit Cancer Surveillance System. *Journal of Clinical Oncology: Official Journal of the American Society of Clinical Oncology* **2004,** *22* (14), 2865-72.

23. Aragon-Ching, J. B.; Zujewski, J. A., CNS Metastasis: An Old Problem in a New Guise. *Clinical Cancer Research* **2007,** *13* (6), 1644-1647.

24. Lin, N. U.; Winer, E. P., Brain Metastases: The HER2 Paradigm. *Clinical Cancer Research* **2007,** *13* (6), 1648-1655.

25. O'Sullivan, B.; Levin, W., Late radiation-related fibrosis: Pathogenesis, manifestations, and current management. *Seminars in Radiation Oncology* **2003,** *13* (3), 274-289.

26. Manikandan, J.; Pushparaj, P. N.; Melendez, A. J., *Frontiers in Bioscience* **2007,** *12*, 1344-1352.

27. Swan, C. H.; Torbett, B. E., *Journal of Medical Primatology* **2006,** *35* (4-5), 236-247.

28. Rondon, I. J.; Marasco, W. A., *Annual Review of Microbiology* **1997,** *51*, 257-283.

29. Jennings, C.; Fiscus, S. A.; Crowe, S. M.; Danilovic, A. D.; Morack, R. J.; Scianna, S.; Cachafeiro, A.; Brambilla, D. J.; Schupbach, J.; Stevens, W.; Respess, R.; Varnier, O. E.; Corrigan, G. E.; Gronowitz, J. S.; Ussery, M. A.; Bremer, J. W., Comparison of Two Human Immunodeficiency Virus (HIV) RNA Surrogate Assays to the Standard HIV RNA Assay. *Journal of Clinical Microbiology* **2005,** *43* (12), 5950-5956.

30. Powis, G.; Gaskada, J. R.; Berggren, M.; Kirkpatrick, D. L.; Engman, L.; Cotegreave, I. A.; Angulo, M.; Bzker, A., *Oncology Research* **1997,** *6*.

31. Gallegos, A.; Berggren, M.; Gaskada, J. R.; Powis, G., *Cancer Research* **1997,** *57*.

32. Hondal, R., Incorporation of Selenocysteine into Proteins Using Peptide Ligation. *Protein & Peptide Letters* **2005,** *12*, 757-764.

33. Kaur, D.; Sharma, P.; Bharatam, P. V., A comparative study on the nature and strength of O-O, S-S, and Se-Se bond. *Journal of Molecular Structures* **2007,** *810*, 31-37.

34. White, E.; Zafiriou, O.; Kagi, H. H.; Hill, J. H. M., Chemiluminescence of Luminol: The Chemical Reaction. *Journal of the American Chemical Society* **1964,** *86* (5), 940-941.

35. Zhang, L.; Yang, N.; Garcia, J. R. C.; Mohamed, A.; Benencia, F.; Rubin, S. C.; Allman, D.; Coukos, G., Generation of a Syngeneic Mouse Model to Study the Effects of Vascular Endothelial Growth Factor in Ovarian Carcinoma. *American Journal of Pathology* **2002,** *161* (6), 2295-2309.

36. Burnette, W. N., *Analytical Biochemistry* **1981,** *112* (2), 195-203.

37. Qing, W. Tumor models employing green fluorescent protein. EP20070104650, 03/22/2007, 2007.

38. Hermanson, G., *Bioconjugate Techniques, 2nd Ed.* Elsevier: 2008.

39. Klayman, D. L.; Griffin, S., Reaction of Selenium with Sodium Borohydride in Protic Solvents. A Facile Method for the Introduction of Selenium into Organic Molecules. *Journal of the American Chemical Society* **1973,** *95*, 197-199.

40. Mugesh, G., Selenenyl iodide: a new substrate for mammalian thioredoxin reductase. *Org. Biomol. Chem.* **2003,** *1*, 2848-2852.

41. Jacob, C.; Giles, G. I.; Giles, N. M.; Sies, H., Sulfur and Selenium: The role of Oxidation State in Protein Structure and Function. *Angewandte Chemie International Edition* **2003,** *42* (39), 4742-4758.

42. Scarberry, K. E.; Dickerson, E. B.; McDonald, J. F.; Zhang, Z. J., Magnetic Nanoparticle-Peptide Conjugates for in Vitro and in Vivo Targeting and Extraction of Cancer Cells. *Journal of the American Chemical Society* **2008,** *130* (31), 10258-10262.

43. Song, Q.; Zhang, Z. J., *Journal of Physical Chemistry B* **2006,** *110*.

44. NIH press release, January 4, 2006. http://www.cancer.gov/newscenter/pressreleases/IPchemotherapyrelease.

45. Chi, D. S.; Hoskins, W. J., *Ovarian Cancer Methods and Protocols*. Humana Press: 2000; p 75.

46. Hanahan, D.; Weinberg, R. A., *Cell* **2000,** *100*.

47. Fidler, I. J., *Nat. Rev. Cancer* **2003,** *3*.

48. Sainz de la Cuesta, R.; Goff, B. A.; Fuller, A. F., Jr.; Nikrui, N.; Eichhorn, J. H.; Rice, L. W., *Obstet. Gynecol.* **1994,** *84*.

49. Koolpe, M.; Dail, M.; Pasquale, E. B., An Ephrin Mimetic Peptide That Selectively Targets the EphA2 Receptor. *Journal of Biological Chemistry* **2002,** *277* (49), 46974-46979.

50. Han, L.; Dong, Z.; Qiao, Y.; Kristensen, G. B.; Holm, R.; Nesland, J. M.; Suo, Z., The clinical significance of EphA2 and Ephrin A-1 in epithelial ovarian carcinomas. *Gynecologic Oncology* **2005,** *99*, 278-286.

51. Thaker, P. H.; Deavers, M.; Celestino, J.; Thornton, A.; Fletcher, M. S.; Landen, C. N.; Kinch, M. S.; Kiener, P. A.; Sood, A. K., *Clinical Cancer Research* **2004,** *10*.

52. Clark, K. D.; Volkman, B. F.; Thoetkiattikul, H.; King, D.; Hayakawa, Y.; Strand, M. R., *J. Biol. Chem.* **2001,** *276*.

53. Goldstein, D. S.; Lu, M. L.; Hattori, T.; Ratliff, T. L.; Loughlin, K. R.; Kavoussi, L. R., *J. Endoruol.* **1993,** *7*.

54. Flam, F., Einhorn, N., Sjovall, K., Symptomatology of ovarian cancer. *European Journal of Obstetrics Gynecology and Reproductive Biology* **1988,** *27*, 53-57.

55. Feldman, G. B.; Knapp, R. C.; Order, S. E.; Hellman, S., The role of lymphatic obstruction in the formation of ascites in a murine ovarian carcinoma. *Cancer Research* **1972,** *32*, 1663-1666.

56. Hirabayashi, K.; Graham, J., The genesis of ascites in ovarian cancer. *American Journal of Obstetrics Gynecology* **1970,** *106*, 492-497.

57. Gabrilovich, D. I.; Nadaf, S.; Corak, J.; Berzofsky, J. A.; Carbone, D. P., Dendritic cells in antitumor immune responses. II. Dendritic cells grown from bone marrow precursors, but not mature DC from tumor-bearing mice are effective antigen carriers in the therapy established tumors. *Cellular Immunology* **1996,** *170* (1), 111-119.

58. Ishida, T.; Oyama, T.; Carbone, D.; Gabrilovich, D. I., Defective function of Langerhans cells in tumor-bearing animals is the result of defective maturation from hematopoietic progenitors. *Journal of Immunology* **1998,** *161*, 4842-4851.

59. Nestle, F. O.; Burg, G.; Fah, J.; Wrone-Smith, T.; Nickoloff, B. J., Human sunlight-induced basal-cell-carcinoma-associated dendritic cells are deficient in T cell co-stimulatory molecules and are impaired as antigen-presenting cells. *American Journal of Pathology* **1997,** *150*, 641-651.

60. Chaux, P.; Favre, N.; Martin, M.; Martin, F., Tumor-infiltrating dendritic cells are defective in their antigen-presenting function and inducible B7 expression in rats. *International Journal of Cancer* **1997,** *72* (4), 619-624.

61. Curtin, J. P.; Malik, R.; Venkatraman, E. S.; Barakat, R. R.; Hoskins, W. J., Stage IV ovarian cancer: impact of surgical debulking. *Gynecologic Oncology* **1997,** *64*, 9-12.

62. Griffiths, C. T.; Parker, L. M.; Fuller, A. J., Role of cytoreductive surgical treatment in the management of advanced ovarian cancer. *Cancer Treatment Reports* **1979,** *63* (2), 235-240.

63. Kosary, C. L., FIGO stage, histology, histological grade, age and race as prognostic factors in determining survival for cancers of the female gynecological system: an analysis of 1973-1987 SEER cases of cancers of the endometrium, cervix, ovary, vulva and vagina. *Seminars in Surgical Oncology* **1994,** *10*, 31-46.

64. Diaz-Arias, A. A.; Loy, T. S.; Bickel, J. T.; Chapman, R. K., Utility of BER-EP4 in the diagnosis of adenocarcinoma in effusions: an immunocytochemical study of 232 cases. *Diagnostic Cytopathology* **1993,** *9* (5), 516-21.

65. Forster, M. D.; Ormerod, M. G.; Agarwal, R.; Kaye, S. B.; Jackman, A. L., Flow Cytometric Method for Determining Folate Receptor Expression on Ovarian Carcinoma Cells. *Cytometry Part A.* **2007,** *71A* (11), 945-950.

66. Bast, R. C.; Jr., M. F.; Lazarus, H.; Nadler, L. M.; Colvin, R. B.; Knapp, R. C., Reactivity of a monoclonal antibody with human ovarian carcinoma. *Journal of Clinical Investigation* **1981,** *68*, 1331-7.

67. Canney, P. A.; Moore, M.; Wilkinson, P. M.; James, R. D., Ovarian cancer antigen CA125: a prospective clinical assessment of its role as a tumour marker. *British Journal of Cancer* **1984,** *50*, 765-9.

68. Kabawat, S. E.; Bast, R. C.; Welch, W. R.; Knapp, R. C.; Colvin, R. B., Immunopathologic characterization of a monoclonal antibody that recognizes common surface antigens of human ovarian tumors of serous, endometrioid, and clear cell types. *American Journal of Clinical Pathology* **1983,** *79*, 98-104.

69. Meyer, T.; Rustin, G. J. S., Role of tumour markers in monitoring epithelial ovarian cancer. *British Journal of Cancer* **2000,** *82* (9), 1535-1538.

70. Thaker, P. H.; Deavers, M.; Celestino, J.; Thornton, A.; Fletcher, M. S.; Landen, C. N.; Kinch, M. S.; Kiener, P. A.; Sood, A. K., EphA2 Expression Is Associated with Aggressive Features in Ovarian Carcinoma. *Clinical Cancer Research* **2004,** *10*, 5145-5150.

71. Harries, M.; Gore, M., Part I: chemotherapy for epithelial ovarian cancer-treatment at first diagnosis. *The Lancet Oncology* **2002,** *3* (9), 537-45.

72. Cohen, L. E., Cancer treatment and the ovary: the effects of chemotherapy and radiation. *Annals of the New York Academy of Sciences* **2008,** *1135* (Menstrual Cycle and Adolescent Health), 123-125.

73. Ziselman, E. M.; Harkavy, S. E.; Hogan, M.; West, W.; Atkinson, B., Peritoneal washing cytology. Uses and diagnostic criteria in gynecologic neoplasms. *Acta cytologica* **1984,** *28* (2), 105-10.

74. Croonen, A. M.; Valk, P. v. d.; Herman, C. J.; Lindeman, J., Cytology, immunopathology and flow cytometry in the diagnosis of pleural and peritoneal

effusions. *Laboratory investigation; a journal of technical methods and pathology* **1988,** *58* (6), 725-32.

75. Shield, P. W.; Callan, J. J.; Devine, P. L., Markers for metastatic adenocarcinoma in serous effusion specimens. *Diagnostic Cytopathology* **1994,** *11*, 237-245.

76. Tuxen, M. K.; Soletormos, G.; Dombernowsky, P., Tumour markers in the management of patients with ovarian cancer. *Cancer Treatment Reviews* **1995,** *21*, 215-245.

77. Hafner, C.; Schmitz, G.; Meyer, S.; Bataille, F.; Hau, P.; Langmann, T.; Dietmaier, W.; Landthaler, M.; Vogt, T., Differential Gene Expression of Eph Receptors and Ephrins in Benign Human Tissues and Cancers. *Clinical Chemistry* **2004,** *50* (3), 490-499.

78. Pasquale, E. B., The Eph Family of receptors. *Current Opinion in Cell Biology* **1997,** *9* (5), 608-615.

79. Cheng, N.; Brantley, D. M.; Chen, J., The ephrins and Eph receptors in angiogenesis. *Cytokine Growth Factor* **2002,** *13*, 75-85.

80. Barth, M. W.; Morahan, P. S., Role of macrophages in the host response to Lewis lung peritoneal carcinomatosis. *Cancer Immunology Immunotherapy* **1994,** *38* (4), 233-42.

81. Zhou, L. J.; Tedder, T. F., Human blood dendritic cells selectively express CD83, a member of the immunoglobulin superfamily. *Journal of Immunology* **1995,** *154* (8), 3821-3835.

82. Ghoneim, N., *J. Photochem. Photobiol. A: Chem.* **1991,** *60*.

83. Mitra, S.; Das, R.; Mukherjee, S., Complex formation and photophysical properties of luminol: solvent effects. *Journal of Photochemistry and Photobiology* **1995,** *87*, 225-230.